UNIVERSITY OF TRENTO

Development of a Damage Indicator Based on Detection of High-Frequency Transients Monitored in Bridge Piers During Earthquake Ground Shaking

by

Aleksandar Zhelyazkov

A thesis submitted in partial fulfillment for the
degree of Doctor of Philosophy

in the
Department of Civil, Environmental and Mechanical Engineering
University of Trento

May 2020

Declaration of Authorship

I, ALEKSANDAR ZHELYAZKOV, declare that this thesis titled, 'DEVELOPMENT OF A DAMAGE INDICATOR BASED ON DETECTION OF HIGH-FREQUENCY TRANSIENTS MONITORED IN BRIDGE PIERS DURING EARTHQUAKE GROUND SHAKING' and the work presented in it are my own. I confirm that:

- This work was done wholly or mainly while in candidature for a research degree at the University of Trento.
- Where any part of this thesis has previously been submitted for a degree or any other qualification at the University of Trento or any other institution, this has been clearly stated.
- Where I have consulted the published work of others, this is always clearly attributed.
- Where I have quoted from the work of others, the source is always given. With the exception of such quotations, this thesis is entirely my own work.
- I have acknowledged all main sources of help.
- Where the thesis is based on work done by myself jointly with others, I have made clear exactly what was done by others and what I have contributed myself.

Signed: _____

Date: _____

"That seems to be an abstraction of your fiction."

Georgi Varbanov

UNIVERSITY OF TRENTO

Abstract

Department of Civil, Environmental and Mechanical Engineering
University of Trento

Doctor of Philosophy

by Aleksandar Zhelyazkov

Real-time structural health monitoring is a well established tool for post-earthquake damage estimation. A key component in the monitoring campaign is the approach used for processing the data from the structural health monitoring system. There is a large body of literature on signal processing approaches aimed at identifying ground-motion induced damage in civil engineering structures. This dissertation expands on a specific subgroup of processing approaches dealing with the identification of damage induced high-frequency transients in the monitoring data. The underlying intuition guiding the current research can be formulated in the following hypothesis - the time difference between the occurrence of a high-frequency transient and the closest deformation extremum forward in time is proportional to the degree of damage. A mathematical deduction is provided in support of the above hypothesis followed by a set of shaking table tests. For the purposes of this research two shaking table tests of reinforced concrete bridge piers were performed. Data from a shaking table test performed by another research group was also analyzed. The cases in which the proposed procedure could find a practical application are examined along with the present limitations.

Acknowledgements

My acknowledgements go to Professor Daniele Zonta for his key guidance during my research. I would also like to express my gratitude and acknowledgements to Professor Helmut Wenzel and Dipl.Ing. Peter Furtner for their constant guidance and support over the last few years. I express my gratitude also to Professor Stathis Bousias and Dr. Elias Strepelias for efforts, support and hospitality during the experimental works at the University of Patras. Finally, I would like to express my gratitude for the guidance and patience of Professor Oreste Bursi.

Contents

List of Figures

List of Tables

Abbreviations

SHM	**S**tructural **H**ealth **M**monitoring
TRDI	**T**ime **R**atio **D**amage **I**ndicator
AE	**A**coustic **E**mission
EDP	**E**ngineering **D**emand **P**arameter
GPS	**G**lobal **P**ositioning **S**ystem
LVDT	**L**inear **V**ariable **D**eformation **T**ransformer
HFT	**H**igh **F**requency **T**ransient
STFT	**S**hort **T**ime **F**ourier **T**ransformation
VoI	**V**alue **o**f **I**information

Symbols

t	time	seconds
ϵ	strain	-
r	correlation coefficient	-

I would like to thank my family for the constant care and support.

Chapter 1

Introduction

A method for the estimation of the ductility demand on reinforced concrete piers during a ground seismic shaking is proposed. The required input is the measurement data from a structural health monitoring system within the time window of the seismic event. The procedure relies on detection of high-frequency transients related to damage and their distance forward in time to the closest deformation extrema. A formulation is proposed which relates these measurements to the ductility demand on the pier. A step-by-step description of the procedure is provided along with a case-study implementation on an experimental reinforced concrete column. The ductility demand is estimated and compared with the one obtained from the experimental force-deformation curve.

1.1 Motivation

Methods for estimation of earthquake induced damage in civil engineering structures have long been a subject of interest for the scientific community. One way for tackling the problem of detecting earthquake induced damage is to implement a Structural Health Monitoring (SHM) system [6], [7].

Reliable an efficient SHM is a prerequisite for loss reduction in case of an earthquake event [8], [9]. A loss reduction would occur in case the SHM indicates insignificant or no damage to the structure, which implies the possibility for immediate occupancy of the structure. The reduced loss follows from the decrease in down-time of the structure, as compared to down-times required in alternative procedures for damage estimation (destructive and non-destructive physical tests [10]). Another scenario for loss reduction enabled by SHM is in the case of significant damage to the structure.

Appropriate decisions in this case are no further occupation of the structure in its current state followed by a demolition or retrofitting campaign [11]. The SHM should aid the stakeholders in this decision-making process and therefore reduce the probability of loss of life and capital.

The above formulates the goals for the research currently presented - estimate the damage state of a structure from output data provided by SHM. A solution based on a specific processing approach, which in essence is the damage estimation method, is discussed. The result of the processing is a damage indicator, named the Time-Ratio Damage Indicator ($TRDI$), which is directly related to the deformation demand on the structure. The discussed solution is developed for reinforced concrete structures, but applications for other fragile materials are conceivable.

$TRDI$ relies on two sets of input values - time instances of damage "initiation" and time instances of deformation peaks. The mathematical formulation and processing steps required for the calculation of the $TRDI$ are presented later in the thesis. At his stage, it is nevertheless useful to throw light on the main concept behind the damage indicator - the time difference between damage "initiation" and deformation peak is indicative of the level of damage. The formulation of the discussed damage index relates it directly to the relative displacement of the structure and consequently to the ductility demand. The technique is suitable only for structures with a predominant first mode response.

The main motivation behind the development of current the procedure are the reported considerable inaccuracies in the most widely implemented method for calculation of drift and ductility demand - double integration of the acceleration record at top and bottom of the structure [12],[13] . Due to the noise in the record the integrated acceleration would generally have a visible drift from the expected average and will break the physical constraint of zero velocity at the end of the dynamic response. This is avoided by implementing the so called base "correction" (adjustment) which guarantees zero velocity at the end of the dynamic response [2]. Methods for base correction include high-pass filtering and polynomial fitting. An observed issue is the fact that after the "correction" the non-linear part of the response is lost, which is exactly the part of the response related to structural damage. The current research aims to solve this problem by also avoiding the need for further installation of more expensive instrumentation, such as LVDT's, GPS, etc.

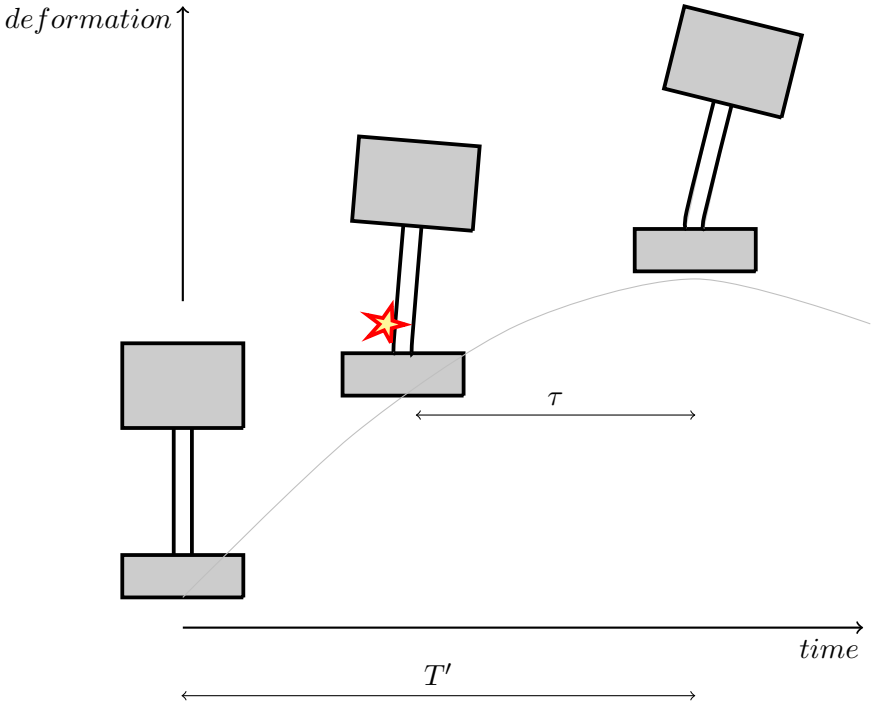

FIG. 1.1 TRDI concept

1.2 Discussion on methods for detection of earthquake induced damage

Damage detection and estimation methods, based on output from SHM, could be divided in three main groups - methods relying on detection of permanent changes in the character of structural response (vibrational methods), methods relying on detection of specific transient response and methods relying on direct estimation of Engineering Demand Parameters (EDP's).

The arbitrary division above is meaningful when the discussion is limited to an explicit estimation of physical parameters - parametric methods. Examples of non-parametric methods are the implementation of neural networks ([14], [15], [16], [17]), fuzzy neural networks ([18], [19], [20], [21]), wavelets [22], Hilbert-Huang transform [23]. Such methods are outside the scope of this thesis.

1.2.1 Vibrational methods

The main concept behind the first group is that the presence of damage is reflected in changes in the modal properties of the structure ([24], [25], [26], [27], [28], [29]). Although this is the most widely used approach for damage detection there are several

issues arising - for example reduction of stiffness and/or increase in damping at the early stages of damage is normally insignificant and therefore the identified modal properties are seemingly unchanged. Further, the identified modal properties are affected by external loading and temperature, although there are methods, based on statistical processing of the data, which could compensate the influence of external factors [30]. The most prominent external factor affecting the identified parameters is temperature. The mechanism governing temperature effects on parameters, such as modal frequencies, could be fundamentally different depending on the type of material and structure. Several authors have reported a positive correlation between temperature and natural frequencies for masonry towers ([31], [32], [33], [34]). On the other hand a negative correlation between these measures has been observed for some types of RC structures ([35], [36]). It is also important to note that these methods allow the detection of damage, but the quantitative estimation of structural performance (damage level) is hardly addressed by the scientific community.

1.2.2 Methods based on detection of transient response

The second group of methods is herein subdivided into two subgroups according to the expected frequency range of the transients related to damage. Typical Acoustic Emission (AE) methods detect elastic waves generated by the sudden release of internal energy [37],[38], [39], [40], [41], [42], [43], [44], [45]. This sudden release of internal energy occurs at the location of damage initiation and the expected frequency range of the generated elastic waves is in the order of tens to hundreds of kilohertz. AE finds a wide variety of applications: distinguishing different sources of damage in RC beams tested under flexural loading [46], testing failure with rebar corrosion [47], detection of yield and failure of post-tensioned concrete beams [48], in-situ evaluation of RC slabs [49], [50], [51]. AE is much more sensitive than vibrational methods, but one has to consider the fast distance attenuation of these high-frequency waves. This effect is especially pronounced for reinforced concrete structures [52] and a considerable obstacle when the goal is to detect damage within an entire civil engineering structure [53]. Detection of damage by capturing transients in the lower frequency ranges seems to be more applicable to civil engineering structures precisely because wave attenuation is not so pronounced. These transients are termed High-Frequency Transients (HFT) [54], but it should be pointed out that they are in the lower frequency range as compared to those in AE.

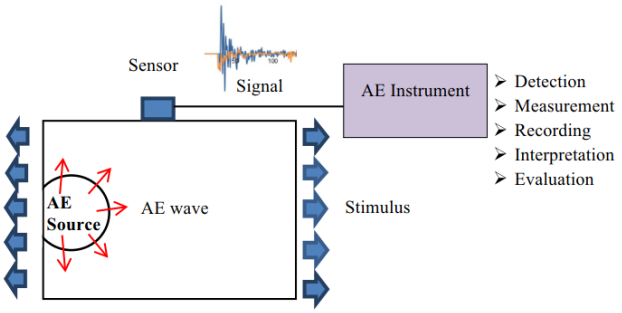

FIG. 1.2 Principles of AE [1]

1.2.3 Methods based on direct measurement of EDP's

In the third group of methods EDP's, such as strain or drift, are measured. An intersection between SHM and Performance-based Earthquake Engineering (PBEE) is drift ratio, therefore an accurate measurement of drift during the earthquake event would be informative of structural performance (Figure 1.4)[6]. The most widely implemented approach for estimation of drift ratio is double integration of the acceleration measured at the top and bottom of a structural element. Unfortunately there are issues with this procedure mainly related to the base correction requirement [12]. Base correction (adjustment) could be performed through low-cut filtering which would remove the low frequency noise [2]. Another option, amongst others, is to fit the velocity data with a linear or polynomial function and subtract the derivative of the fitted function from the recorded acceleration. In any case, the goal of the base correction (adjustment) procedure is to achieve zero velocity at the end of the record. The issues arise if the response of the structure is non-linear. The plastic part of the response and the resulting residual displacement are generally lost in the process of base correction. This leads to large discrepencies between actual and estimated drift. Smaller discrepancies are expected in the linear range of the response. Further drawbacks of the method is the subjectivity in the selection of the base correction approach and the relatively high instrumentation density required [55]. It should although be pointed out that there are other methods for direct measurement of drift (e.g. laser, GPS, LVDT), but a large number of structures are already instrumented with accelerometers. Therefore deducing drift, or any kind of damage sensitive feature, from accelerometer data is still desirable.

Discussion on the currently proposed procedure

The currently discussed damage estimation method attempts to address some of the main issues in the above summarized methods. On the one hand the method is more sensitive

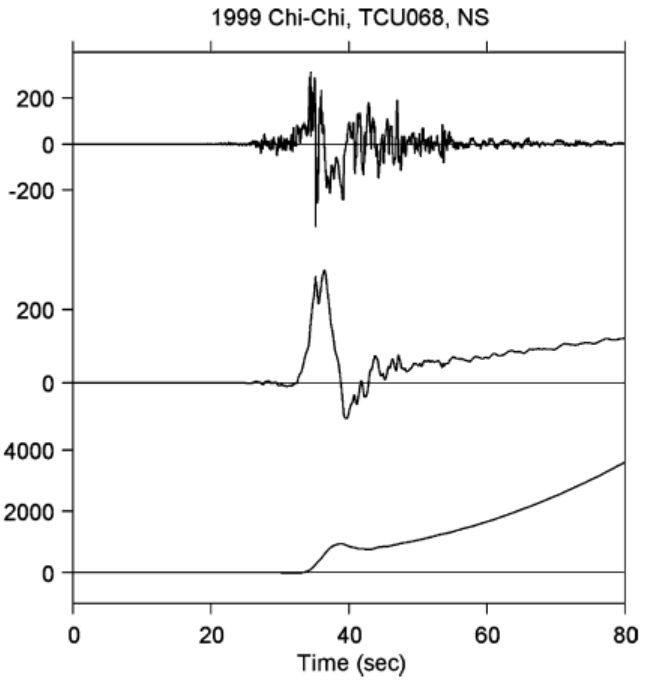

FIG. 1.3 Example of integration acceleration [2]

than traditional vibrational methods, since not permanent, but transient changes in the character of the response are detected. Also, the transients (HFT's) are examined in the lower frequency range, as compared to AE methods, where distance attenuation is not so critical. As already described in the thesis, the currently discussed damage indicator ($TRDI$) is directly related to the actual drift and this relation is kept even during non-linear response. The limitations of sparse instrumentation are also partially addressed by the possibility that the HFT's could be detected and the $TRDI$ calculated even if the instruments are not attached directly to the affected element. Actually, addressing the issue of sparse instrumentation is the most notable promise of the $TRDI$. Limitations of the method are discussed in depth in Section 6.1.1 with the main one being the requirement for a predominant first mode response.

J. Rodgers & M. Celebi [54] proposed a damage detection procedure based on detection of HFT's in steel structures. P. Bodin et al. [56] further analyzed the presence of HFT's during three earthquake response of the National Resources Building in Olympia, Washington. This thesis builds on the above work, but is limited to reinforced concrete structures and additionally attempts to express the level of damage in a quantitative manner.

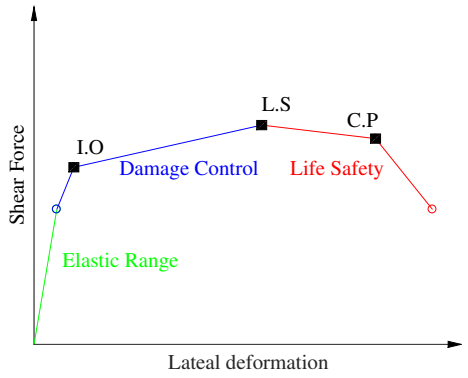

FIG. 1.4 Performance levels according to FEMA274 [3]

1.3 Detecting the HFT's

Let's first assume that we have the acceleration and strain response at arbitrary locations on a bridge pier (Figure 1.5). Initially we need to detect the HFT's in the response. As hyphotesized in [57] the cause of the HFT's is fixed-end rotation. Fixed-end rotation introduces a partial rigid body rotation in the response, which could be detected by the accelerometer (rigid body modes are not detected in the strain). In order to better distinguish the HFT's from to total acceleration we need to filter out the lower frequency response. A time-frequency representation of the acceleration could additionally aid the indentification of the transients. An additional indicator on knowing if a certain HFT is caused by damage is checking if the transient occurs shortly before a deformation extremum. The deformation extrema are obtained from the strain measurement. This choice will be justified in the next section.

Damage level is directly proportional to the length of the time-window between the arrival of the HFT and the consequent deformation extrema - τ (Figure 1.1). Damage "starts" to accumulate at the arrival time of the HFT and stops to accumulate at the first deformation extremum. The longer this time-window is the more damage the structure has accumulated. An additional important clarification in this chapter is that the damage is proportional to the above mentioned time-window, but ratioed to the length of the deformation cycle . Here we are refering to the length of the deformation cycle within which a HFT is observed.

An in-depth explanation of the response related to bond-slip could be found in [58], [59],[60], [61], [62], [63], [64], [65], [66]. It is well established that bond-slip has a significant effect on structural response in the low frequency range. AE generated from bond-slip has also been researched by a number of authors [ref]. This paper puts more

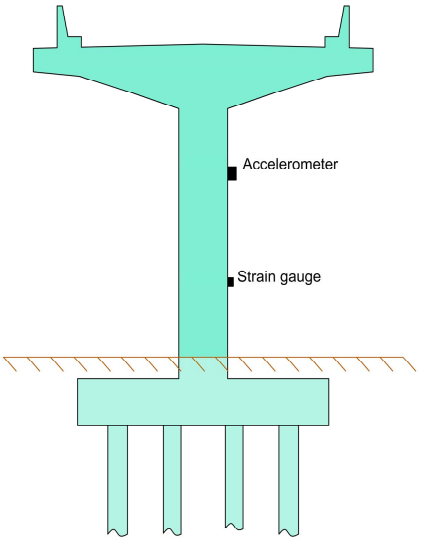

FIG. 1.5 Position of the instruments used for calculating the $TRDI$

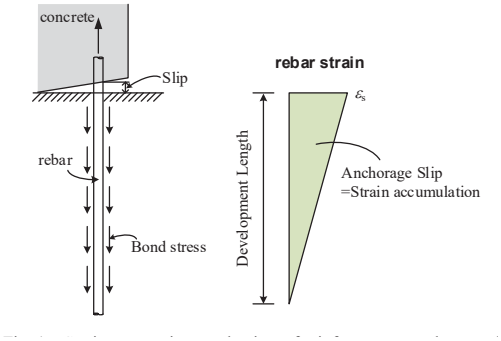

FIG. 1.6 Strain penetration and slip mechanism [4]

focus on the structural response within the order of dHz (HFT's) induced by bond-slip and the resulting fixed-end rotation.

Chapter 2

Mathematical formulation of the Time-Ratio Damage Indicator

2.1 Mathematical formulation of the Time-Ratio Damage Indicator

As a start lets set a goal of estimating the maximum drift of the structure during an earthquake response. The only input data available is the set of arrival times of the HFT's and the set of time instances of the deformation extrema. In order to deduce the maximum drift from this input several assumptions are made:

1. The structure has a predominant first mode response

2. Damage starts to accumulate at the arrival times of the HFT's

3. Damage stops to accumulate at the deformation extrema

4. HFT's occur once the previous maximum drift is exceeded with the exception of the first HFT

5. The calculation of the maximum drift, according to the above assumptions, could be done independently per direction of deformation

Figure 2.1 helps us visualize the above assumptions and deduce the expression for the maximum drift and the $TRDI$. The top part of the figure represents the idealized deformation of the structure only in one direction. Both idealized drift (Θ) and strain (ϵ) are plotted with the goal of describing their expected relationship. Additionally only the half cycles with HFT's present are shown and squeezed together. The bottom part of the figure is an idealized representation of the expected transient part of the acceleration response (α).

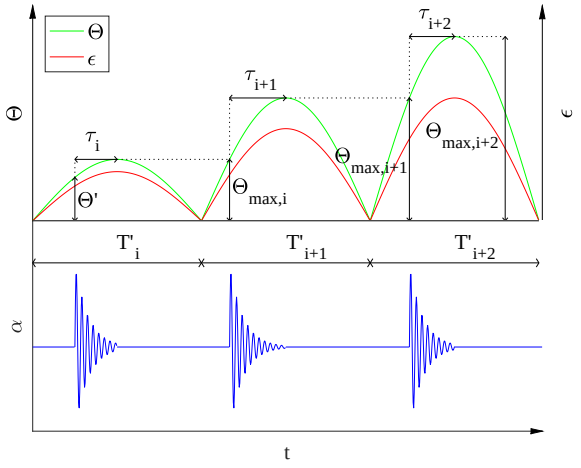

FIG. 2.1 Visualizing the $TRDI$

If the value of Θ' is known then we could obtain $\Theta_{max,i}$ with the following relation:

$$\Theta_{max,i} = \frac{\Theta'}{sin\pi(\frac{1}{2} - \frac{\tau_i}{T_i'})} \tag{2.1}$$

,where Θ' is the drift at the first HFT, $\Theta_{max,i}$ is the maximum drift in the ı-th half cycle, T_i' is the length of the ı-th half cycle and τ_i is the time difference between the deformation extremum and the arrival time of the HFT in the ı-th half cycle.

The maximum value of the drift in the following cycle with a HFT present is:

$$\Theta_{max,i+1} = \Theta_{max,i}\{csc\pi(\frac{1}{2} - \frac{\tau_{i+1}}{T_{i+1}'})\} \tag{2.2}$$

The maximum value of the drift after the last HFT is:

$$\Theta_{max,N} = \Theta' \prod_{i=1}^{N}\{csc\pi(\frac{1}{2} - \frac{\tau_{i+1}}{T_{i+1}'})\} \tag{2.3}$$

where N is the number of HFT's. The damage indicator $TRDI$ is defined as:

$$TRDI = \prod_{i=1}^{N} \{csc\pi(\frac{1}{2} - \frac{\tau_{i+1}}{T'_{i+1}})\} \tag{2.4}$$

and gives the ratio between the maximum drift of the structure and the drift at at the first HFT.

The naming of the damage indicator (Time Ratio Damage Indicator) follows from the variable in equation 2.4, which is a ratio between the time segments τ_i and T'_i. Here drift is the chosen EDP, but the estimation of other EDP's using the above equations is conceivable.

$TRDI$, as deduced in equation 2.4, is defined only for a discrete set of points (the deformation extrema). In order not to miss characteristic points of response (e.g. initiation of yielding) a continuous time function of the $TRDI$ would also have to be deduced. We start with the continuous time function of the drift:

$$\Theta(\tau)_i = \Theta_{max,i} \sin \pi(\frac{1}{2} - \frac{\tau}{T'_i}) \tag{2.5}$$

After substituting $\Theta_{max,i}$ with the expression in equation 2.3 and dividing by Θ' we obtain the following:

$$\frac{\Theta(\tau)_i}{\Theta'} = \prod_{i=1}^{N} \{csc\pi(\frac{1}{2} - \frac{\tau_{i+1}}{T'_{i+1}})\} \sin \pi(\frac{1}{2} - \frac{\tau}{T'_i}) \tag{2.6}$$

therefore:

$$TRDI(\tau)_i = TRDI_i \sin \pi(\frac{1}{2} - \frac{\tau}{T'_i}) \tag{2.7}$$

If we assume to have the strain response at an arbitrary location along the height of the structure (e.g. from measurement), then we could plot the relationship between $\epsilon(\tau)$ and $TRDI(\tau)$ (Figure 2.2):

Since the $TRDI$ is directly related to drift a linear relationship between the $TRDI$ and ϵ indicates that the relationship between Θ and ϵ is also linear. This implies that the structural response is still in the linear range. Non-linear response and hence damage is expected once the linear relationship between the above parameters is broken.

If $TRDI_y$, which is the $TRDI$ at yielding, is identified from the ϵ - $TRDI$ relationship, then the ductility factor μ_N after the last HFT could be expressed in the following way:

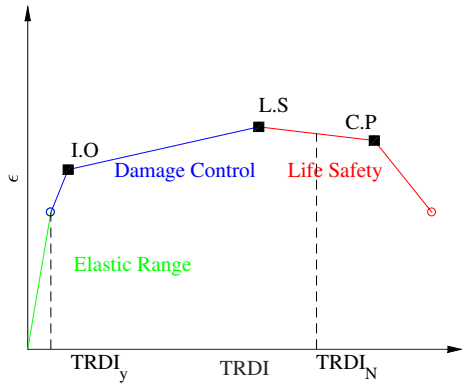

FIG. 2.2 Idealized representation of TRDI vs. strain

$$\mu_N = \frac{TRDI_N}{TRDI_y} = \frac{\Theta_{max,N}}{\cancel{\Theta}} \frac{\cancel{\Theta}^{1}}{\Theta_y} \tag{2.8}$$

From equation 2.8 it follows that no actual drift measurements are required for the evaluation of structural performance. μ_N provides sufficient insight to the performance of the structure and could be deduced only from the calculated $TRDI$'s.

Chapter 3

The loss of linear proportionality as indicative of damage

In this chapter the concept of damage detection based on loss of linear proportionality between response parameters is further elaborated on. We first touched upon this by hypothesizing on the relationship between the TRDI and strain, which will later be demonstrated on experimental data (Chapter 5). As damage accumulates in a structure during earthquake ground motion loss of linear proportionality will occur between response parameters, such as drift and strain, acceleration and drift, sets of strains, etc. This is an almost trivial claim, but nevertheless rarely discussed in the realm of research on earthquake induced damage. There is a large body of research on the application of the transmissibility function in vibration based SHM . In essence the change in proportionality between the amplitudes of two measured response parameters is tracked in the frequency domain. In the frequency domain usually the coherence function is implemented ([67], [68]). This approach has shown satisfactory results for monitoring data from long term vibration under ambient excitation (e.g. [69], [70], [71], [72], [73], [74]). When we have transient excitations, such as those expected during an earthquake event, the accuracy in the estimated frequency content within the time-window of the transient event drops. This accuracy reduction could mask the damage induced response, especially in the early stages of damage. Such an effect is highly undesirable, since most of the value of information from a SHM system is contained in enabling preventive measures. Therefore detecting damage at the early stages is key. For this reason the approach implemented in this thesis keeps the data in the time domain. This is accompanied with trade-offs, which will shortly be emphasized.

3.1 Section

The chosen approach consists in tracking the loss of linear proportionality between the recorded responses from a pair of strain gauges during earthquake induced shaking of a structure. The linearity between the two responses is measured with Pearson's correlation coefficient. The value of the correlation coefficient is expected to decrease as a structure accumulates damage and plastic hinges are formed. This expectation will not be always realized, as it depends on the relative location of the instruments. For example, if we have a single column with one "strain gauge" (marked with ■) installed below the expected location of the plastic hinge and the other installed above (3.2(a)) then we will observe a loss of linear proportionality between the two and a drop in the correlation coefficient. On the other hand if both strain gauges are installed well above the plastic hinge there will be no loss of linear proportionality between the two strain gauges even if significant damage occurs. Another example is a column fixed at both ends, a plastic hinge at one of the supports and both strain gauges placed on one side of the plastic hinge (3.2(b)). In this case, as the damage accumulates in the plastic hinge, the moment will be redistributed and linear proportionality between the strain responses will be lost. This would also be the case if there are hinges at both end (3.2(c)), but only if the response of the hinges is not exactly identical. All of the above claims will correspond well to reality only if the monitored structure or structural element deforms according to a single deformation mode or deforms in more than one deformation mode, but with no phase-shift in the response between the different modes. In case the response is in more than one deformation mode and there is a phase-shift between the modes the relationship between two response quantities will not be linearly proportional even if the structure remains linear. The following section provides more clarity by demonstrating this concept on a simple frame structure.

3.2 Numerical model

A numerical model of a simple frame was built for the purpose of demonstrating the detection of hinge formations in the beams with a pair of strain gauges. The material and geometric properties of the model are shown on Figure 3.1. Base excitation is introduced through an artificially generated accelerogram matching the spectrum on Figure 3.3.The analysis was performed with the ASE module of Sofistik [75]. The artificial accelerogram was generated according to the procedure in [76]. Time integration is according to the $HHT-\alpha$ method with $\alpha = 0.3$ [77]. Plastic hinges with moment-rotation relationships

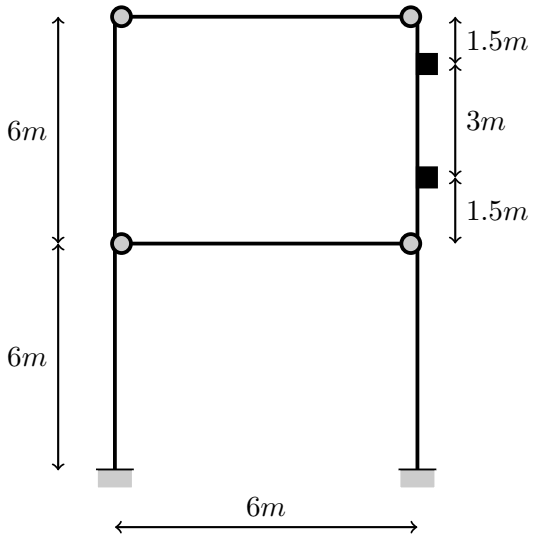

FIG. 3.1 Frame geometry

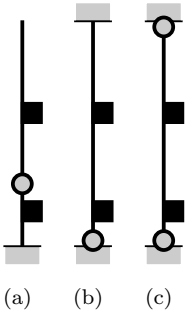

FIG. 3.2 Cases of relative location between plastic hinges and instruments

according to Figure 3.4 are assigned to the ends of the beams. The locations of the strain measurements are as shown on Figure 3.1.

First, the results from an entirely linear analysis of the frame are shown on Figures 3.5 and 3.6. As expected the relationship between the strains remains linear.

Figures 3.8 and 3.9 show the results from a non-linear analysis of the strain response in time of before the yield moment is reached. As expected the relationship between the strains is linearly proportional. Therefore by just looking at the relationship between the two strains we could conclude that there is no plastification at the hinges. Now let's plot the strains over the entire response of the frame. It is clear that the linear proportionality between the strains is broken, which is expected since the yield moment at the beam-column connection is exceeded. Although we could directly observe the presence of linearity between the measured strains it would be advantageous to quantify it. Pearson's correlation coefficient is used for this purpose (eq. 3.1). The correlation between the two strain responses from the non-linear analysis is calculated (Figure 3.10.

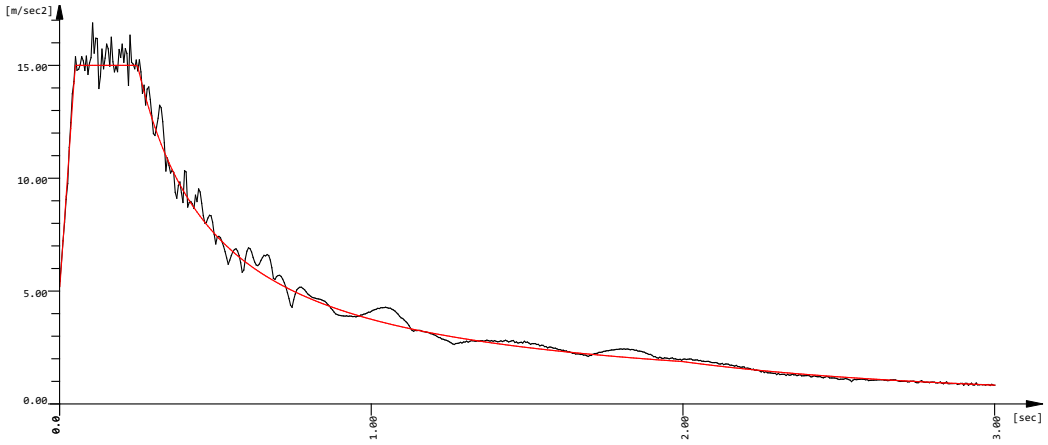

FIG. 3.3 Simulated accelerogram

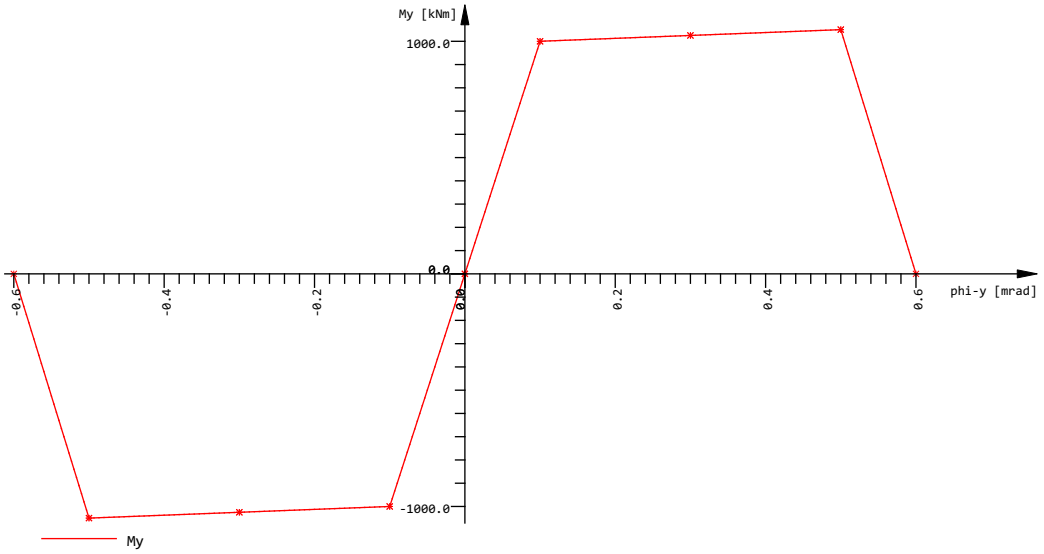

FIG. 3.4 Moment rotation relationship for the plastic hinges

$$r = \frac{\sum_{i=1}^{n}(x_i - \overline{x})(y_i - \overline{y})}{\sqrt{\sum_{i=1}^{n}(x_i - \overline{x})^2(y_i - \overline{y})^2}} \tag{3.1}$$

The correlation is calculated for a moving window of 500 samples from each strain measure and an overlap of 499 samples. The size of the window should be large enough so that samples within the order of one deformation cycle are included. Misleading results could be obtained in case of a window size which is too small due to some spurious transient responses. A window size which is too large might not be informative, as it does not allow the accurate tracking of change in correlation.

Below we plot strain vs. strain from frame structure

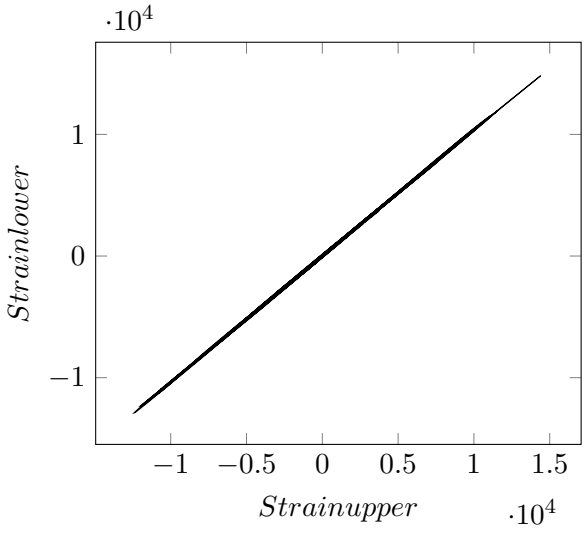

FIG. 3.5 Lower strain vs. Upper strain from the linear frame analysis

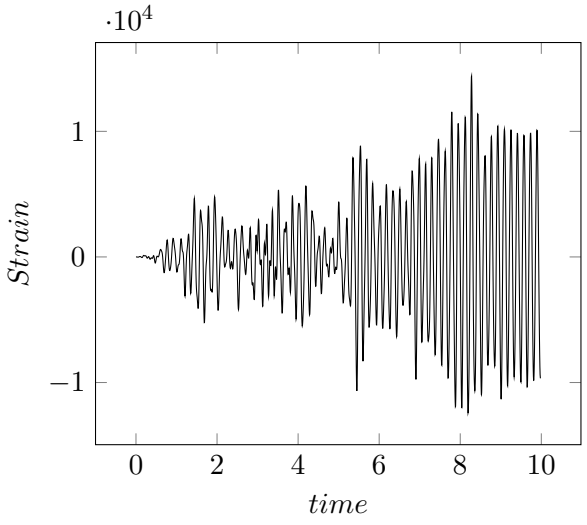

FIG. 3.6 Lower strain vs. time from the linear frame analysis

Below we plot the correlation factor (R) vs. time for the model of the frame

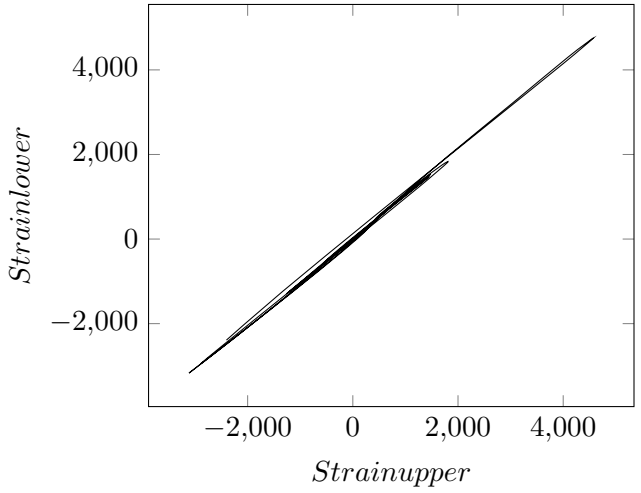

FIG. 3.7 Lower strain vs. Upper strain from the non-linear frame analysis before hinge plastification

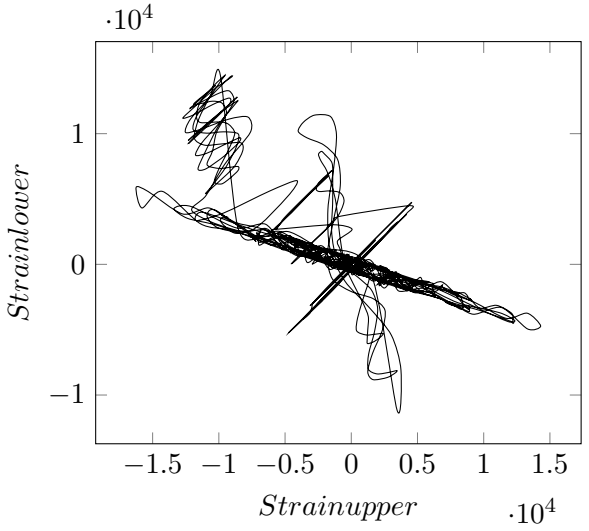

FIG. 3.8 Lower strain vs. Upper strain from the non-linear frame analysis for the entire record

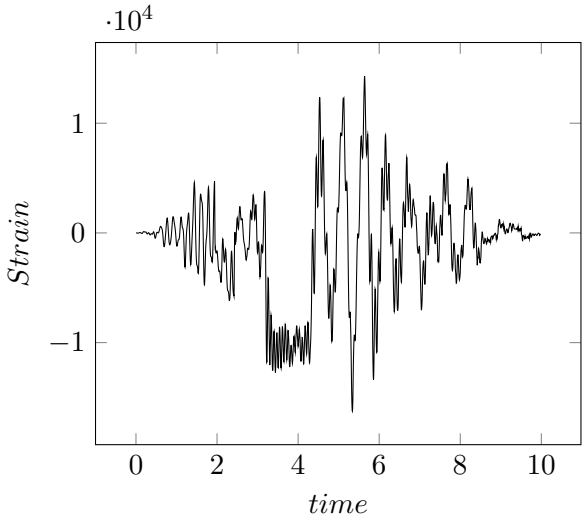

FIG. 3.9 Lower strain vs. time from the non-linear frame analysis

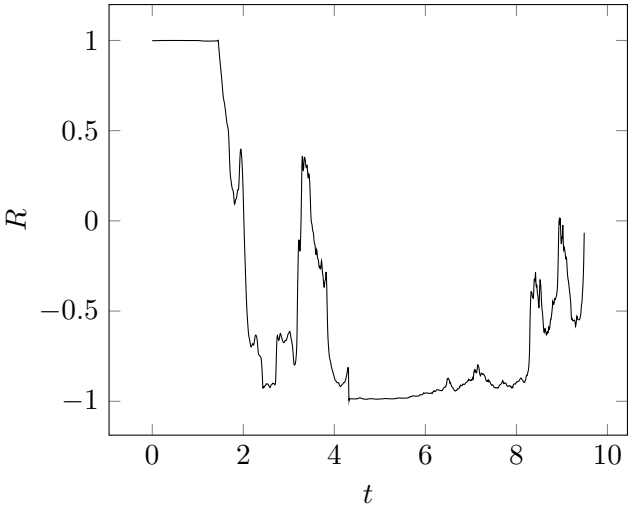

FIG. 3.10 Correlation factor vs. time for model of frame

3.3 Discussion

The approach described within this chapter could be implemented for detection of yield in bridge piers and elements in building during earthquake ground motion. Other implementations are of course also conceivable. Detecting yielding according to the above approach might hold some advantages compared to detecting the yield from drift ratio estimations. Drift is most often deduced from double integration of acceleration data, which as already discussed in this thesis, is not always accurate. We have to also consider that measuring only the drift is not sufficient for judging if there is yielding or not. The yield capacity of the given element has to be also known. Uncertainty is always present when estimating the yield capacity [78], especially if the physical and mechanical properties are not well known and \or there is already some damage present (e.g.corrosion). In this sense there is uncertainty in both the demand (estimated drift from acceleration data) and the yield capacity. It could be argued that these uncertainties are eliminated when the loss of linear proportionality is detected in a direct manner.

Initially the correlation coefficient on Figure 3.10 remains relatively constant at one. After around second 1.8 the yielding moment is exceeded in the correlation starts the decrease. The correlation coefficient tends to decrease, but this is not strict. We observe also increases in the correlation coefficient. Such a behaviour is explained by the expectation that the correlation coefficient will drop during the reduction is stiffness. If there is no further reduction is stiffness the system is again linearly proportional, but with a different stiffness, which implies an increase in the correlation coefficient. For extreme levels of damage a negative correlation could also be observed, as in the examined case above.

Chapter 4

Description of the experimental set-ups

4.1 Description of the Shaking Table Experiment performed in U.C. San Diego

4.1.1 Geometry and material properties U.C. San Diego experiment

Design and detailing of the 1.22 meter diameter column with 7.31 meter height were according to Caltrans seismic design guidelines [79]. The column was subjected to 10 significant ground motions (EQ's) - Table 4.1. Excitations by the shaking table were uni-axial in the East-West direction. The intent was nonlinear response with predominant flexural behavior. Longitudinal reinforcement consisted of 18 bars with a diameter of 35.8 mm (reinforcement ratio 1.55%). The column was reinforced in the transverse direction with 15.9 mm butt-welded double hoops spaced at 152 mm (Annex A). The average yield stress of the longitudinal reinforcement was 518.5 MPa. No yield plateu was observed from the testing of the transverse reinforcement and the average value of the ultimate tensile stress was 592.2 MPa. The average compessive strenght of the concrete was 40.9 MPa. Axial load was 2.52 MN.

Two inclined steel columns and two arched steel towers served as safety restraints (Figure 4.1). Drift was directly measured with string potentiometers attached between the stiff steel structure (the arched towers) and the column.

Detailed reinforcement plans of the columns are attached in Annex A.

FIG. 4.1 Test set-up [5]

Base excitations

TABLE 4.1
DESCRIPTION OF SHAKE TABLE TEST AND OBSERVED DAMAGE FROM THE U.C. SAN DIEGO EXPERIMENT

Ground motion	Description	Notes on outcome
EQ1	Agnew State Hospital record 1989 Loma Prieta	Residual cracks footing-to-column interface 0.1 mm
EQ2	Coralitos 1989 Loma Prieta earthquake	Residual cracks in the column are marked
EQ3	Los Gatos Center 1989 Loma Prieta earthquake	Spalling on the West face of the column
EQ4	Coralitos 1989 Loma Prieta earthquake	More spalling on the West face
EQ5	Takatori at -80% amplitude 1995 Kobe earthquake	Continued spalling. Longitudinal bars are visible
EQ6	Los Gatos Center 1989 Loma Prieta earthquake	-not available
EQ7	Takatori at 100% amplitude 1995 Kobe earthquake	-not available
EQ8	Takatori at -120% amplitude 1995 Kobe earthquake	Two longitudinal rebar fracture East face
EQ9	Takatori at 120% amplitude 1995 Kobe earthquake	Longitudinal rebar fracture on East and West face
EQ10	Takatori at 120% amplitude 1995 Kobe earthquake	Impacted the East safety restraint

4.1.2 Instrumentation

Locations of instruments relevant for the data used in this research are given in Annex C.

4.2 Description of the Shaking Table Experiment performed at the University of Patras

4.2.1 Geometry and material properties University of Patras experiment

Two shaking table test of reinforced concrete bridge piers were performed for the purpose of validating the above procedure for damage detection and estimation. Two columns with circular cross-sections were tested - one with a 30 cm diameter cross-section and one with a 40 cm. The general geometry, material properties and reinforcement of the columns are presented in Table 4.2. Detailed reinforcement plans of the columns are attached in Annex B. The base excitations chosen for the experiment are described in section 4.2.2. The observed damage is given in Section 5.3.4. The columns are designed according to EN1998 [80].

FIG. 4.2 Patras column

TABLE 4.2
DESCRIPTION OF COLUMNS FOR THE EXPERIMENT AT THE UNIVERSITY OF PATRAS

Column	Length pl.hinge [cm]	Concrete class	Steel class	Reinforcement ratio	Concrete cover [cm]
D30	55	C25/30	B500 C	1.44%	3
D40	55	C25/30	B500 C	0.81%	3

4.2.2 Base excitations

The chosen earthquake record is from the Los Angeles - 116th St. School recorded during the Whittier Earthquake on October 1st 1997 (Figures 4.6(a) and 4.6(b)). For the column with the $30cm$ diameter the excitation is scaled to a PGA of $0.4g$ and for the column with a $40cm$ diameter the excitation is scaled up to $0.5g$. Before testing the column on the shaking table a test with two block with masses equal to those of the

FIG. 4.3 Patras column

FIG. 4.4 Patras column

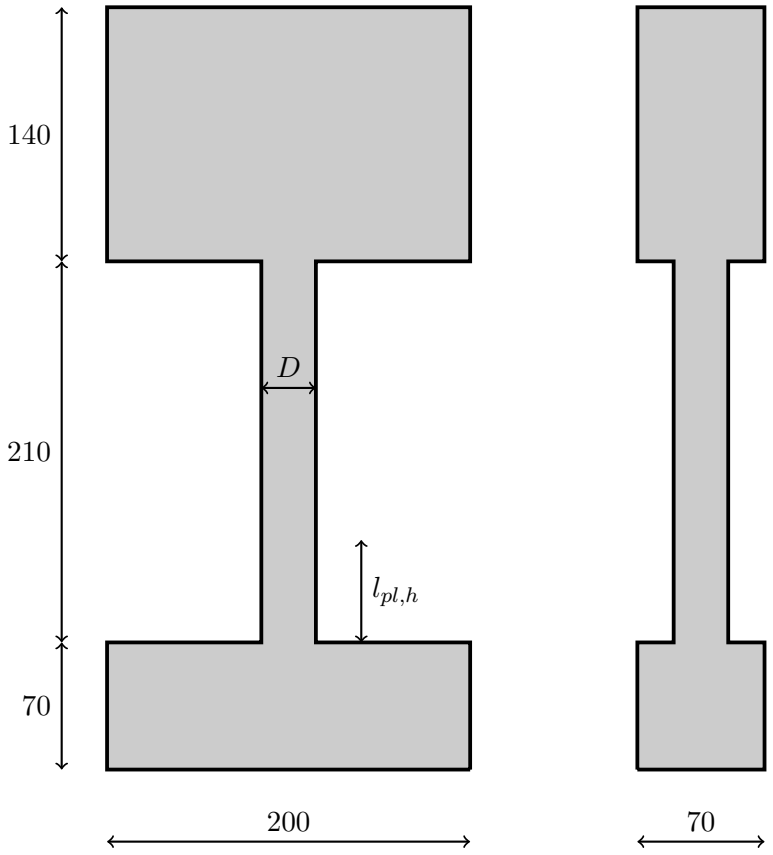

FIG. 4.5 Column geometry in centimeter

columns were performed. The purpose of this was to fine tune the shaking table in order to achieve the desired base excitations.

Both column are excited sequently by 5 base accelerations, which are scaled values of the record on Figure 4.6(a). The records are first scaled to 25% of the above given PGAs for both columns, then 50%, 75%, 100% and 125%. This was done to avoid risks of any sudden collapses.

4.2.3 Instrumentation

The columns were instrumented with 32 strain gauges and 4 accelerometers each. All strain gauges were located on the outer most longitudinal reinforcement bars of the columns. Precise locations of the instruments are given in Annex D.

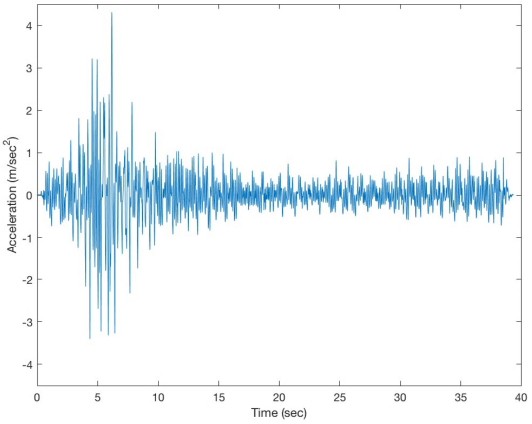

(a) Excitation in the time domain

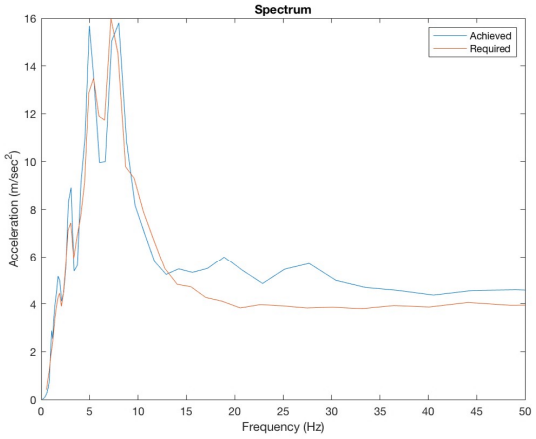

(b) Excitation in the frequency domain

FIG. 4.6 Base excitation from the experiment at the University of Patras

Chapter 5

Results

5.1 Results for U.C. San Diego experiment

In this section a case-study calculation of the $TRDI$ is demonstrated on an output data from an experimental reinforced concrete column (Fig. 4.1) tested on a shaking table [5]. The test was conducted on the George E. Brown, Jr Network for Earthquake Engineering Simulations shake table at U.C. San Diego. The goal of the case study is to demonstrate the relation between the $TRDI$ and the ductility factor. Additionally a step-by-step procedure is provided for the calculation of the $TRDI$.

5.1.1 Calculating the TRDI

Several processing steps are required before the calculation of the $TRDI$ is possible. First the arrival times of the HFT's have to be detected. This could be done by examination of the acceleration response of the monitored structure. A high-pass filter should be applied with a cut-off frequency high enough so that the response governed by the first several modes (the global modes) is removed. In this case a Butterworth filter [81] with a cut-off frequency of 25 Hz was selected. In this way the transients are more clearly distinguished in the time domain. In addition a time-frequency representation of the signal could be obtained. In this representation the transients should again be distinguishable. For this case-study a Short-Time Fourier Transform (STFT) was implemented [82].

Next, the time instances of the drift extrema should be identified. One could use strain gauge data, since the extrema of strain and the extrema of the drift match in time. Also, a Linear Variable Deformation Transformer (LVDT) device could be attached at

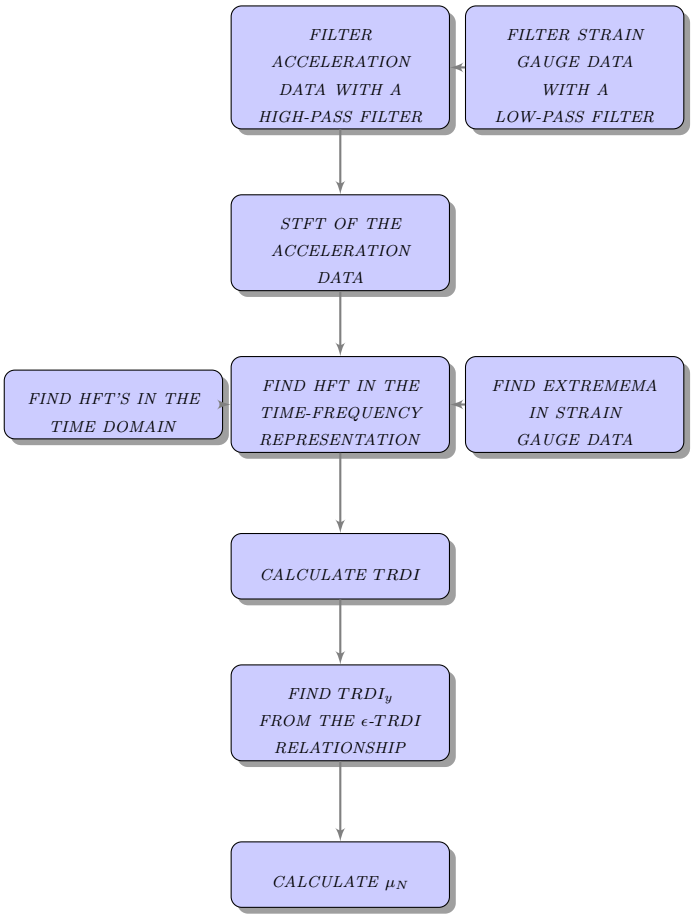

FIG. 5.1 Processing steps required for the calculation of μ_N

an arbitrary location along the height of the column. If such data is not available, then the times instances of the deformation extrema could be found from the relative displacement calculated by double integration of top and bottom acceleration. The key here is to perform the adjustment of the top and bottom velocities (obtained from integration) with a baseline correction and not a high-pass filter. The extrema of the drift obtained from such an adjustment are expected to match in time with the extrema of the actual drift, although the amplitudes would not match.

The above processing steps are a recommendation, but one could obtain the arrival times of the HFT's and the extrema with a different processing approach. For clarification a block diagram with the proposed processing steps is given in Figure 5.1.

Measurement output was used from accelerometer ACW6E for capturing HFT's and strain gauge data from GLES08E was used for measuring time instances of deformation extrema (Figure 5.3). It was necessary to filter the strain-gauge data with a low-pass

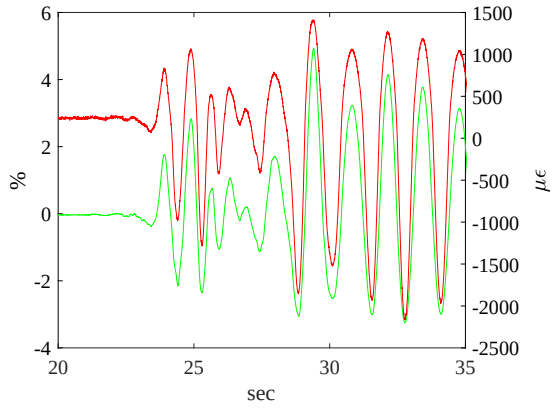

(a) EQ 3

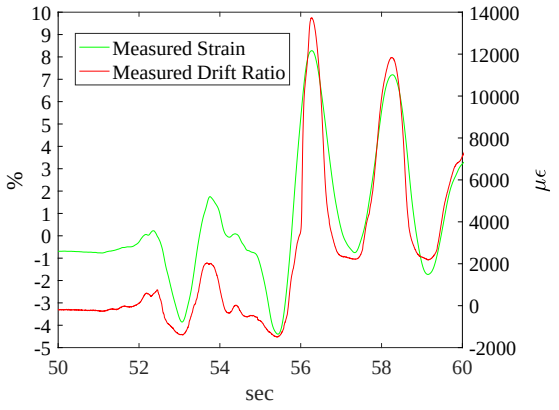

(b) EQ 8

FIG. 5.2 Comparing strain with drift ratio

filter (cut-off at 25 Hz), in order to have a smooth curve before the identification of the extrema.

The purpose of the strain gauge is to capture the time instances of EDP extrema. For this case-study drift ratio was the considered EDP. It is expected that the extrema of the drift ratio and strain coincide in time, therefore the strain gauge is suitable for capturing time instances of drift ratio extrema. The match in time between strain and drift extrema is confirmed by the current experiment (Figure 5.2).

It was observed that only the accelerometers are able to capture the HFT's, even though the strain gauge data was sampled at the same rate. The reason for this could be a transient rigid rotation (aka. end-rotation) of the column about the location of damage at the time instances of damage initiation. Rigid body response could be captured only with an accelerometer and not a strain gauge. On the other hand, a single accelerometer can not capture relative deformation extrema and therefore a strain gauge is required. The exact damage mechanism causing the HFT's is later elaborated on in the text.

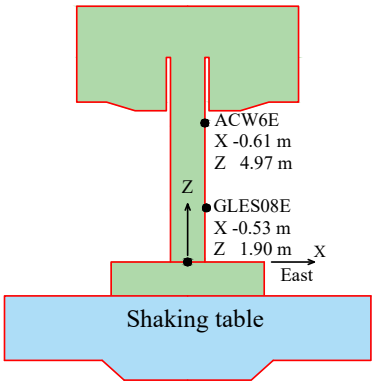

FIG. 5.3 Position of the instruments used for calculating the $TRDI$

5.1.2 Calculating the TRDI

The goal is to estimate the maximum drift ratio in each half-cycle of observed HFT and compare the estimation with the drift measured with spring potentiometers. Therefore it is required to calculate the $TRDI$ for each half-cycle with observed damage an multiply it with the drift ratio at the time of the first observed HFT (Θ'). In a real-case scenario Θ' would not be available (further discussed in Section 6.1.1), but in this case this value was taken from the potentiometer measurements and used as input to estimate the rest of the drifts.

The drift and acceleration are herein also plotted.

First the arrival times of the HFT's are located in time from the time-frequency representation and time-domain representation (Fig.5.4, Fig.5.5). Deformation extrema are identified from the filtered strain gauge data. τ_i and T_i' are obtained according to the following formulas:

$$\tau_i = t_{2,i} - t_{d,i} \tag{5.1}$$

$$T_i' = t_{2,i} - t_{1,i} \tag{5.2}$$

, where $t_{d,i}$ is the arrival time of the HFT in the ı-th half-cycle. $t_{1,i}$ and $t_{2,i}$ are the time instances of response extrema correspondingly before and after the HFT in the ı-th half-cycle (Figure 5.5).

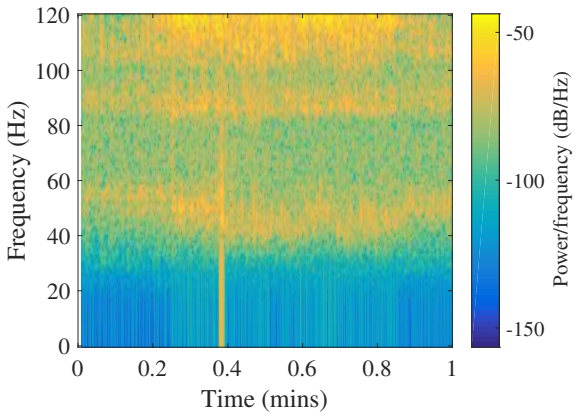

(a) EQ 1

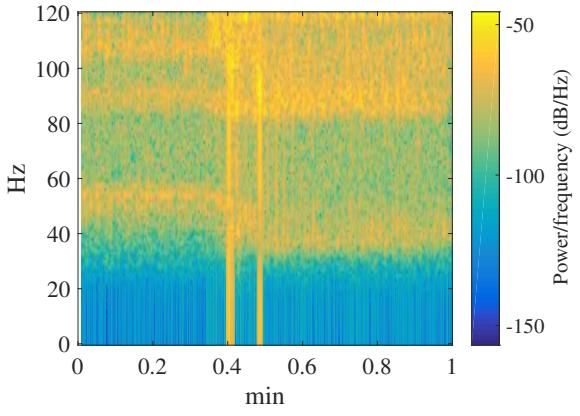

(b) EQ 2

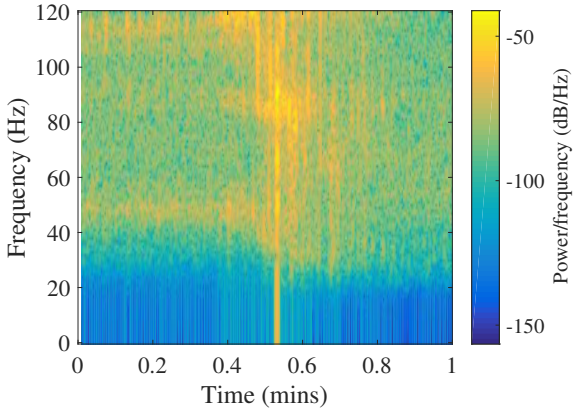

(c) EQ 3

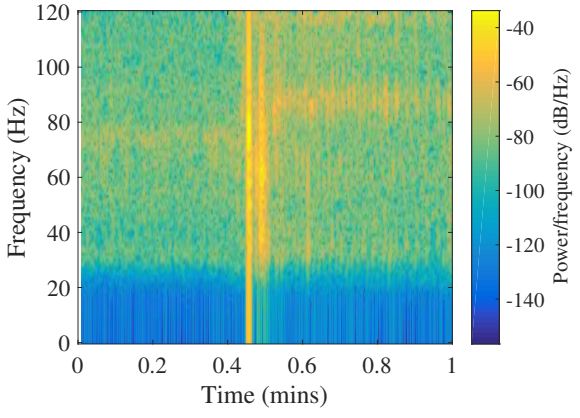

(d) EQ 4

FIG. 5.4 Spectrograms of the filtered acccelerations

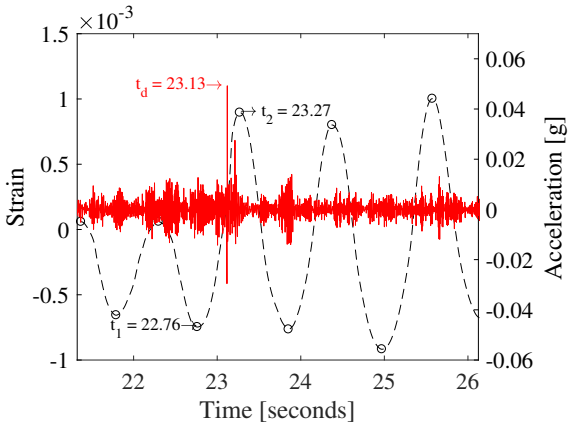

(a) EQ 1

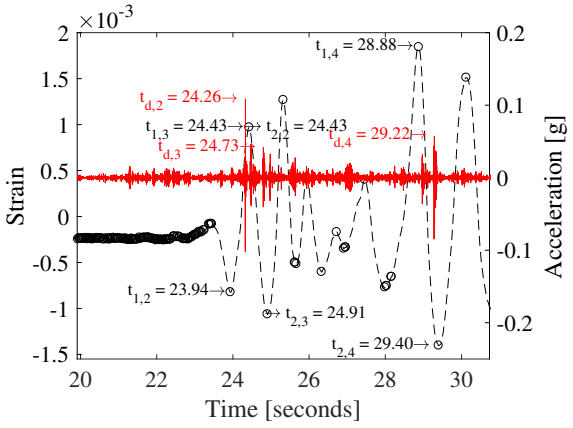

(b) EQ 2

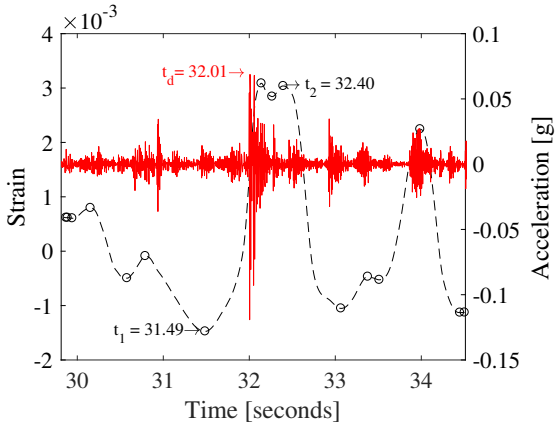

(c) EQ 3

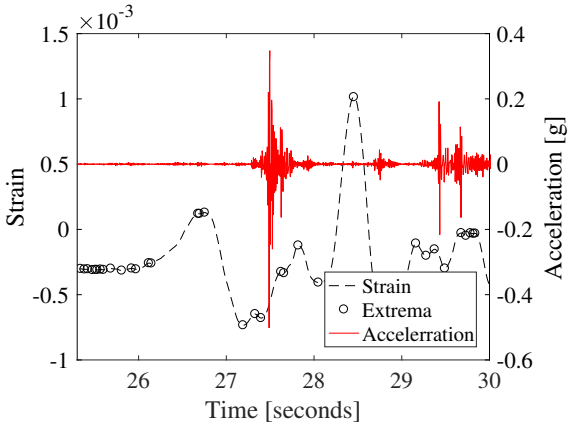

(d) EQ 4

FIG. 5.5 Spectrograms of the filtered acccelerations

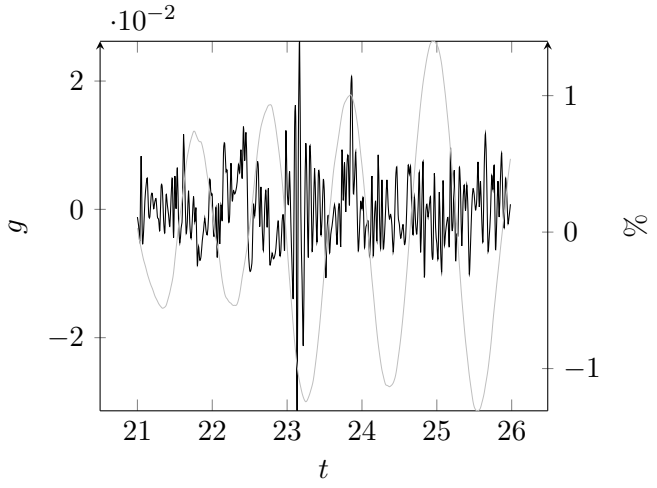

FIG. 5.6 Filtered acceleration and drift, EQ1

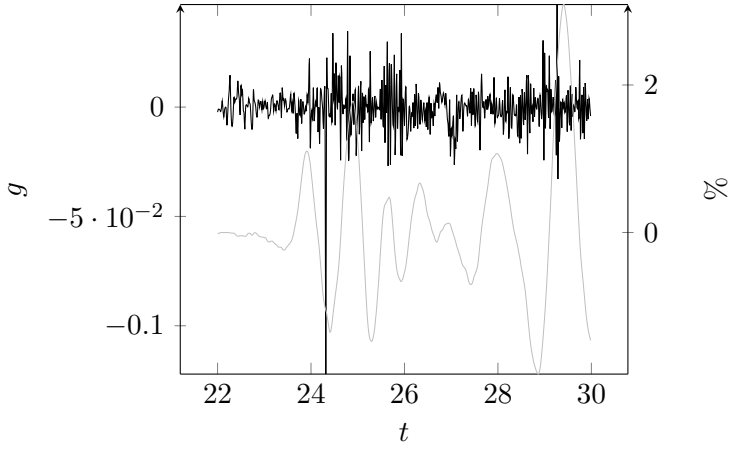

FIG. 5.7 Filtered acceleration and drift, EQ2

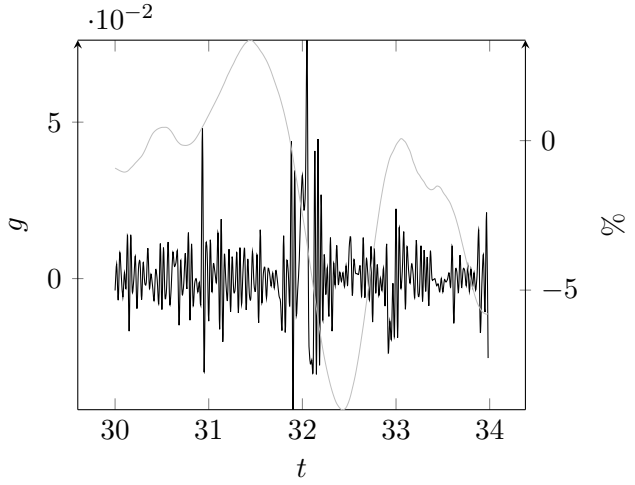

FIG. 5.8 Filtered acceleration and drift, EQ3

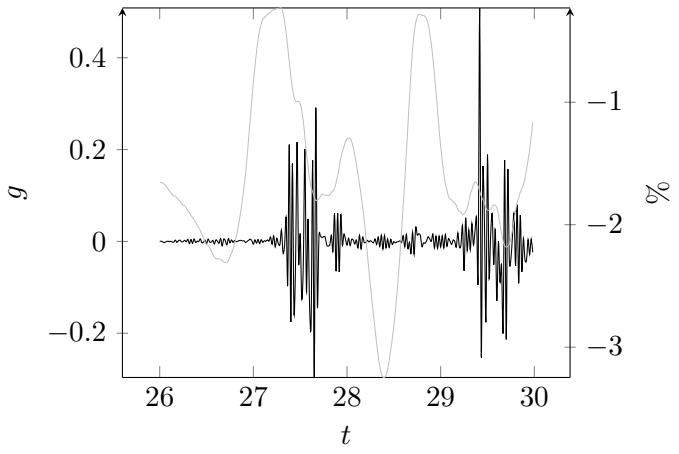

FIG. 5.9 Filtered acceleration and drift, EQ4

TABLE 5.1
CALCULATION OF TRDI FOR EACH EQ

EQ #	EQ1	EQ2	EQ2	EQ2	EQ3
HFT #	1	2	3	4	5
t_1 [s]	22.762	23.937	24.429	28.879	31.487
t_2 [s]	23.271	24.429	24.910	29.400	32.396
t_d [s]	23.125	24.333	24.80	29.26	32.010
τ_i [s]	0.146	0.096	0.110	0.140	0.386
T_i' [s]	0.509	0.492	0.481	0.521	0.909
$TRDI_{i,p}$	1.611	1.967	1.967	1.967	8.390
$TRDI_{i,n}$	0.000	0.000	−1.328	−1.999	−1.999
$\Theta'(t_d)$ [%]	0.526	0.690	−0.908	−1.000	0.760
$\Theta'_{max,i}$ [%]	0.710	0.790	−1.040	−1.760	5.050
$\Theta_{max,i}$ [%]	0.847	1.036	−1.206	−1.816	4.417

Finally the results are summarized on Figure 5.10 and Table 5.1. $\Theta'_{max,i}$ is the maximum drift ratio per cycle measured with spring potentiometers and serves as comparison with the estimated maximum drift ratio ($\Theta_{max,i}$).

There are 5 HFT's observed. The plus and minus signs in 5.1 indicate the direction of deformation of the column. For each direction of deformation the EDP (drift ratio) is estimated separately, which is in accordance with assumption iv) (Section 2.1).

5.1.2.1 On the estimation of ductility demand

The performance of the structure is deduced from the ductility factor obtained from equation 2.8 giving the ratio between the experienced drift and the drift at yielding. Conclusions on the performance of the structure are to be made from this ratio, therefore an explicit calculation of the drift is not required. The question here is how to evaluate

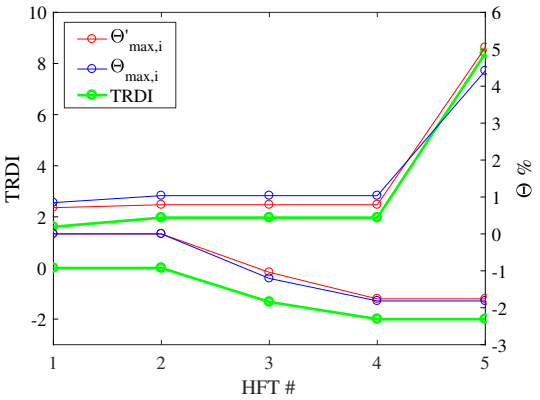

FIG. 5.10 TRDI versus Drift Ratio

$TRDI_y$. $TRDI_y$ is reached when the drift at yielding Θ_y is reached. At this point it is expected that the linear relationship between strain and drift would be lost. Since the relationship between drift and the $TRDI$ is related by a constant, it follows that the linear relationship between the strain ϵ at an arbitrary location and the $TRDI$ would also be lost.

In order to clarify to above preposition first the measured strain (strain gauge GLES08E) for each time window between t_d and $t_{2,i}$ is plotted (Figures 5.11 and 5.14). Next, for the same time windows we plot the $TRDI$. Plotting these graphs is not necessary, but useful for the better grasping of the problem. The important relationship is the one between the $TRDI$ and strain (Figures 5.13 and 5.16). From Figures 5.13 and 5.16 it could be observed that the column enters the nonlinear range only in the "positive" direction of deformation. In the "negative" direction the response quantities ($TRDI$ and strain) remain linearly proportional, therefore the column should still be in the linear range. This is further addressed in Section 6.1.1. It is noticed that there are jumps in the $TRDI$ and strain plots (e.g. in Figure 5.16 and 5.14). This occurs since the arrival times of the HFT's are not captured at the exact time of damage initiation, therefore breaking the logical continuity in the strain.

From Figure 5.13 it could be concluded that the structure has gone into the nonlinear range. The estimated $TRDI_y$ and the maximum $TRDI$ are correspondingly ≈ 2.30 and 8.39. Therefore the ductility factor according to equation 2.8 is $\mu_N = 3.65$. A $TRDI_y$ of 2.30 corresponds to a drift of 1.21%, which is $\Theta' TRDI_y$. From the experimental force-deformation curve (Figure 5.17) it could be observed that the structure yields at about the same drift, which leads to an experimental $\mu'_N \approx 4.17$.

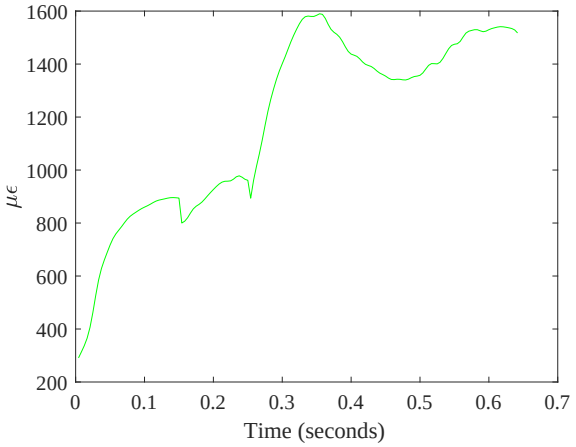

FIG. 5.11 Strain vs. Time in positive direction of deformation

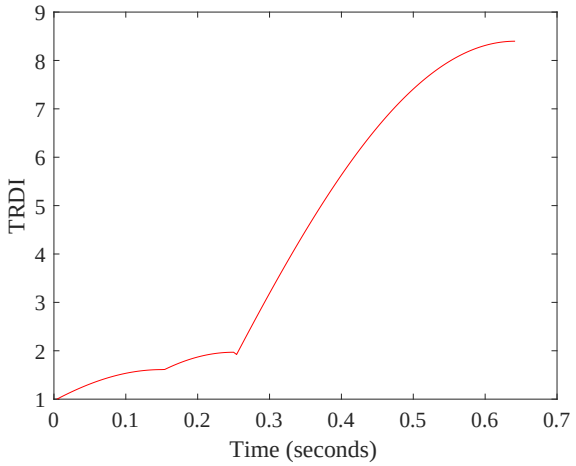

FIG. 5.12 TRDI vs. Time in positive direction of deformation

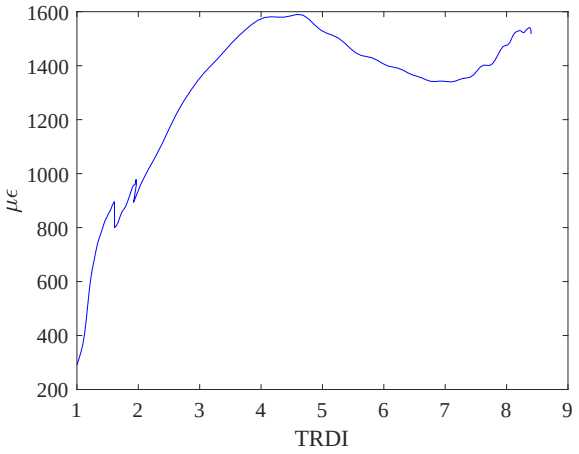

FIG. 5.13 Strain vs. TRDI in positive direction of deformation

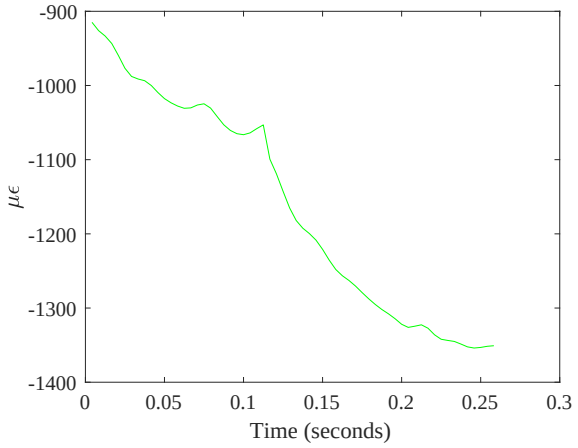

FIG. 5.14 Strain vs. Time in negative direction of deformation

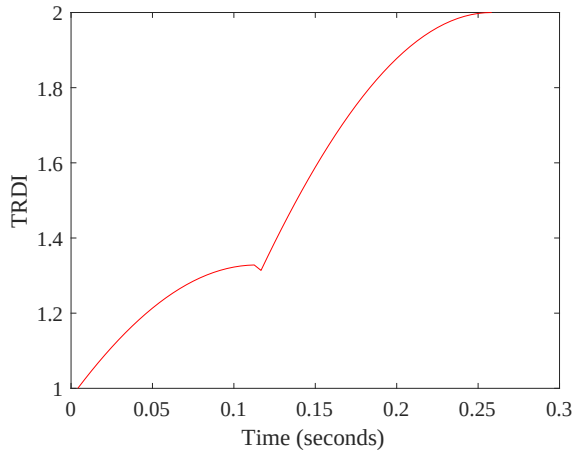

FIG. 5.15 TRDI vs. Time in negative direction of deformation

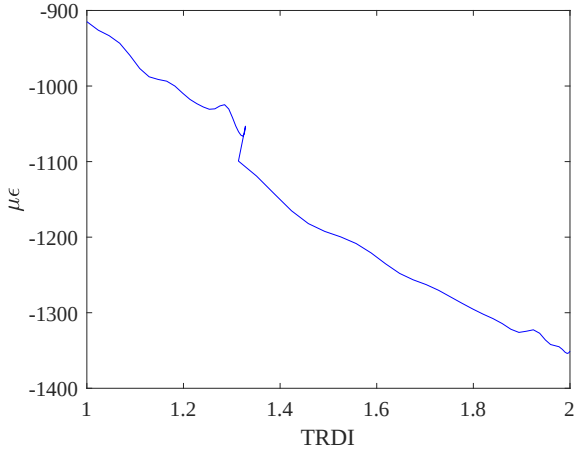

FIG. 5.16 Strain vs. TRDI in negative direction of deformation

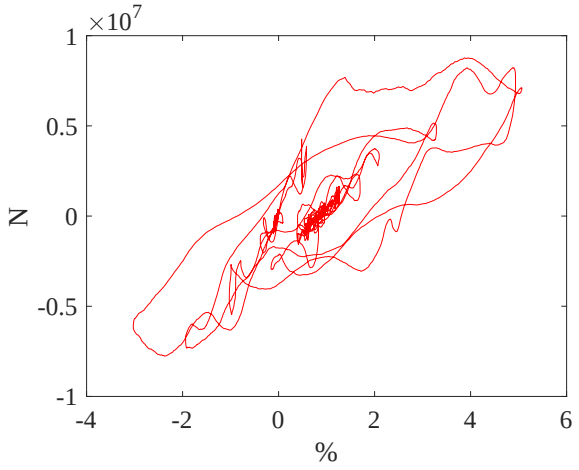

FIG. 5.17 Experimental force-deformation curve for EQ3

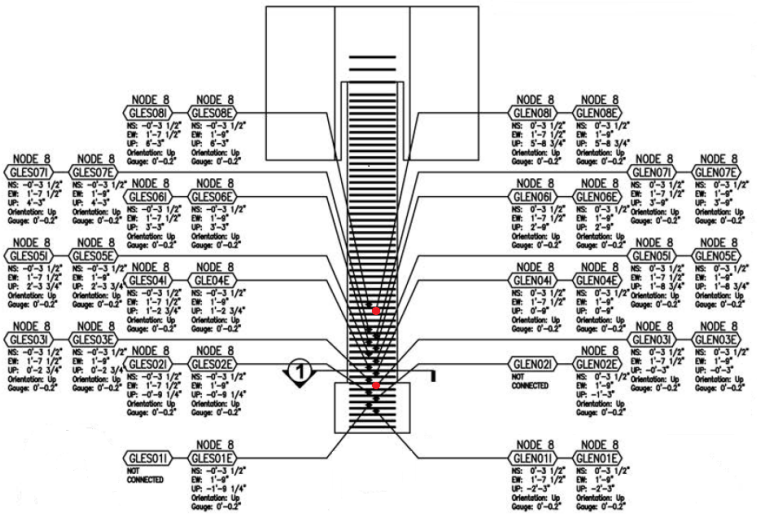

FIG. 5.18 Location of strain-gauges for calculation of correlation factor

5.1.3 Calculating the correlation coefficient between strain measurements

The correlation coefficient was calculated for the base excitations up to EQ4. Correlation was calculated between a pair of strain gauges (GLENO3I and GLENO8I)- Figure 5.18, Annex C. GLENO3I is below the base of the column and the expected location of the plastic hinge and GLENO8I is above the base and the expected location of the plastic hinge.

The change of the correlation factor is calculated in time by implementing a moving window on the data with a size of 500 and overlap of 499. Choosing the size of the window is of key importance for obtaining meaningful results. If the window is too small the data might be dominated by spurious transient response and indicate a non-linear relation between the strain even if the column has remained linear. On the other hand a

window which is too large will not capture the change in the correlation factor in time, which means loss of additional information. In this section the length of the window in time is in the order of the length of one deformation cycle of the column's response.

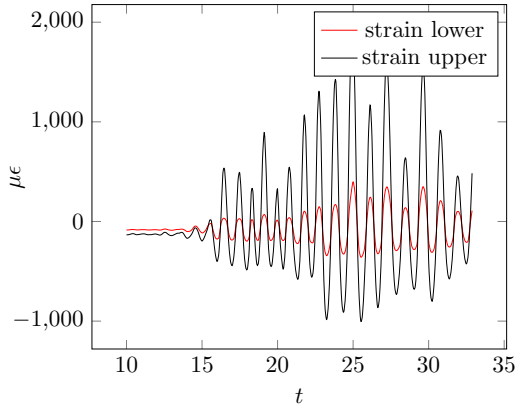

FIG. 5.19 Strain vs. time for lower and upper strain gauges, Trial 3

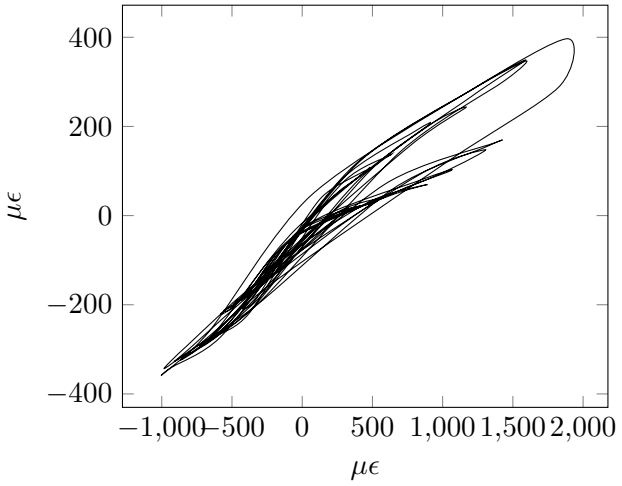

FIG. 5.20 Strain above vs. strain below plastic hinge for the entire record, Trial 3

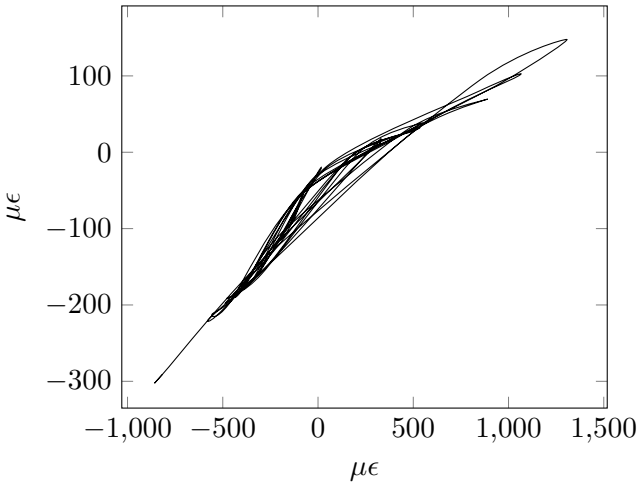

FIG. 5.21 Strain above vs. strain below plastic hinge before first HFT's, Trial 3

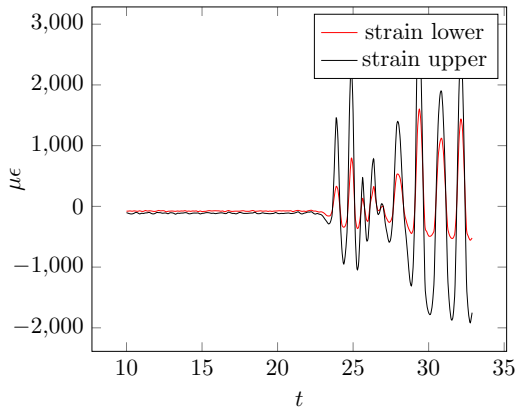

FIG. 5.22 Strain vs. time for lower and upper strain gauges, Trial 5

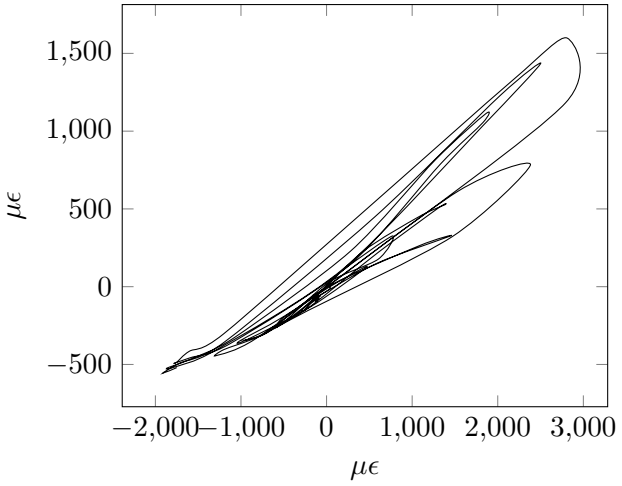

FIG. 5.23 Strain above vs. strain below plastic hinge the entire, Trial 5

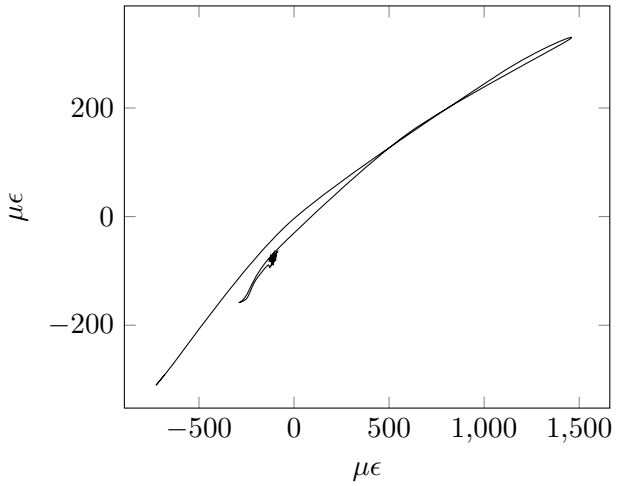

FIG. 5.24 Strain above vs. strain below plastic hinge first HFT's, Trial 5

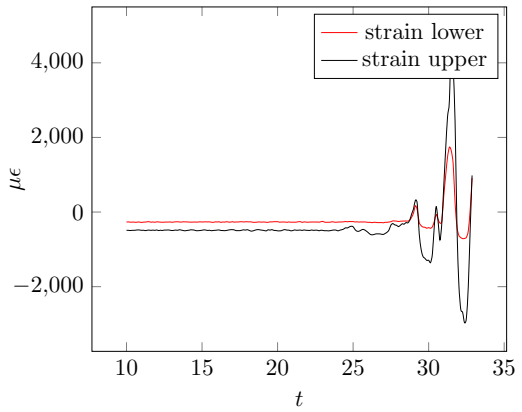

FIG. 5.25 Strain vs. time for lower and upper strain gauges, Trial 7

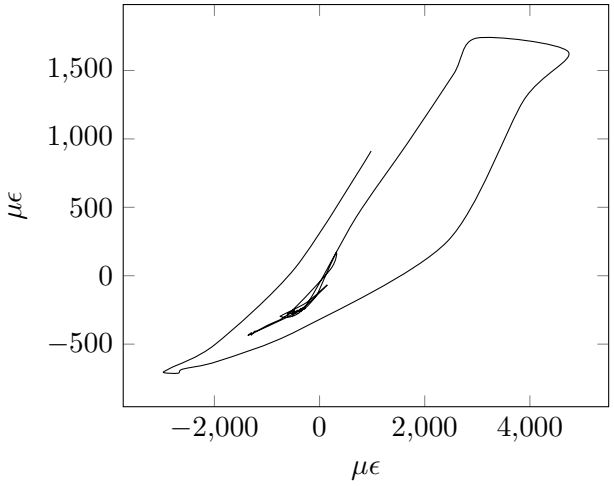

FIG. 5.26 Strain above vs. strain below plastic hinge for the entire record, Trial 7

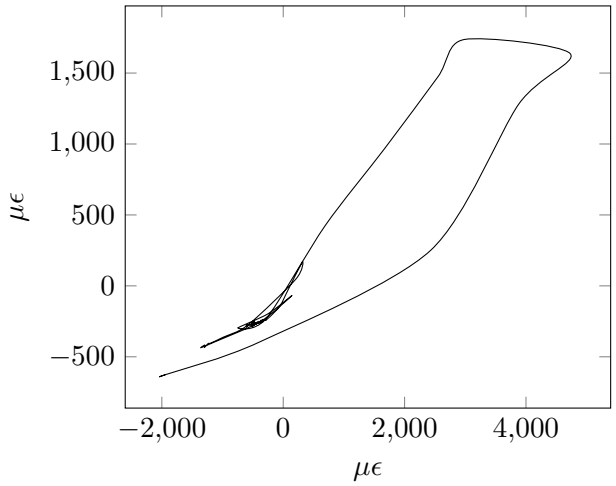

FIG. 5.27 Strain above vs. strain below plastic hinge before first HFT's, Trial 7

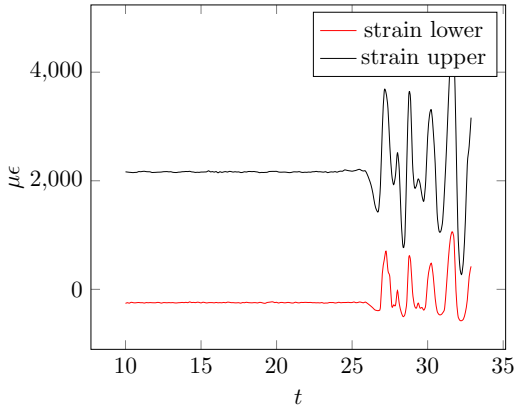

FIG. 5.28 Strain vs. time for lower and upper strain gauges, Trial 9

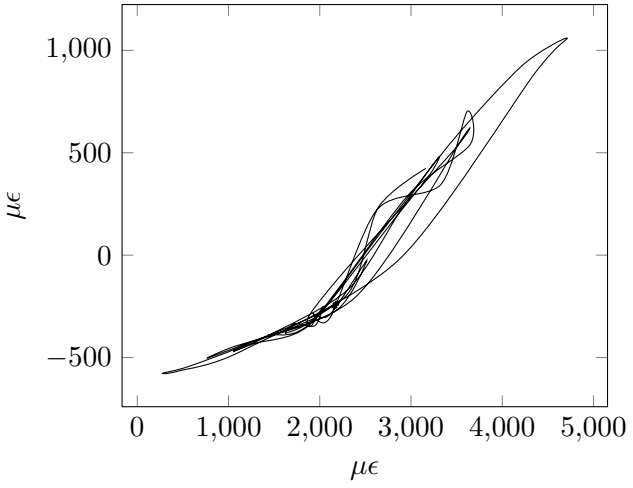

FIG. 5.29 Strain above vs. strain below plastic hinge for the entire record, Trial 9

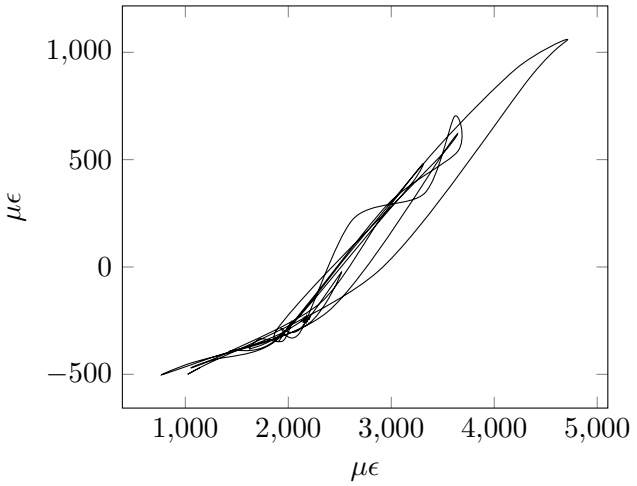

FIG. 5.30 Strain above vs. strain below plastic hinge before first HFT's, Trial 9

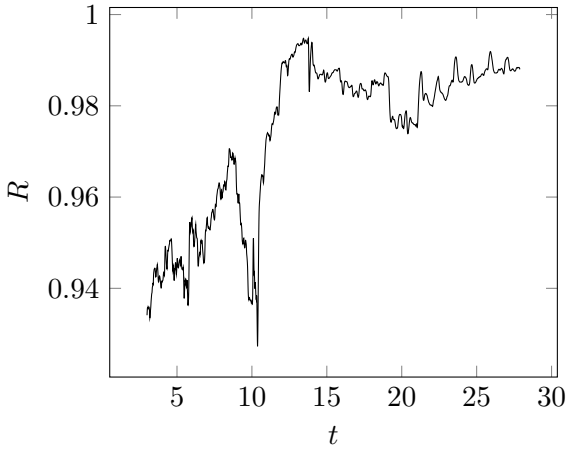

FIG. 5.31 Correlation factor vs. time for Trial 3, U.C. San Diego

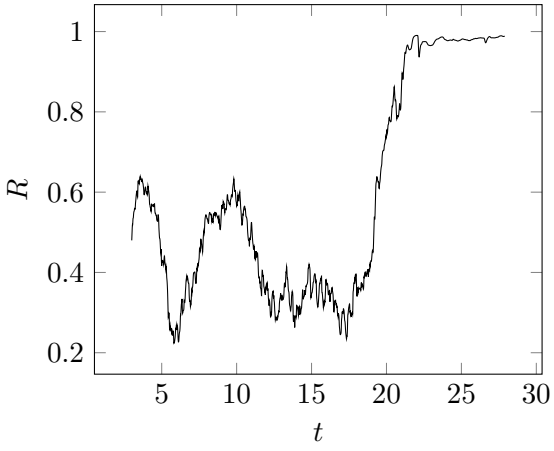

FIG. 5.32 Correlation factor vs. time for Trial 5, U.C. San Diego

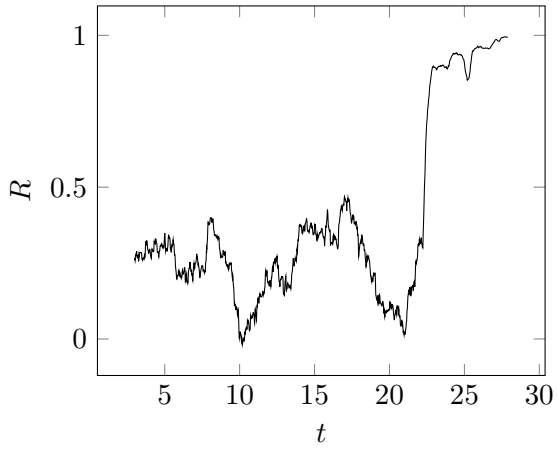

FIG. 5.33 Correlation factor vs. time for Trial 7, U.C. San Diego

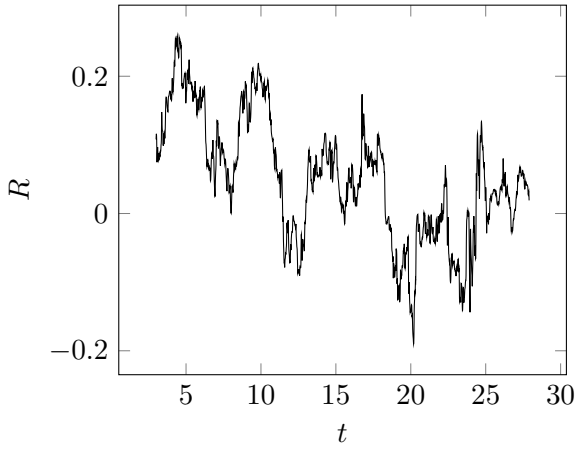

FIG. 5.34 Correlation factor vs. time for Trial 9, U.C. San Diego

5.1.4 Damage observed on the column after each EQ

Figure 5.35 and Table 4.1 summarize the damage observed on the column after each EQ.

5.1.5 Discussion of results for the UC. San Diego column

For the case study above, if it is assumed that the column has reached the I.O. performance level at $TRDI_y$, it could be concluded that the structure is in the Limited Safety performance range [11]. This follows from the multiplication of the drift at I.O., given in Table 2-4 in [11], by $\mu_N = 3.65$. In case of a real structure this conclusion is sufficient for the decision-making process regarding the future operation of the structure. It is also important to reiterate on how the yielding limit was found. This is done by exploiting the property of linear proportionality between different response quantities in linear systems.

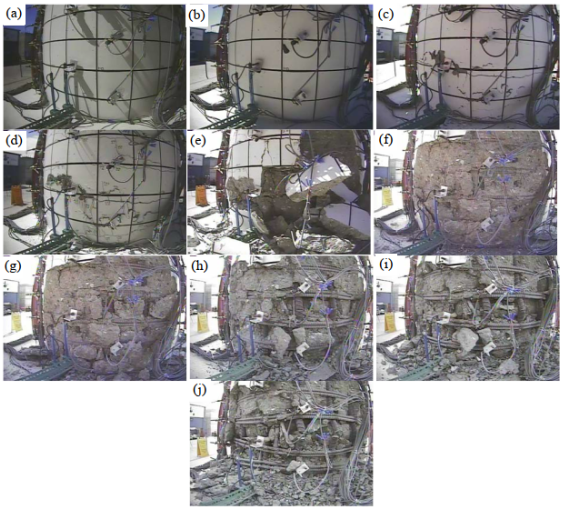

FIG. 5.35 Column base East face post test a)EQ1 b)EQ2 c)EQ3 d)EQ4 e)EQ5 f)EQ6 g)EQ7 h)EQ8 i)EQ9 j)EQ10

Once the linear proportionality is broken the system has become non-linear, which for structural elements means yielding. In the above case-study the tracked responses are strain and "drift", but the drift is represented by the $TRDI$. This allowed by the formulation of the $TRDI$, which relates it to the estimated drift by the constant Θ' (equation 2.3 and 2.4).

Here it is also important to discuss the suspected source of the HFT's. A key observation is that HFT's are detected only in the accelerometer data and not in the strain gauge data. Since accelerometers are able to capture rigid body response and strain gauges are not, it could be stipulated that the HFT's are related to a rigid body response. Additionally, the sampling rate of data is 240 Hz, therefore elastic waves generated directly from concrete cracking or reinforcement damage could not be detected. In such case the only damage mechanism left, which is also reported to cause a rigid body response in the form of end-rotation, is bond-slip between concrete and reinforcement [83]. From examinations of the measured strain in the reinforcement along the height of the reinforcement it is clear that there are losses of bond. This is concluded from the high amplitudes of the measured strain in the reinforcement, which the concrete is not able to resist, and the non-linear distribution of strain along the height of the reinforcement bars (Figure 5.38). The bond-slip causes a partial rigid body rotation of the column about the location of damage.

The assumptions laid out in Section 2.1 are confirmed as reasonable from the comparison with the directly measured drift. Drift was measured in the experiment with a spring potentiometer attached between the column and a rigid structure mounted on the

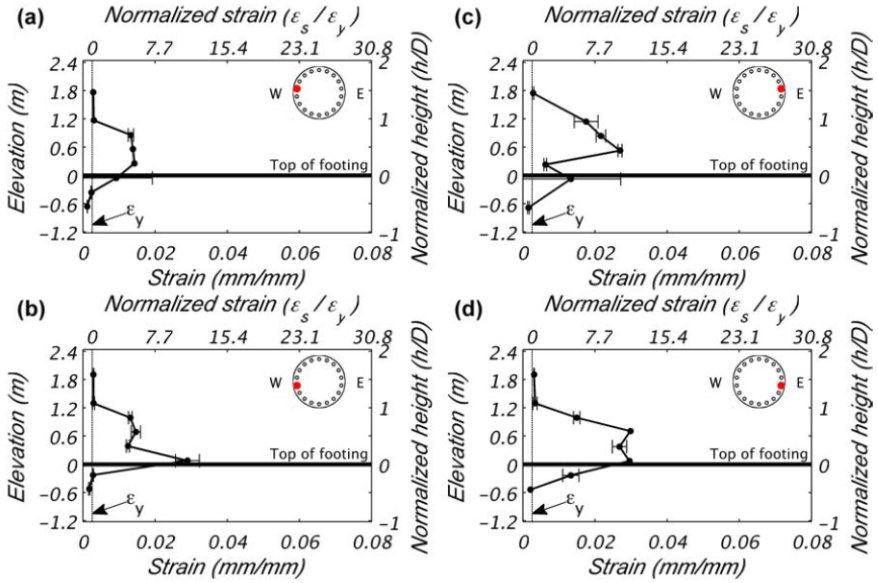

FIG. 5.36 Strain distribution along the height of reinforcement bars for EQ3 [5]

shaking table. Assumption 1) is as expected kept, since we basically have a single degree of freedom system. Assumptions 2) to 4) are justified by the fact that the HFT's arrive once the previous largest drift is exceed. Assumption 5) is justified by the fact that the maximum drifts were predicted with reasonable accuracy (Figure 5.10). Actually assumption 4) is analogous to Kaiser's effect. Kaiser's effect [84], [37], [85], [86], [87], [88], [89] is observed in classical acoustic emission where the sampling rate is in the order of kHz. Kaiser discovered that no signals (AE's) were generated by a sample upon the second loading until the previous maximum load was exceeded. To make the analogy with the method in this paper we have to consider the drift (or relative deformation) as the loading and the HFT's as the signals. Kaiser's effect does not always hold especially for composite materials. The reason for this is that after reapplication of the load the specimen is not always taken along the same micro-stress path [37]. The ratio between the the load at which the AE is observed to previous maximum load is known as the Felicity ratio. Figure 5.37 schematically demonstrates the Kaiser's effect and Felicity's ratio - as damage accumulates the arrival of AE is not exactly after the previous maximum load is reached (Kaiser's effect), but before this load is reached (Felicity's ratio < 1). Additional research is required to better understand the application of Kaiser's effect and Felicity's ratio within the frequency range associated with HFT's.

From Figure 5.31 to Figure 5.34 it is clearly observed that the correlation factor (R) tends to decrease as damage accumulates. Generally the correlation drops in value

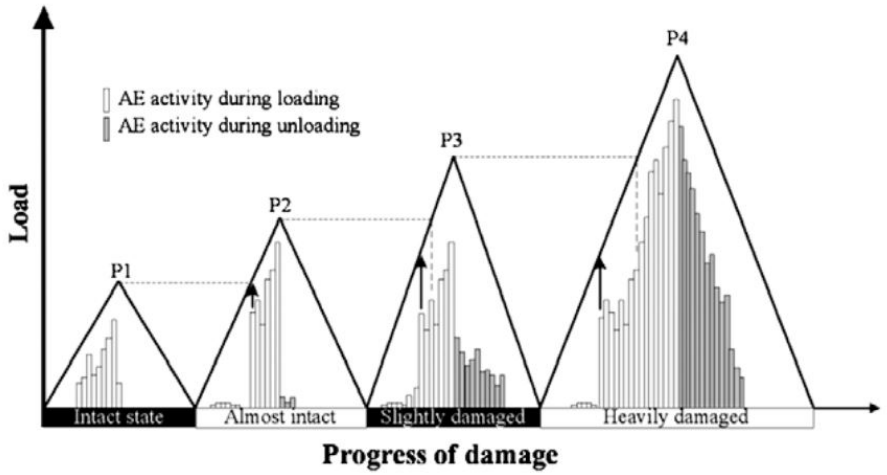

FIG. 5.37 AE activity with damage progress [90]

during stiffness reduction. Afterwards an increase could be observed, as the system becomes again linear, but with a different stiffness. When significant damage is present an increase in (R) might not occur, which implies a complete loss of linear proportionality between the strain measurements. In certain cases of excessive damage even negative correlation could be observed.

5.2 Limitations of the Proposed Method

A limitation is the requirement for a predominant first mode response of the structure. In case this requirement is not met the ductility factor deduced from the $TRDI$ will be inaccurate. This follows from the presumption of sinusoidal response within the half cycle as a basis for the deduction of the $TRDI$ (Section 2.1). The requirement for a predominant first mode response is what actually limits the method to bridge piers.

Further for the higher damage levels there is a vibration energy shift from to lower to higher modes ([25], [29]), thus contradicting the requirement for a predominant first mode response and introducing inaccuracies. This actually should not be of great concern, because such significant damage in a bridge pier is obvious and therefore the value if information of the output from the SHM lessens.

5.3 Results from University of Patras experiment

5.3.1 Observation of High-Frequency Transients

During the experimental work some of the instruments got damaged and others did produce more noise than expected. This made the data somewhat hard to interpret, therefore unfit for supporting general conclusions on the current research. Nevertheless the HFT's are again observed and their arrival is, as expected, shortly before the deformation extrema. The $TRDI$ was not calculated because of the above reasons. Results seemed to be highly dependent on the choice of the cut-off frequencies for the filter, which would make any conclusions strongly subjective. Therefore this section is limited to discussing observations in the data, which are of relevance to Section 5.1.1.

The first observation is that the HFT's again occur. This is observed for both columns. In all cases they occur right before a deformation extrema. Such a response was both observed and hypothesized in the previous chapters and sections.

The second observation is that the HFT's are not distinguishable once the column has accumulated a more significant amount of damage. This is caused by the increased response of the column in the higher modes, which masks the presence of the HFT's. Such an increase of response in the higher modes is expected, since as established in [29] and [25] the vibration energy shifts from lower to higher modes as damage accumulates.

The third observation is that the HFT's seem to occur once the previous maximum drift is exceed. This can not decisively concluded due to the subjectivity in choosing the cut-off frequency of the filter. This was not the case in 5.1.1 and therefore the issue might be limited to the specific data.

Results are plotted for accelerometer A4, strain gauge 2L and strain gauge 6L. Strain gauge 2L is below the expected location of the plastic hinge and strain gauge 6L is above. For a more detailed description of the instrumentation set-up please refer to Annex D.

Below we plot filtered strain and acceleration

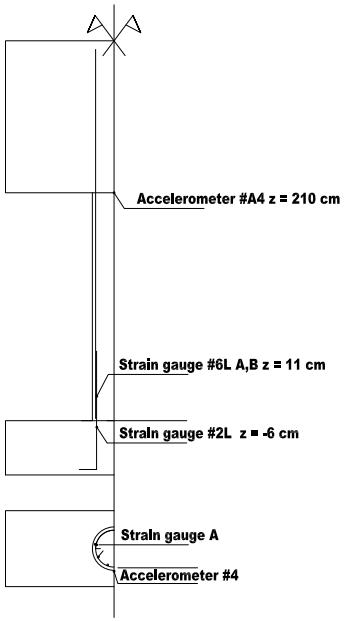

FIG. 5.38 Location of instrumentation for the given results

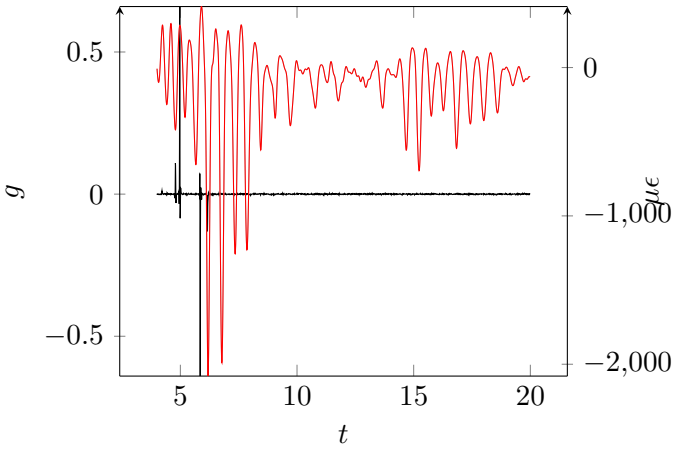

FIG. 5.39 Filtered acceleration and strain, 40 cm column, 50% excitation

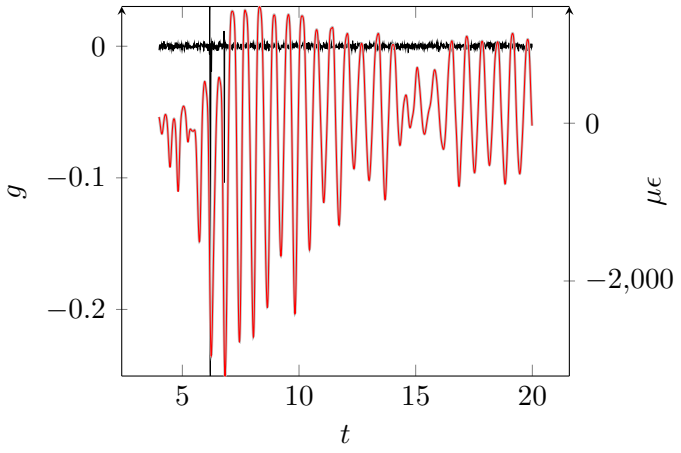

FIG. 5.40 Filtered acceleration and strain, 40 cm column, 75% excitation

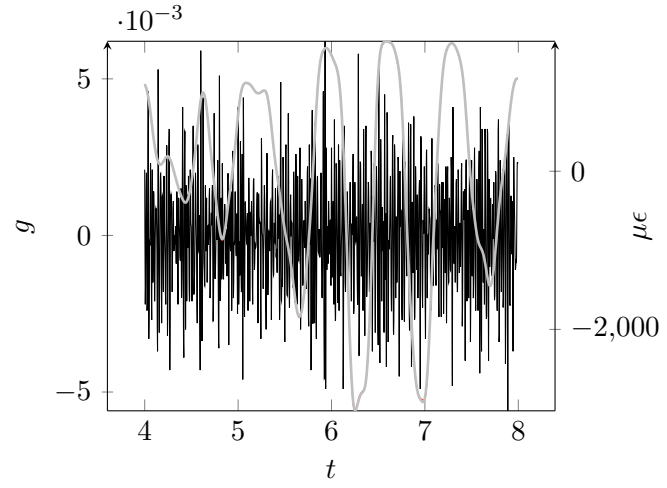

FIG. 5.41 Filtered acceleration and strain, 40 cm column, 100% excitation

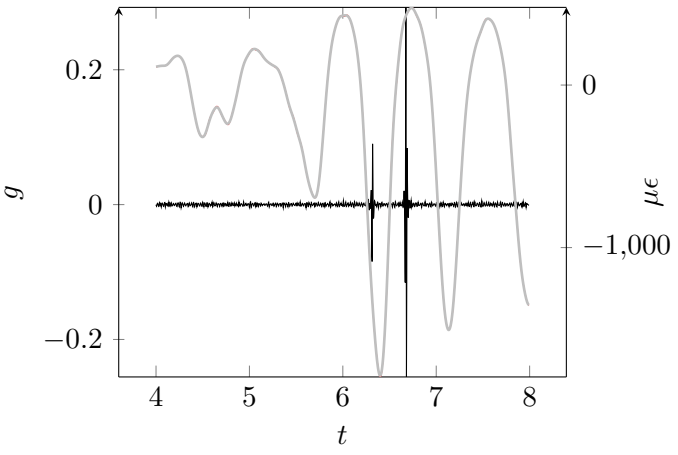

FIG. 5.42 Filtered acceleration and strain, 30 cm column, 50% excitation

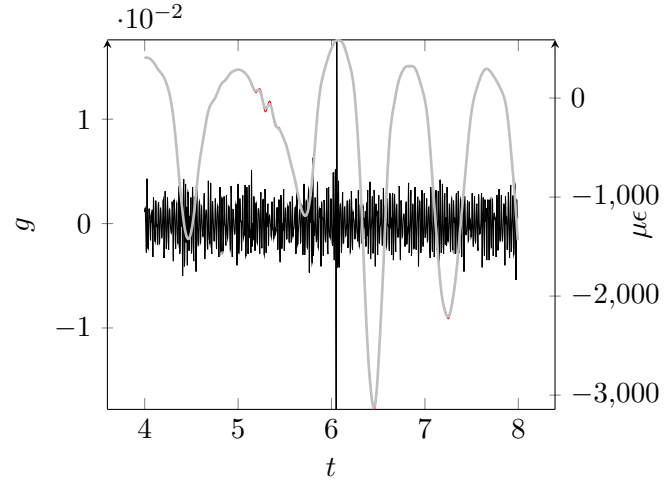

FIG. 5.43 Filtered acceleration and strain, 30 cm column, 100% excitation

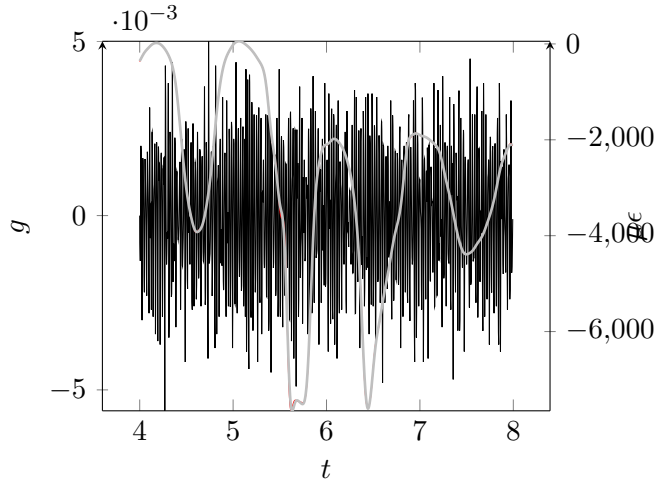

FIG. 5.44 Filtered acceleration and strain, 30 cm column, 100% excitation

Below we plot filtered drift and acceleration

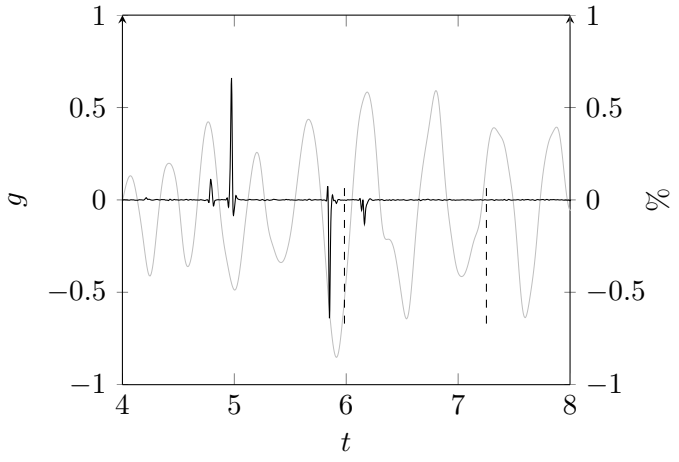

FIG. 5.45 Filtered acceleration and drift, 40 cm column, 50% excitation

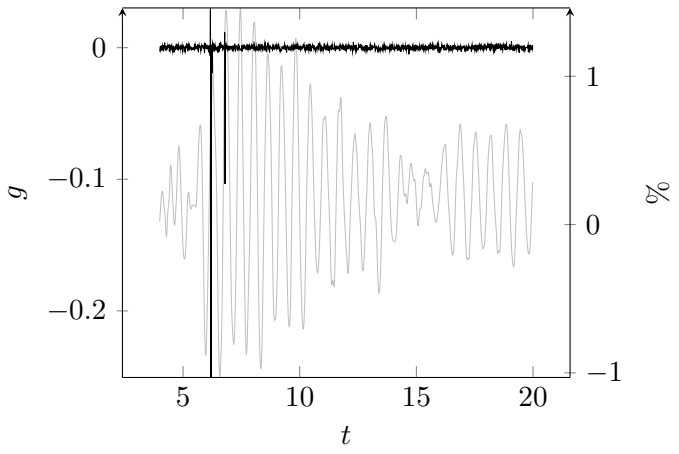

Fig. 5.46 Filtered acceleration and drift, 40 cm column, 75% excitation

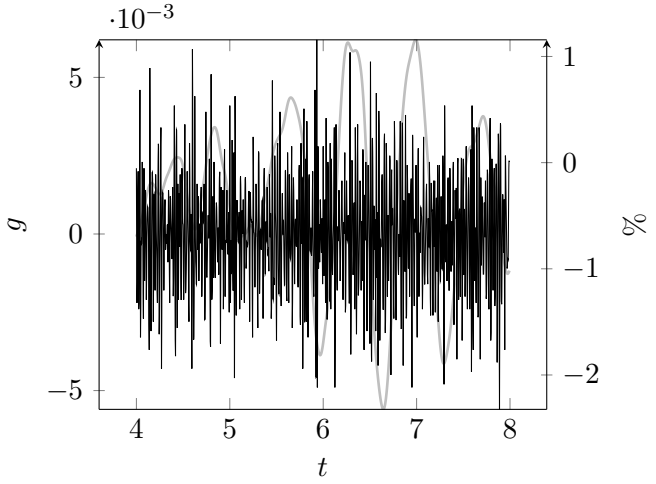

Fig. 5.47 Filtered acceleration and drift, 40 cm column, 100% excitation

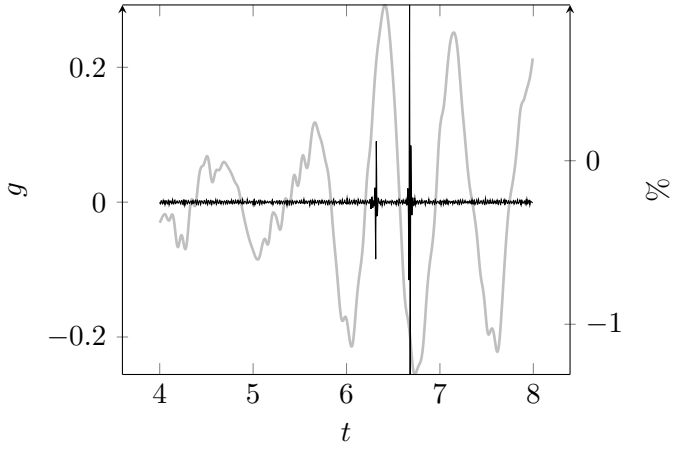

Fig. 5.48 Filtered acceleration and drift, 30 cm column, 50% excitation

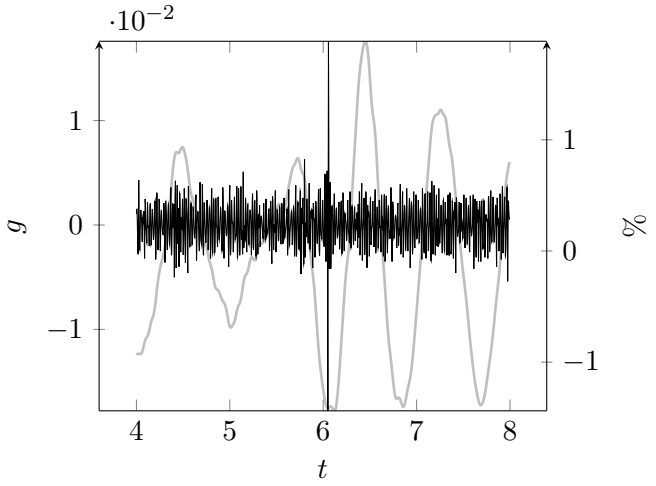

FIG. 5.49 Filtered acceleration and drift, 30 cm column, 75% excitation

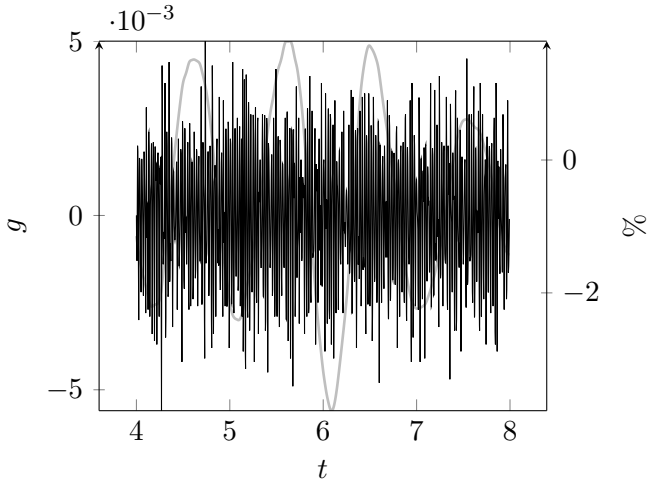

FIG. 5.50 Filtered acceleration and drift, 30 cm column, 100% excitation

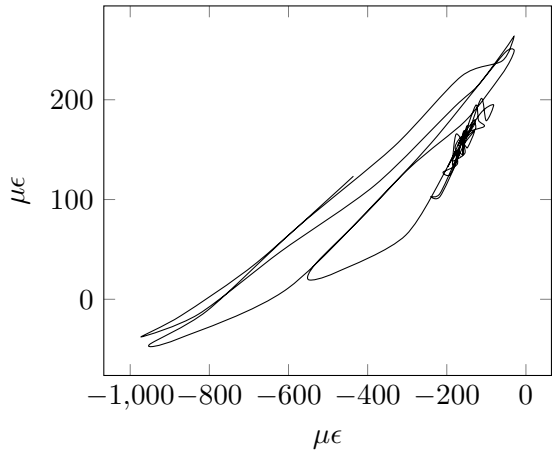

FIG. 5.51 Strain above vs. strain below plastic hinge for the entire record, 30 cm column, 25 % excitation

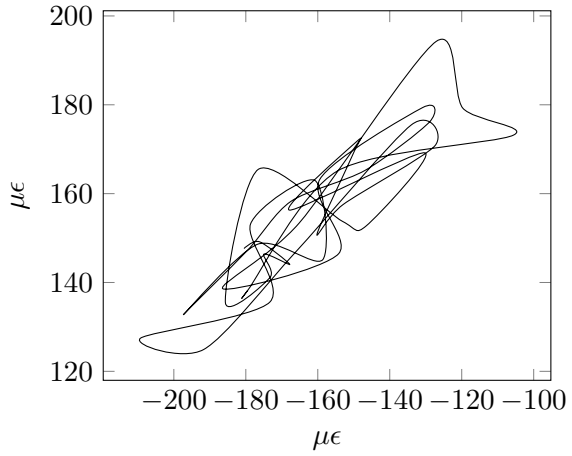

FIG. 5.52 Strain above vs. strain below plastic hinge before first HFT, 30 cm column, 25 % excitation

5.3.2 Strain measurements below and above the expected plastic hinge location

Below we plot filtered strains below and above the plastic hinge. The purpose of this is to show clearly the relation between the strain measured below and above the expected location of the plastic hinge.

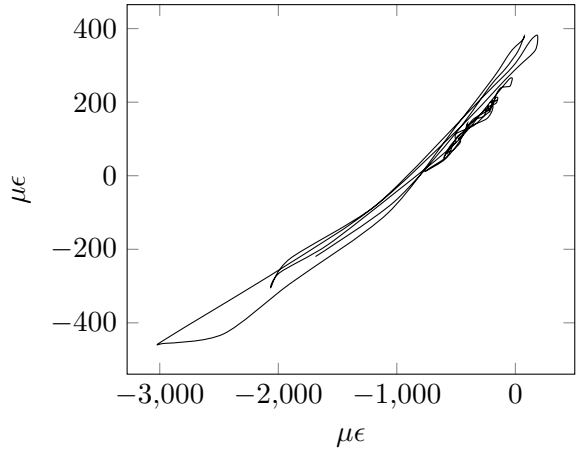

FIG. 5.53 Strain above vs. strain below plastic hinge for the entire record, 30 cm column, 50 % excitation

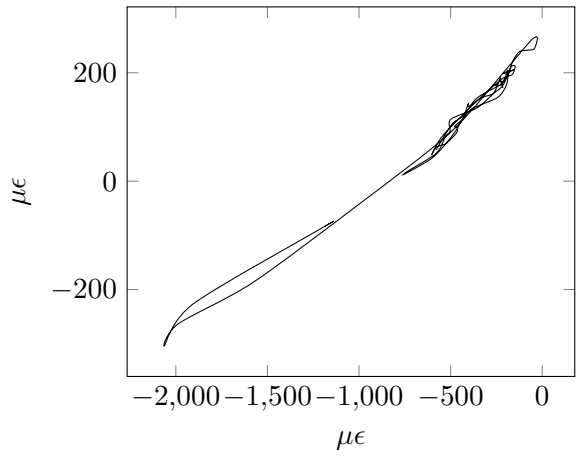

FIG. 5.54 Strain above vs. strain below plastic hinge before first HFT, 30 cm column, 50 % excitation

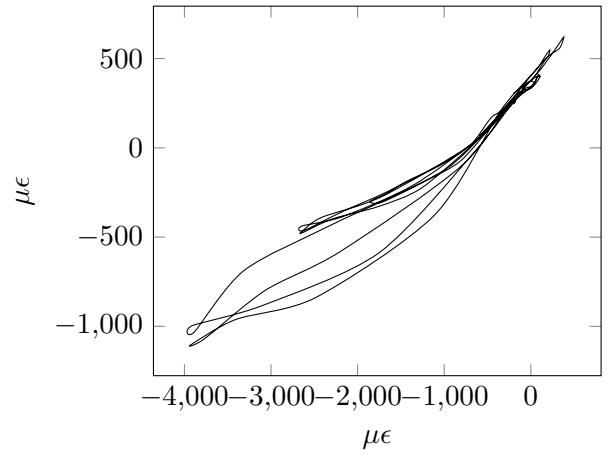

FIG. 5.55 Strain above vs. strain below plastic hinge for the entire record, 30 cm column, 75 % excitation

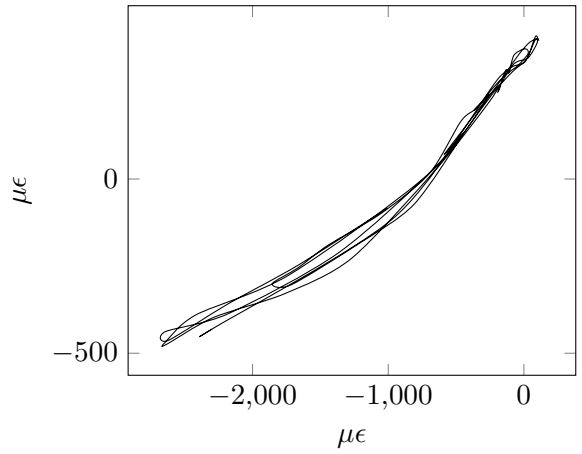

FIG. 5.56 Strain above vs. strain below plastic hinge for the entire record, 30 cm column, 75 % excitation

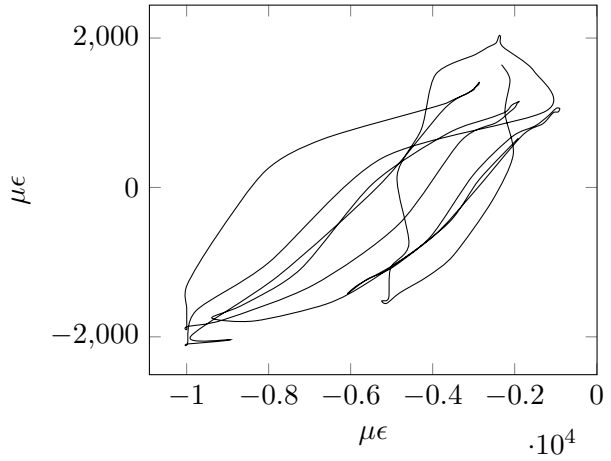

FIG. 5.57 Strain above vs. strain below plastic hinge for the entire record, 30 cm column, 100 % excitation

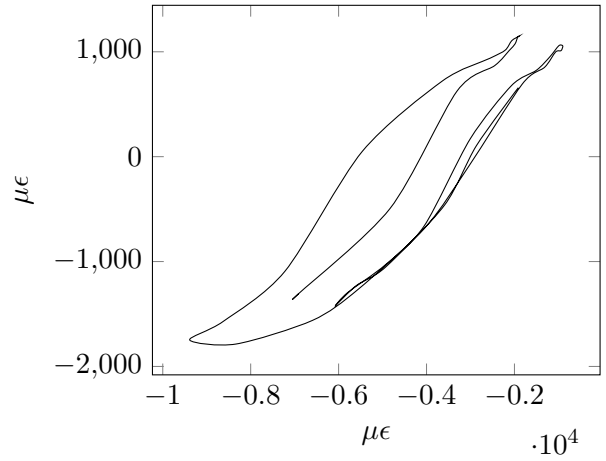

FIG. 5.58 Strain above vs. strain below plastic hinge before first HFT, 30 cm column, 100 % excitation

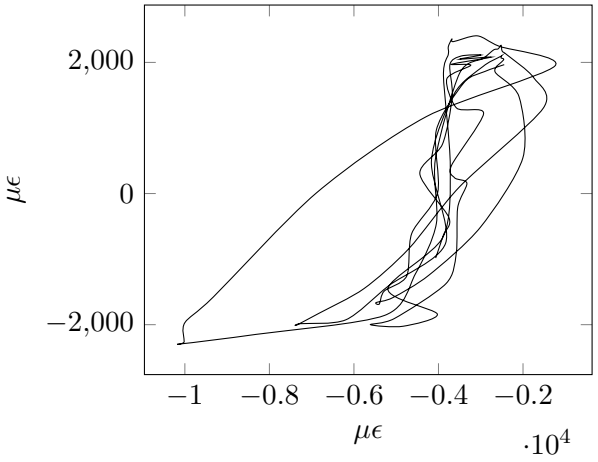

FIG. 5.59 Strain above vs. strain below plastic hinge for the entire record, 30 cm column, 120 % excitation

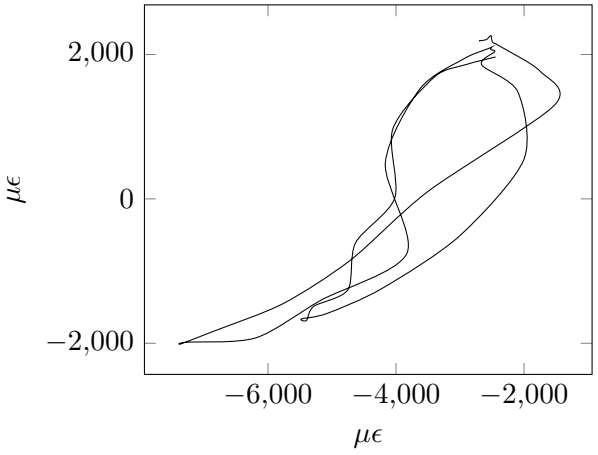

FIG. 5.60 Strain above vs. strain below plastic hinge before first HFT, 30 cm column, 120 % excitation

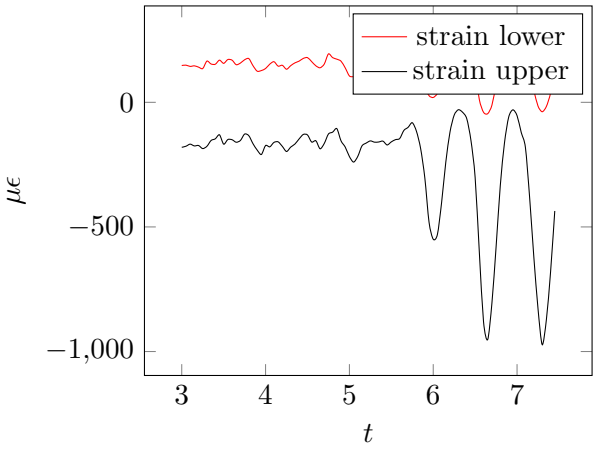

FIG. 5.61 Strain vs. time for lower and upper strain gauges, 30 cm column, 25 % excitation

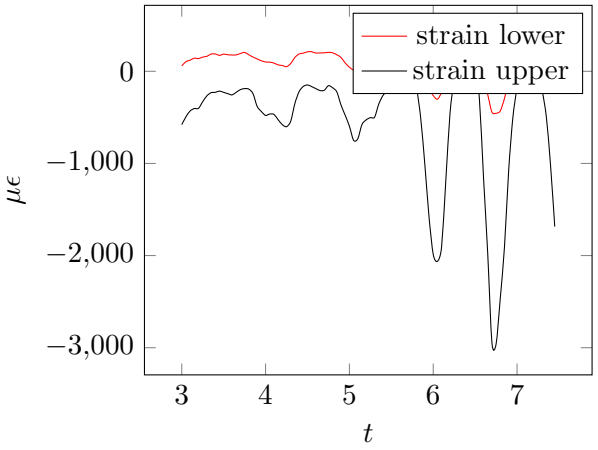

FIG. 5.62 Strain vs. time for lower and upper strain gauges, 30 cm column, 50 % excitation

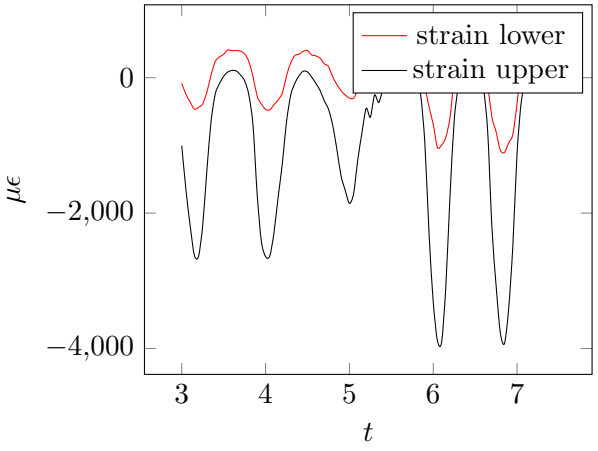

FIG. 5.63 Strain vs. time for lower and upper strain gauges, 30 cm column, 75 % excitation

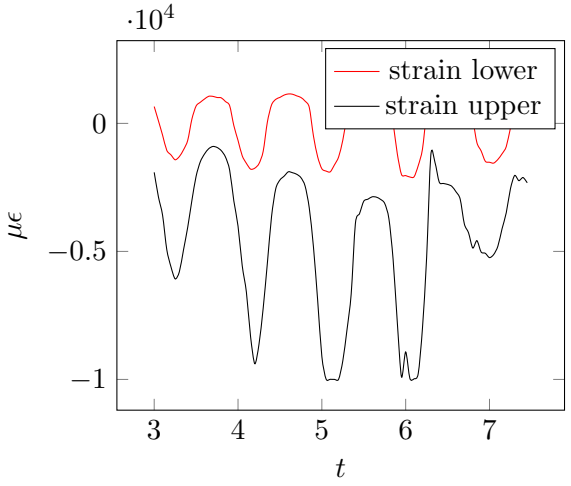

FIG. 5.64 Strain vs. time for lower and upper strain gauges, 30 cm column, 100 % excitation

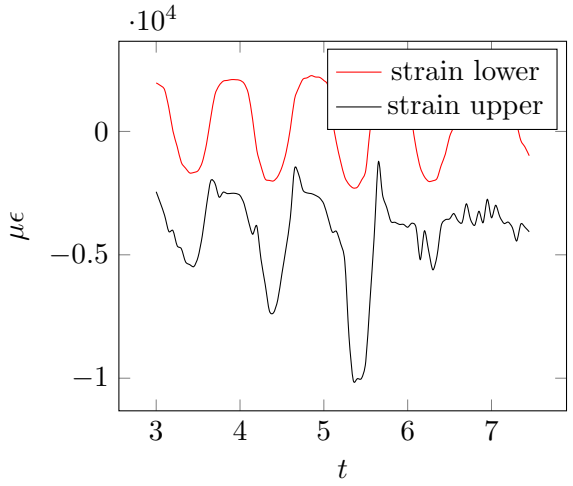

FIG. 5.65 Strain vs. time for lower and upper strain gauges, 30 cm column, 120 % excitation

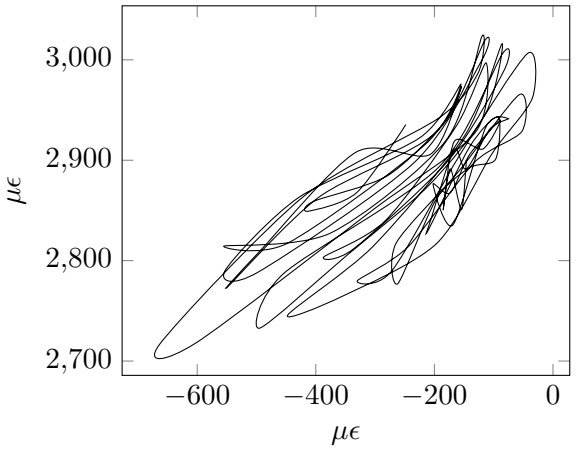

FIG. 5.66 Strain above vs. strain below plastic hinge for the entire record, 40 cm column, 25 % excitation

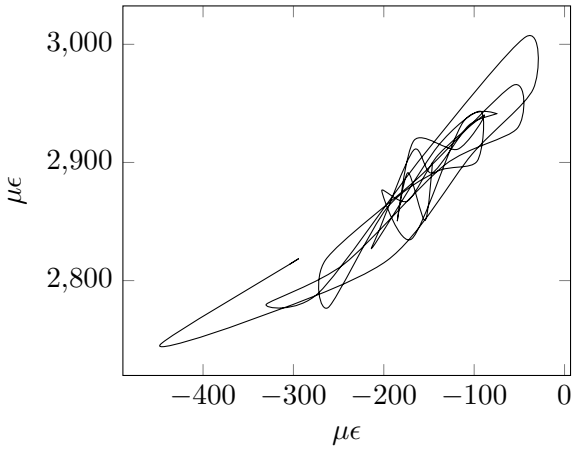

FIG. 5.67 Strain above vs. strain below plastic hinge before first HFT, 40 cm column, 25 % excitation

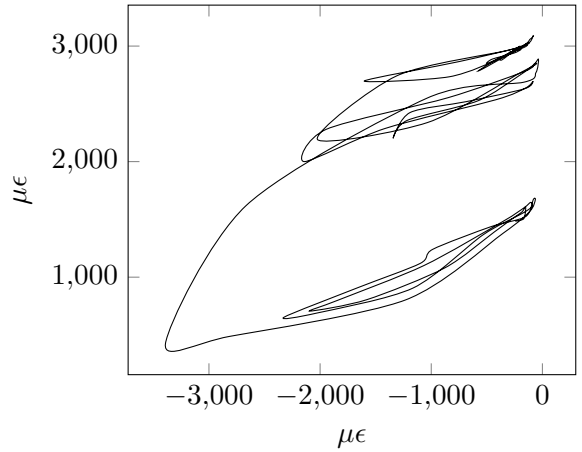

FIG. 5.68 Strain above vs. strain below plastic hinge for the entire record, 40 cm column, 50 % excitation

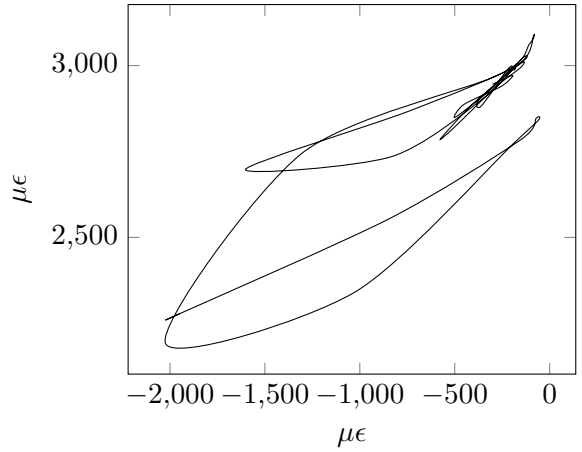

FIG. 5.69 Strain above vs. strain below plastic hinge before first HFT, 40 cm column, 50 % excitation

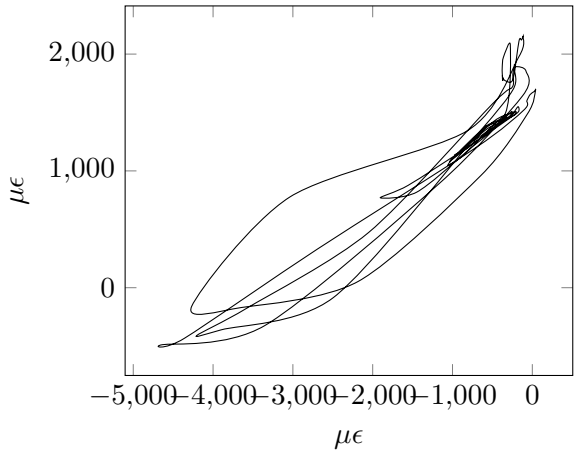

FIG. 5.70 Strain above vs. strain below plastic hinge ENTIRE RECORD ..., 40 cm column, 75 % excitation

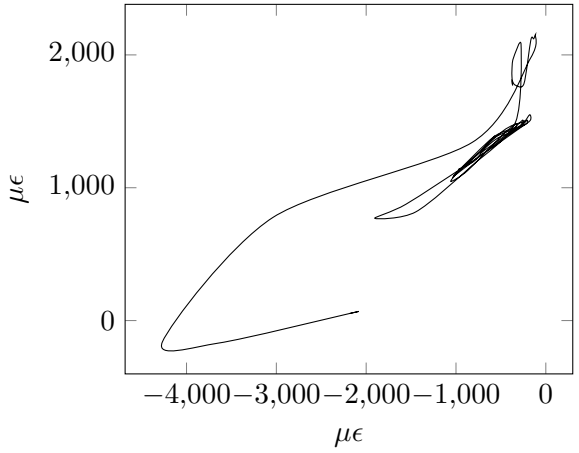

FIG. 5.71 Strain above vs. strain below plastic hinge before first HFT, 40 cm column, 75 % excitation

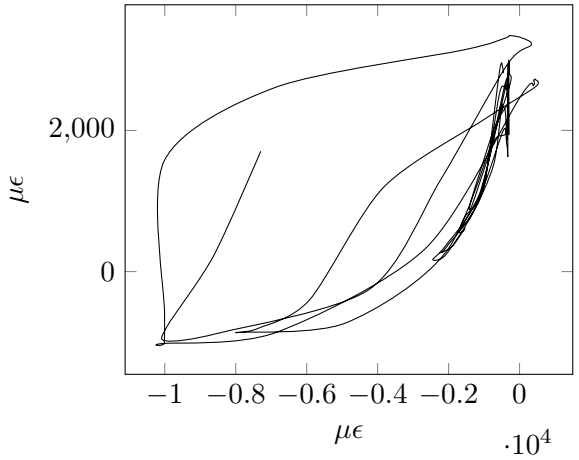

FIG. 5.72 Strain above vs. strain below plastic hinge for the entire record, 40 cm column, 100 % excitation

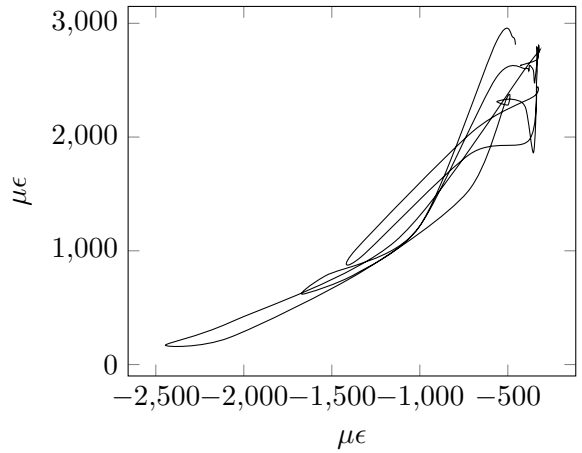

Fig. 5.73 Strain above vs. strain below plastic hinge before first HFT, 40 cm column, 100 % excitation

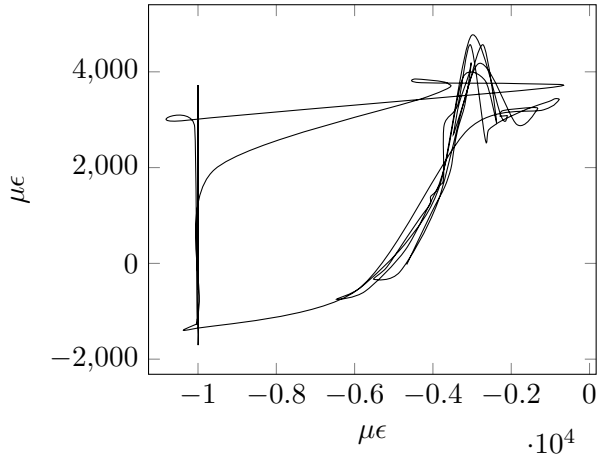

Fig. 5.74 Strain above vs. strain below plastic hinge for the entire record, 40 cm column, 120 % excitation

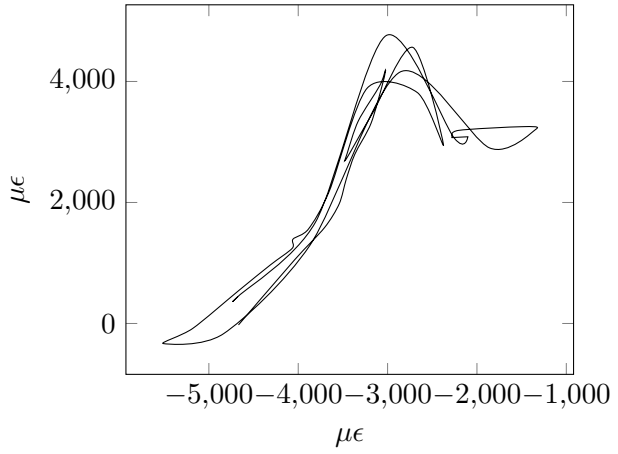

Fig. 5.75 Strain above vs. strain below plastic hinge before first HFT, 40 cm column, 120 % excitation

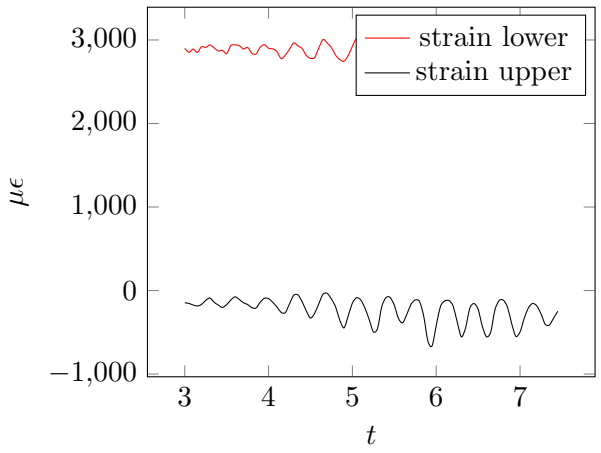

FIG. 5.76 Strain vs. time for lower and upper strain gauges, 40 cm column, 25 % excitation

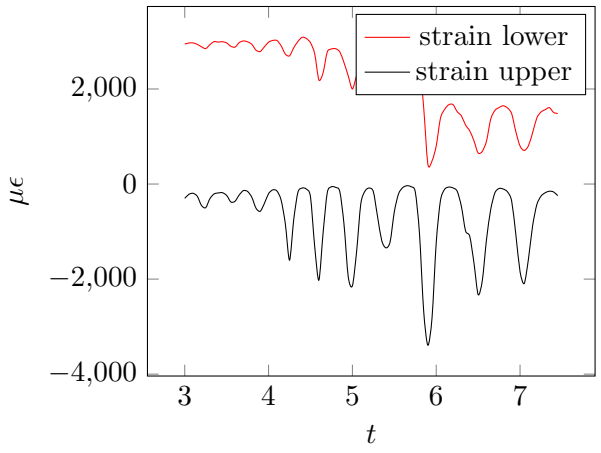

FIG. 5.77 Strain vs. time for lower and upper strain gauges, 40 cm column, 50 % excitation

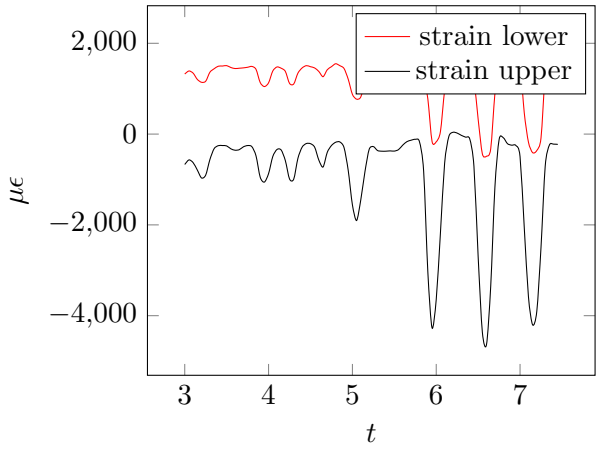

FIG. 5.78 Strain vs. time for lower and upper strain gauges, 40 cm column, 75 % excitation

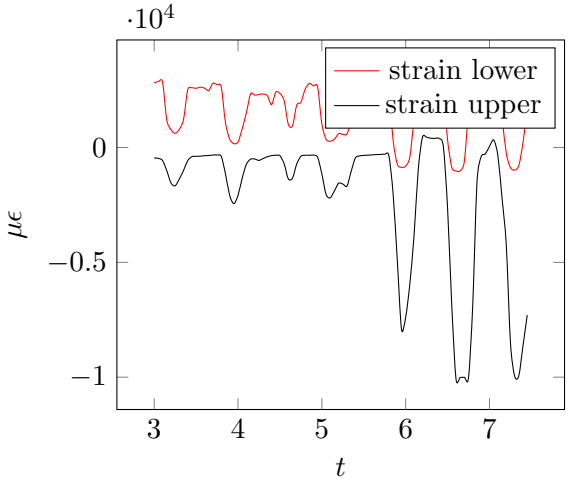

FIG. 5.79 Strain vs. time for lower and upper strain gauges, 40 cm column, 100 % excitation

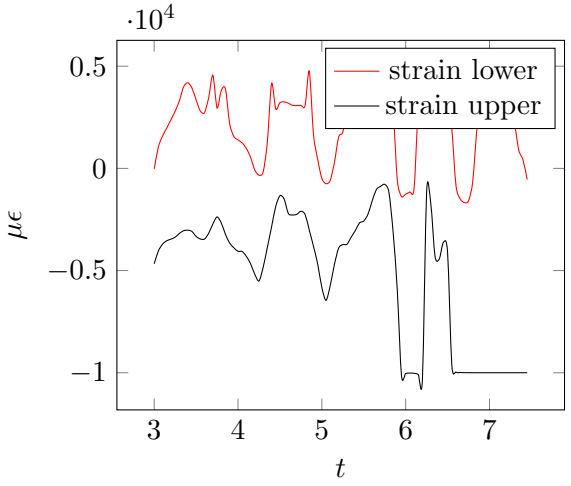

FIG. 5.80 Strain vs. time for lower and upper strain gauges, 40 cm column, 120 % excitation

5.3.3 Calculation of the correlation coefficient

In this section the correlation factor between strain measurements for each of the base excitations is calculated. A moving window with a size of 2000 and overlap of 1999 is chosen for extracting the data from the strain measurements above and below the plastic hinge. For each position of the window the correlation factor between the two extracted data sets is calculated. Measurements are taken from strain gauge 2L and 6L. (Annex D).

In Chapter 3 and Section 5.1.3 it was well observed that the correlation factor has a strong tendency of decreasing as damage accumulates. This was not strictly observed for the strain measurements from the experiments at the University of Patras. It is suspected that the main reason for this could be lower sensitivity of the instruments. The expected drop in the correlation factor can be more clearly observed once more cracks in the columns have occurred and the measured strains are more significant. A further discussion of the results is given in Chapter 6

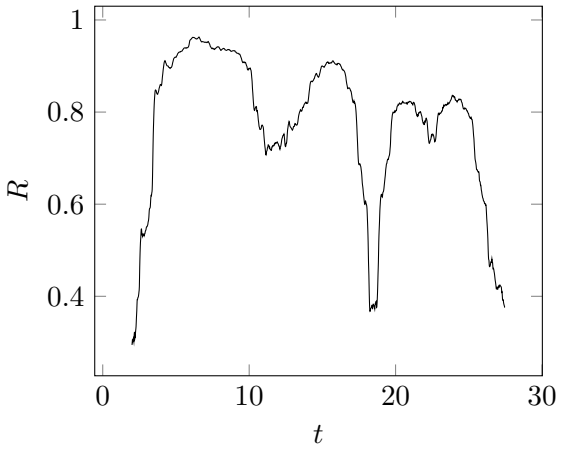

FIG. 5.81 Correlation factor vs. time for 30 cm column 25 % excitation

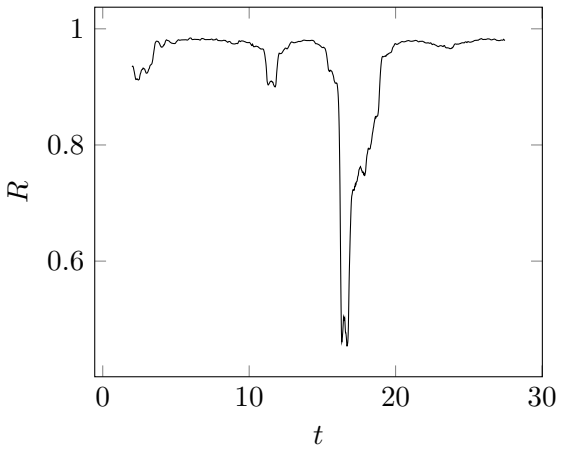

Fig. 5.82 Correlation factor vs. time for 30 cm column 50 % excitation

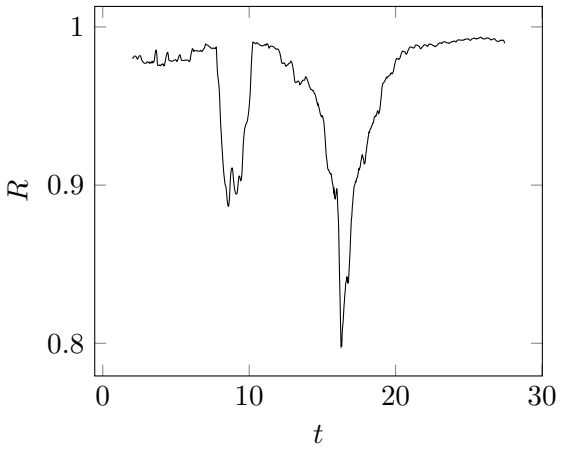

Fig. 5.83 Correlation factor vs. time for 30 cm column 75 % excitation

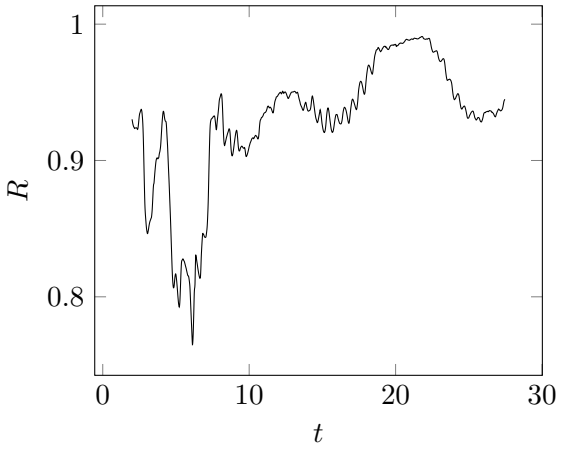

Fig. 5.84 Correlation factor vs. time for 30 cm column 100 % excitation

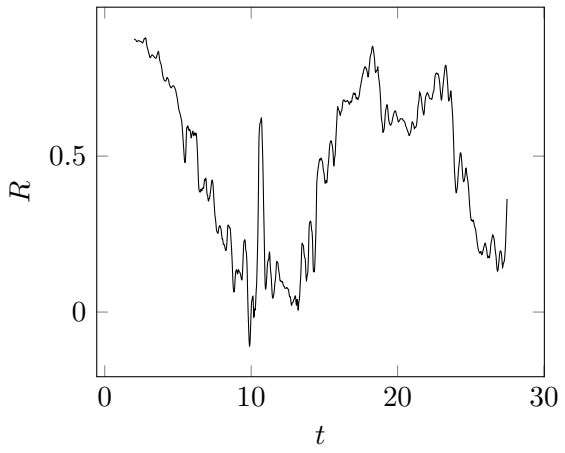

FIG. 5.85 Correlation factor vs. time for 30 cm column 120 % excitation

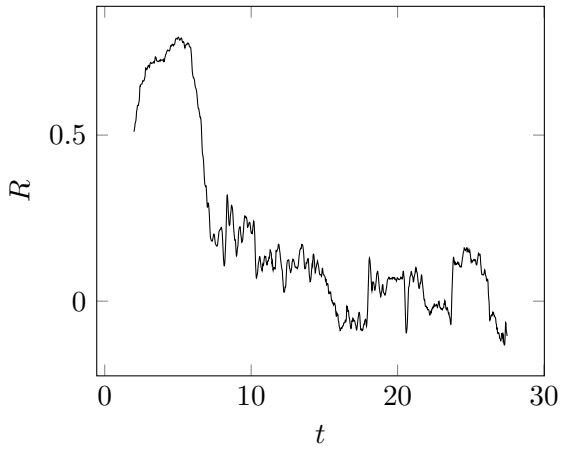

FIG. 5.86 Correlation factor vs. time for 40 cm column 25 % excitation

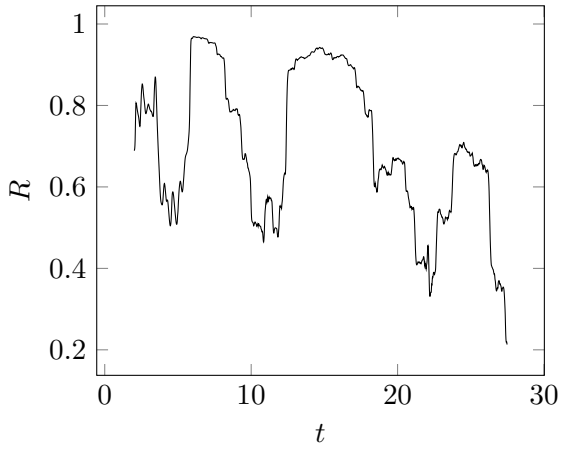

FIG. 5.87 Correlation factor vs. time for 40 cm column 50 % excitation

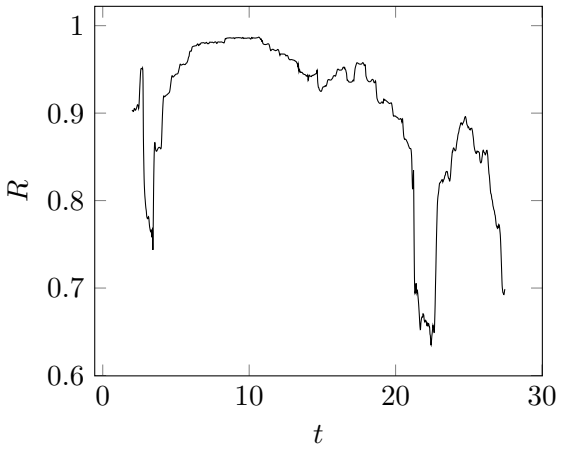

FIG. 5.88 Correlation factor vs. time for 40 cm column 75 % excitation

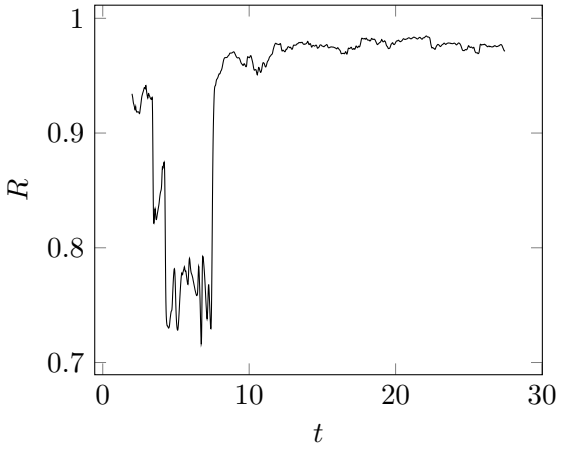

FIG. 5.89 Correlation factor vs. time for 40 cm column 100 % excitation

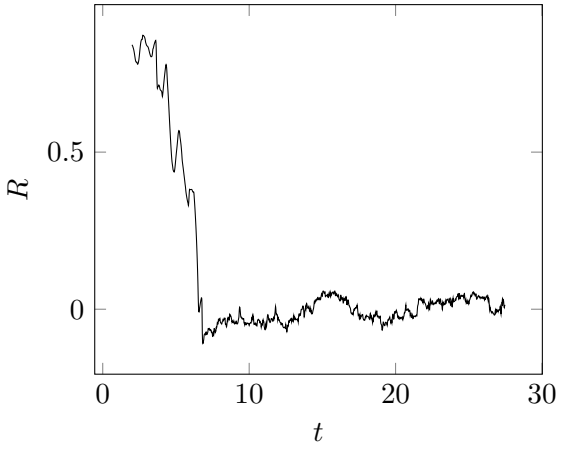

FIG. 5.90 Correlation factor vs. time for 40 cm column 120 % excitation

5.3.4 Damage observed on the columns after each EQ

FIG. 5.91 After test 30 cm column 120%

FIG. 5.92 After test 40 cm column 120%

FIG. 5.93 After test 40 cm column 120%

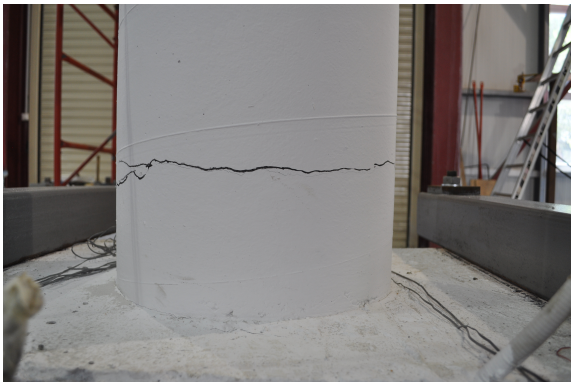

FIG. 5.94 After test 40 cm column 100%

Chapter 6

Discussion of Results

6.1 UC San Diego

For the case study above, if it is assumed that the column has reached the I.O. performance level at $TRDI_y$, it could be concluded that the structure is in the Limited Safety performance range [11]. This follows from the multiplication of the drift at I.O., given in Table 2-4 in [11], by $\mu_N = 3.65$. In case of a real structure this conclusion is sufficient for the decision-making process regarding the future operation of the structure. It is also important to reiterate on how the yielding limit was found. This is done by exploiting the property of linear proportionality between different response values in linear systems. Once the linear proportionality is broken the system has become non-linear, which for structural elements means yielding. In the above case-study the tracked responses are strain and "drift", but the drift is represented by the $TRDI$. This allowed by the formulation of the $TRDI$, which relates it to the estimated drift by the constant Θ' (equation 2.3 and 2.4).

Here it is also important to discuss the suspected source of the HFT's. A key observation is that HFT's are detected only in the accelerometer data and not in the strain gauge data. Since accelerometers are able to capture rigid body response and strain gauges are not, it could be stipulated that the HFT's are related to a rigid body response. Additionally, the sampling rate of data is 240 Hz, therefore elastic waves generated directly from concrete cracking or reinforcement damage could not be detected. In such case the only damage mechanism left, which is also reported to cause a rigid body response in the form of end rotation, is bond-slip between concrete and reinforcement [83]. From examinations of the measured strain in the reinforcement along the height

of the reinforcement it is clear that there are losses of bond. This is concluded from the high amplitudes of the measured strain in the reinforcement, which the concrete is not able to resist, and the non-linear distribution of strain along the height of the reinforcement bars. The bond-slip causes a partial rigid body rotation of the column about the location of damage.

The assumptions laid out in Section 2.1 are confirmed as reasonable from the comparison with the directly measured drift. Drift was measured in the experiment with a spring potentiometer attached between the column and a rigid structure mounted on the shaking table. Assumption 1) is as expected kept, since we basically have a single degree of freedom system. Assumptions 2) to 4) are justified by the fact that the HFT's arrive once the previous largest drift is exceed. Assumption 5) is justified by the fact that the maximum drifts were predicted with reasonable accuracy (Figure 5.10). Actually assumption 4) is analogous to Kaiser's effect [84], [37], [91]. Kaiser's effect is observed in classical acoustic emission where the sampling rate is in the order of kHz. Kaiser discovered that no signals (AE's) were generated by a sample upon the second loading until the previous maximum load was exceeded. To make the comparison with the method in this paper we have to consider the drift (or relative deformation) as the loading and the HFT's as the signals.

6.1.1 Limitations of the Proposed Procedure

A notable limitation is the requirement for a predominant first mode response of the structure. In case this requirement is not met the drift deduced from the $TRDI$ will be inaccurate. This follows from the presumption of sinusoidal response as a basis for the deduction of the $TRDI$ (Section 2.1). It is further not clear if the HFT's would be captured in all cases, which would lead to an underestimation of the damage. For the case study above most likely not all HFT's were captured in the "negative" side of deformation, or the arrival times were detected inaccurately. This is concluded from the fact that a drift of 1.76 % was reached, but the relationship between strain and the $TRDI$ remained linear. Further for the higher damage levels the vibration energy shifts from to lower to higher modes ([25], [29]), thus contradicting the requirement for a predominant first mode response and introducing inaccuracies.

6.2 University of Patras

The data obtained from the two shaking table tests did not fully confirm nor refute the hypotheses previously laid out, although that was not the case for the experiment at UCSD. A main conclusion from the experimental work at the University of Patras is that highly sensitive instrumentation is needed for the successful application of the above described methods for damage detection.

Nevertheless, the phenomenon of HFT's was again observed and the arrival of the HFT's was again shortly before the deformation extrema. The expected change of the correlation factor in time was observed only after more significant cracking of the concrete. The TRDI was not calculated due to subjectivity related to both selecting the strain gauge for the output data and selecting the cut-off frequency of the filters. It could be the case that the problems laid out are not specific to the current data. This implies the need for additional experimental work. One thing that could be concluded with a good amount of certainty is that HFT's are observed in all of the three experimental columns and they always arrive before the deformation extrema. The large number of HFT's observed for the three experiments supports this conclusion with statistical significance.

Another interesting, although somewhat expected observation, is the closing of the cracks after the end of the base excitation. This was the case for limited yielding of the reinforcement. Such damage might require retrofitting measures, but this will not be evident due to the seemingly undamaged appearance of the column. Damage was detected because the column was instrumented. This demonstrated the VoI from the SHM at levels of damage which are limited, but still require action.

Chapter 7

Summary and Conclusions

The current thesis proposed a procedure for the calculation of the ductility factor reached by a structure during earthquake response. This was achieved by comparing the strain in the reinforcement at an arbitrary location with a damage indicator called the $TRDI$. In essence the strain and the drift of the structure are compared, since the $TRDI$ is related to the drift by a constant. The ductility factor was calculated by dividing the maximum $TRDI$ by the $TRDI$ at yielding. The result is identical to dividing the maximum drift by the drift at yielding. Obtaining the $TRDI$ at yielding is performed by locating the loss of linear proportionality between the $TRDI$ and strain. This approach is justified by the fact that both the $TRDI$ and the strain are response quantities, which should remain linearly proportional in case the structure has not gone into the nonlinear range.

The $TRDI$ is a function of the arrival time of the HFT's, the time-instances of the deformation extrema and the time-length of the deformation half-cycles. By assuming a sinusoidal response within the deformation half cycle the $TRDI$ is directly related to the drift of the structure. A drawback of such an assumption is that the currently proposed damage estimation method is valid only for structures with a predominant first mode response. Such a response guarantees that the approximation with a sinusoidal function is sufficient within a deformation half-cycle.

It was further stipulated on the cause of the HFT's. Since the HFT's were detected only in the accelerometer data and not in the strain gauge data, it was hypothesized that the transients are related to a partial rigid body response. Such a response is observed during bond-slip failure. Considering the low sampling rate of the data (240 Hz), only transients related to bond-slip could be captured. Transients related to concrete cracking and reinforcement yielding could not be captured at the available sampling rate.

The loss of linear proportionality between pairs of strains gauges as indicative of damage was investigated. First, detection of yielding was attempted by tracking the change in linear proportionality between the newly proposed TRDI and a strain measurement at an arbitrary location. This approach was expanded on by tracking the loss of linear proportionality between sets of strain measurements recorded during the dynamic response of the instrumented structure.

The contribution of the thesis could be summarized in three bullet points:

- Stipulating on the mechanism causing high frequency transients in reinforced concrete bridge piers.

- Proposing a relationship between the arrival time of the high-frequency transients and time-instances of deformation extrema with the degree of damage.

- Expanding on the explicit use of loss of linear proportionality as indicative of ground-motion induced damage.

Further research should be carried out in order to confirm the applicability of the above investigated methods. It would also be of interest to apply the method on masonry structures, as it is expected that damage in masonry would generate HFT's in the low-frequency range. Kaiser's effect and Felicity's ratio are well know concepts in classic acoustic emission, but their application in the frequency range associated with HFT's is not researched. It might be of value to research if a decreasing Felicity ratio is related to accumulation of damage for HFT signals. This phenomenon is already observed in classic AE for FRP ([92], [93]) and concrete [94].

Bibliography

[1] AA Pollock. Inspecting bridges with acoustic emissioninspection details about in-service steel bridges and monitoring weld operations: application guidelines. *Prepared by: Physical Acoustics Corporation*, 1995.

[2] David M Boore and Julian J Bommer. Processing of strong-motion accelerograms: needs, options and consequences. *Soil Dynamics and Earthquake Engineering*, 25(2):93–115, 2005.

[3] FEMA 274. NEHRP Commentary on the Guidelines For Seismic Rehabilitation of Buildings. Standard, Federal Emergency Management Agency, Washington, D.C, October 1997.

[4] W. H. Pan, Mu-Xuan Tao, and J. Nie. Simulation of an rc bridge column shake-table test using a fiber beam-column model considering reinforcement anchorage slip. 01 2017.

[5] MJ Schoettler, JI Restrepo, G Guerrini, DE Duck, and F Carrea. A full-scale, single-column bridge bent tested by shake-table excitation. *Center for Civil Engineering Earthquake Research, Department of Civil Engineering, University of Nevada*, 2012.

[6] Mehmet Celebi. Seismic monitoring of structures and new developments. In *Earthquakes and health monitoring of civil structures*, pages 37–84. Springer, 2013.

[7] Mehmet Çelebi. Seismic monitoring to assess performance of structures in near-real time: Recent progress. In *Seismic Risk Assessment and Retrofitting*, pages 1–24. Springer, 2009.

[8] Charles R Farrar and Keith Worden. An introduction to structural health monitoring. *Philosophical Transactions of the Royal Society A: Mathematical, Physical and Engineering Sciences*, 365(1851): 303–315, 2006.

[9] MI Todorovska and MD Trifunac. Earthquake damage detection in structures and early warning. In *The 14th world conference on earthquake engineering*, pages 12–17, 2008.

[10] C Rojah. Atc-20-1 field manual: Postearthquake safety evaluation of buildings. *Applied Technology Council*, page 12, 2005.

[11] FEMA 273. NEHRP Guidelines For Seismic Rehabilitation of Buildings. Standard, Federal Emergency Management Agency, Washington, D.C, October 1997.

[12] Derek A Skolnik and John W Wallace. Critical assessment of interstory drift measurements. *Journal of structural engineering*, 136(12):1574–1584, 2010.

[13] MD Trifunac and MI Todorovska. A note on the useable dynamic range of accelerographs recording translation. *Soil dynamics and Earthquake engineering*, 21(4):275–286, 2001.

[14] MAH Akhand and Kazuyuki Murase. Ensembles of neural networks based on the alteration of input feature values. *International journal of neural systems*, 22(01):77–87, 2012.

[15] Teruya Yamanishi, Jian-Qin Liu, and Haruhiko Nishimura. Modeling fluctuations in default-mode brain network using a spiking neural network. *International journal of neural systems*, 22(04): 1250016, 2012.

[16] Zhaohui Cen, Jiaolong Wei, and Rui Jiang. A gray-box neural network-based model identification and fault estimation scheme for nonlinear dynamic systems. *International journal of neural systems*, 23(06):1350025, 2013.

[17] Wolfgang Graf, Steffen Freitag, J-U Sickert, and Michael Kaliske. Structural analysis with fuzzy data and neural network based material description. *Computer-Aided Civil and Infrastructure Engineering*, 27(9):640–654, 2012.

[18] Fan Liu and Meng Joo Er. A novel efficient learning algorithm for self-generating fuzzy neural network with applications. *International Journal of Neural Systems*, 22(01):21–35, 2012.

[19] Kartick Subramanian and Sundaram Suresh. Human action recognition using meta-cognitive neuro-fuzzy inference system. *International journal of neural systems*, 22(06):1250028, 2012.

[20] Yiannis Boutalis, Manolis Christodoulou, and Dimitrios Theodoridis. Indirect adaptive control of nonlinear systems based on bilinear neuro-fuzzy approximation. *International Journal of Neural Systems*, 23(05):1350022, 2013.

[21] Nazmul Siddique and Hojjat Adeli. *Computational intelligence: synergies of fuzzy logic, neural networks and evolutionary computing*. John Wiley & Sons, 2013.

[22] Hongjin Kim and Hojjat Adeli. Hybrid control of smart structures using a novel wavelet-based algorithm. *Computer-Aided Civil and Infrastructure Engineering*, 20(1):7–22, 2005.

[23] Juan Pablo Amezquita-Sanchez and Hojjat Adeli. Signal processing techniques for vibration-based health monitoring of smart structures. *Archives of Computational Methods in Engineering*, 23(1): 1–15, 2016.

[24] Daniele Zonta, Ahmed Elgamal, Michael Fraser, and MJ Nigel Priestley. Analysis of change in dynamic properties of a frame-resistant test building. *Engineering Structures*, 30(1):183–196, 2008.

[25] H. Wenzel and VCE Vienna Consulting Engineers ZT GmbH Krims-Steiner. *Industrial Safety and Life Cycle Engineering: Technologies, Standards, Applications ; IRIS, Chapter 3*. VCE Vienna Consulting Engineers ZT GmbH, 2013. ISBN 9783200031791.

[26] Helmut Wenzel. Ambient vibration monitoring. *Encyclopedia of Structural Health Monitoring*, 2009.

[27] James MW Brownjohn, Alessandro De Stefano, You-Lin Xu, Helmut Wenzel, and A Emin Aktan. Vibration-based monitoring of civil infrastructure: challenges and successes. *Journal of Civil Structural Health Monitoring*, 1(3-4):79–95, 2011.

[28] Helmut Wenzel. *Health monitoring of bridges*. John Wiley & Sons, 2008.

[29] A Tributsch and C Adam. An enhanced energy vibration-based approach for damage detection and localization. *Structural Control and Health Monitoring*, 25(1), 2018.

[30] Alban Kita, Nicola Cavalagli, and Filippo Ubertini. Temperature effects on static and dynamic behavior of consoli palace in gubbio, italy. *Mechanical Systems and Signal Processing*, 120:180–202, 2019.

[31] Carmelo Gentile, Marco Guidobaldi, and Antonella Saisi. One-year dynamic monitoring of a historic tower: damage detection under changing environment. *Meccanica*, 51(11):2873–2889, 2016.

[32] Filipe Magalhães, A Cunha, and Elsa Caetano. Vibration based structural health monitoring of an arch bridge: from automated oma to damage detection. *Mechanical Systems and Signal Processing*, 28:212–228, 2012.

[33] Alessandro Cabboi, Carmelo Gentile, and Antonella Saisi. From continuous vibration monitoring to fem-based damage assessment: application on a stone-masonry tower. *Construction and Building Materials*, 156:252–265, 2017.

[34] Antonella Saisi, Carmelo Gentile, and Marco Guidobaldi. Post-earthquake continuous dynamic monitoring of the gabbia tower in mantua, italy. *Construction and Building Materials*, 81:101–112, 2015.

[35] Wenchen Shan, Xianqiang Wang, and Yubo Jiao. Modeling of temperature effect on modal frequency of concrete beam based on field monitoring data. *Shock and Vibration*, 2018, 2018.

[36] Yong Xia, Bo Chen, Shun Weng, Yi-Qing Ni, and You-Lin Xu. Temperature effect on vibration properties of civil structures: a literature review and case studies. *Journal of civil structural health monitoring*, 2(1):29–46, 2012.

[37] Alan G Beattie. Acoustic emission non-destructive testing of structures using source location techniques. *Albuquerque and Livermore*, 2013.

[38] Martine Wevers and Kasper Lambrighs. *Applications of Acoustic Emission for SHM: A Review*. 09 2009. ISBN 9780470061626. doi: 10.1002/9780470061626.shm011.

[39] Masayasu Ohtsu. *Acoustic emission and related non-destructive evaluation techniques in the fracture mechanics of concrete: fundamentals and applications*. Woodhead Publishing, 2015.

[40] Masayasu Ohtsu. Elastic wave methods for nde in concrete based on generalized theory of acoustic emission. *Construction and Building Materials*, 122:845–854, 2016.

[41] Tomoki Shiotani and Masayasu Ohtsu. Prediction of slope failure based on ae activity. In *Acoustic emission: standards and technology update*. ASTM International, 1999.

[42] A Behnia, HK Chai, M Yorikawa, S Momoki, M Terazawa, and T Shiotani. Integrated non-destructive assessment of concrete structures under flexure by acoustic emission and travel time tomography. *Construction and Building Materials*, 67:202–215, 2014.

[43] Tomoki Shiotani. Evaluation of long-term stability for rock slope by means of acoustic emission technique. *Ndt & E International*, 39(3):217–228, 2006.

[44] Masayasu Ohtsu and S Yuyama. Recommended practice for in situ monitoring of concrete structures by acoustic emission. In *15 th International Acoustic Emission Symposium*, pages 263–268, 2000.

[45] Christian U Grosse and Masayasu Ohtsu. *Acoustic emission testing*. Springer Science & Business Media, 2008.

[46] Dong-Jin Yoon, W Jason Weiss, and Surendra P Shah. Assessing damage in corroded reinforced concrete using acoustic emission. *Journal of engineering mechanics*, 126(3):273–283, 2000.

[47] Nobuhiro Okude, Minoru Kunieda, Tomoki Shiotani, and Hikaru Nakamura. Flexural failure behavior of rc beams with rebar cor-rosion and damage evaluation by acoustic emmission. *Journal of Acoustic Emission*, 27:263–271, 2009.

[48] Salvatore Salamone, Marc J Veletzos, Francesco Lanza di Scalea, and José I Restrepo. Detection of initial yield and onset of failure in bonded posttensioned concrete beams. *Journal of Bridge Engineering*, 17(6):966–974, 2012.

[49] Paul H Ziehl, Nestore Galati, Antonio Nanni, and J Gustavo Tumialan. In-situ evaluation of two concrete slab systems. ii: evaluation criteria and outcomes. *Journal of Performance of Constructed Facilities*, 22(4):217–227, 2008.

[50] Marwa Abdelrahman, Mohamed K ElBatanouny, and Paul H Ziehl. Acoustic emission based damage assessment method for prestressed concrete structures: Modified index of damage. *Engineering Structures*, 60:258–264, 2014.

[51] Matteo Di Benedetti, Giovanni Loreto, Fabio Matta, and Antonio Nanni. Acoustic emission historic index and frequency spectrum of reinforced concrete under accelerated corrosion. *Journal of materials in civil engineering*, 26(9):04014059, 2014.

[52] Francisco Sagasta, Yoshihiro Mizutani, Ignacio Valverde, Elisabet Suarez, J Rescalvo Francisco, and Antolino Gallego. Influence of attenuation on the acoustic emission b-value for damage evaluation of reinforced concrete specimens.

[53] Arash Behnia, Hwa Kian Chai, and Tomoki Shiotani. Advanced structural health monitoring of concrete structures with the aid of acoustic emission. *Construction and Building Materials*, 65: 282–302, 2014.

[54] Janise E Rodgers and Mehmet Çelebi. Method for detecting moment connection fracture using high-frequency transients in recorded accelerations. *Journal of Constructional Steel Research*, 67 (3):293–307, 2011.

[55] LATBSDC. An alternative procedure for seismic analysis and design of tall buildings located in the Los Angeles region. Document, Los Angeles Tall Buildings Structural Design Council, Los Angeles, C.A, March 2018.

[56] Paul Bodin, John Vidale, Timothy Walsh, Recep Çakir, and Mehmet Çelebi. Transient and long-term changes in seismic response of the natural resources building, Olympia, Washington, due to earthquake shaking. *Journal of Earthquake Engineering*, 16(5):607–622, 2012.

[57] Aleksandar Zhelyazkov, Daniele Zonta, Helmut Wenzel, and Peter Furtner. On the estimation of the ductility demand on reinforced concrete bridge piers from structural health monitoring data. *Journal of Civil Structural Health Monitoring*, pages 1–13, 2020.

[58] Zhuo-Han Wang, Lei Li, Yi-Xin Zhang, and Shan-Suo Zheng. Reinforcement model considering slip effect. *Engineering Structures*, 198:109493, 2019.

[59] Dario Coronelli and Maria Gabriella Mulas. Local–global approach in the seismic analysis of r/c frames including bond slip effects. *Engineering structures*, 23(8):911–925, 2001.

[60] R Eligehausen, EP Popov, and VV Bertero. Local bond stress-slip relationships of deformed bars under generalized excitations, report no. ucb/eerc 83-23. *University of California, Berkeley*, 1983.

[61] SS Mousavi, M Dehestani, and KK Mousavi. Bond strength and development length of steel bar in unconfined self-consolidating concrete. *Engineering Structures*, 131:587–598, 2017.

[62] Yu-Fei Wu and Xue-Mei Zhao. Unified bond stress–slip model for reinforced concrete. *Journal of Structural Engineering*, 139(11):1951–1962, 2013.

[63] Eliene Pires Carvalho, Marcela Palhares Miranda, Danielle SG Fernandes, and Guilherme Victor Alves. Comparison of test methodologies to evaluate steel-concrete bond strength of thin reinforcing bar. *Construction and Building Materials*, 183:243–252, 2018.

[64] M Dehestani and SS Mousavi. Modified steel bar model incorporating bond-slip effects for embedded element method. *Construction and Building Materials*, 81:284–290, 2015.

[65] M Dehestani, A Asadi, and SS Mousavi. On discrete element method for rebar-concrete interaction. *Construction and Building Materials*, 151:220–227, 2017.

[66] DV Bompa and AY Elghazouli. Bond-slip response of deformed bars in rubberised concrete. *Construction and Building Materials*, 154:884–898, 2017.

[67] Thomas L Paez. The history of random vibrations through 1958. *Mechanical Systems and Signal Processing*, 20(8):1783–1818, 2006.

[68] Enders A Robinson. A historical perspective of spectrum estimation. *Proceedings of the IEEE*, 70 (9):885–907, 1982.

[69] Jiann-Shiun Lew. Using transfer function parameter changes for damage detection of structures. *AIAA journal*, 33(11):2189–2193, 1995.

[70] Jennifer E Michaels and Thomas E Michaels. Detection of structural damage from the local temporal coherence of diffuse ultrasonic signals. *IEEE transactions on ultrasonics, ferroelectrics, and frequency control*, 52(10):1769–1782, 2005.

[71] DD Rizos, SD Fassois, ZP Marioli-Riga, and AN Karanika. Vibration-based skin damage statistical detection and restoration assessment in a stiffened aircraft panel. *Mechanical Systems and Signal Processing*, 22(2):315–337, 2008.

[72] Demosthenis D Rizos, Spilios D Fassois, Zaira P Marioli-Riga, and Alexandra N Karanika. Statistical skin damage detection and restoration assessment for aircraft panels via vibration testing. In *First European Workshop on Structural Health Monitoring, Paris, France*, pages 1211–1218, 2002.

[73] Spilios D Fassois and John S Sakellariou. Time-series methods for fault detection and identification in vibrating structures. *Philosophical Transactions of the Royal Society A: Mathematical, Physical and Engineering Sciences*, 365(1851):411–448, 2007.

[74] Charles Joseph Schallhorn. Localization of vibration-based damage detection method in structural applications. 2012.

[75] *General Static Analysis of Finite Element Structures*. SOFiSTiK AG.

[76] A SIMQKE. Program for artificial ground motion generation. users manual and documentation, 1976.

[77] Anil K Chopra. *Dynamics of structures theory and*. 1995.

[78] Telemachos B Panagiotakos and Michael N Fardis. Deformations of reinforced concrete members at yielding and ultimate. *Structural Journal*, 98(2):135–148, 2001.

[79] Caltrans. Seismic Design Criteria. Standard, California Department of Transportation, Sacramento, C.A, 2006.

[80] British Standard. Eurocode 8: Design of structures for earthquake resistance. *Part*, 1:1998–1, 2005.

[81] Alan V Oppenheim. *Discrete-time signal processing*. Pearson Education India, 1999.

[82] Eric Chassande-Mottin, Franois Auger, and Patrick Flandrin. *Reassignment*, chapter 9, pages 249–277. Wiley-Blackwell, 2010. ISBN 9780470611203.

[83] Jian Zhao and Sri Sritharan. Modeling of strain penetration effects in fiber-based analysis of reinforced concrete structures. *Aci Structural Journal*, 104:133–141, 03 2007.

[84] J Kaiser. *Untersuchungen uber das Auftreten Gerauschen beim Zugversuch.(A Study of Acoustic Phenomena in Tensile Tests)*. PhD thesis, Ph. D. Thesis. Technische Hochschule of Munchen. Munich Germany, 1950 .

[85] Robert Klingel. *Anziehverfahren für hochfeste Schraubenverbindungen auf Basis akustischer Emissionen*, volume 169. Herbert Utz Verlag, 2002.

[86] Nak-Sam Choi, Tae-Won Kim, and Kyoung Y Rhee. Kaiser effects in acoustic emission from composites during thermal cyclic-loading. *Ndt & E International*, 38(4):268–274, 2005.

[87] Erling Nordlund, Chunlin Li, et al. Acoustic emission and the kaiser effect in rock materials. In *The 31th US Symposium on Rock Mechanics (USRMS)*. American Rock Mechanics Association, 1990.

[88] A Lavrov. The kaiser effect in rocks: principles and stress estimation techniques. *International Journal of Rock Mechanics and Mining Sciences*, 40(2):151–171, 2003.

[89] Chunlin Li and Erling Nordlund. Experimental verification of the kaiser effect in rocks. *Rock Mechanics and Rock Engineering*, 26(4):333–351, 1993.

[90] AA Shah and Y Ribakov. Effectiveness of nonlinear ultrasonic and acoustic emission evaluation of concrete with distributed damages. *Materials & Design*, 31(8):3777–3784, 2010.

[91] Kaiser effect. https://www.ndt.net/ndtaz/content.php?id=476. Accessed: 2020-02-10.

[92] Jess M Waller, E Andrade, and RL Saulsberry. Use of acoustic emission to monitor progressive damage accumulation in kevlar® 49 composites. In *AIP Conference Proceedings*, volume 1211, pages 1111–1118. American Institute of Physics, 2010.

[93] Commemorative Speech. The origin of carp and the term felicity effect.

[94] Abid A Shah, Rahmat Ali, Amjad Naseer, and Ch Zhang. Assessment of progressive damages in concrete with acoustic emission technique. *Advances in Applied Acoustics (AIAAS)*, 3, 2014.

Appendices

Appendix A

Appendix A Reinforcement plan of the U.C. San Diego column

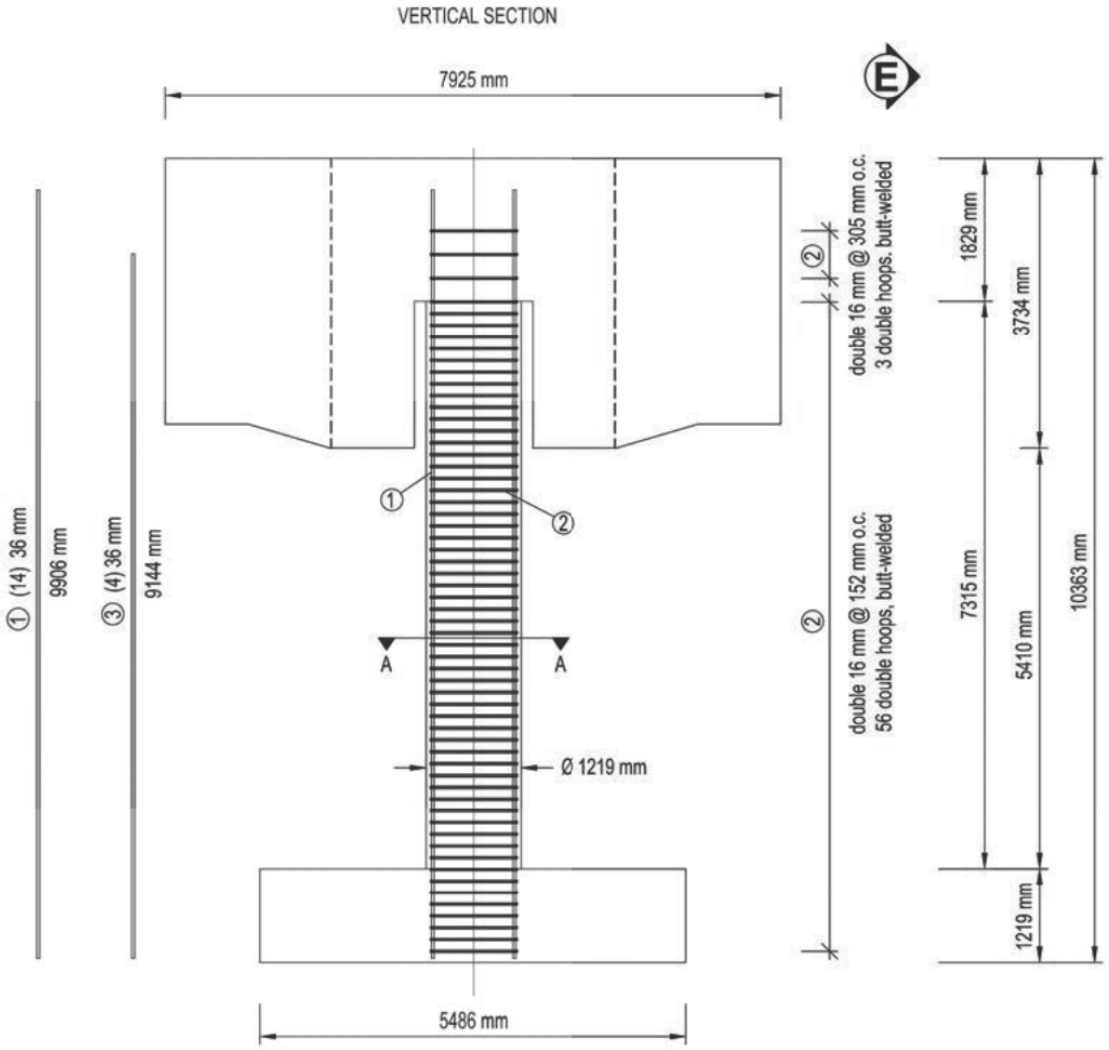
VERTICAL SECTION
7925 mm
E
① (14) 36 mm
9906 mm
③ (4) 36 mm
9144 mm
②
double 16 mm @ 305 mm o.c.
3 double hoops. butt-welded
② double 16 mm @ 152 mm o.c.
56 double hoops, butt-welded
1829 mm
3734 mm
7315 mm
5410 mm
10363 mm
1219 mm
A
A
Ø 1219 mm
5486 mm

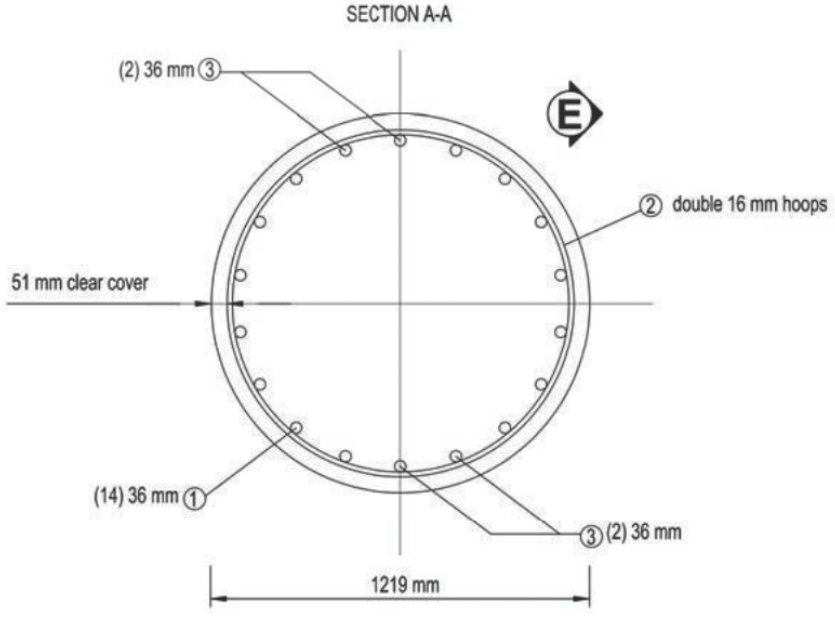
SECTION A-A
(2) 36 mm ③
E
② double 16 mm hoops
51 mm clear cover
(14) 36 mm ①
③ (2) 36 mm
1219 mm

Appendix B

Appendix B Reinforcement plans of the columns tested at the University of Patras

COLUMN REINFORCEMENT D=30cm

Section 1-1

1:25

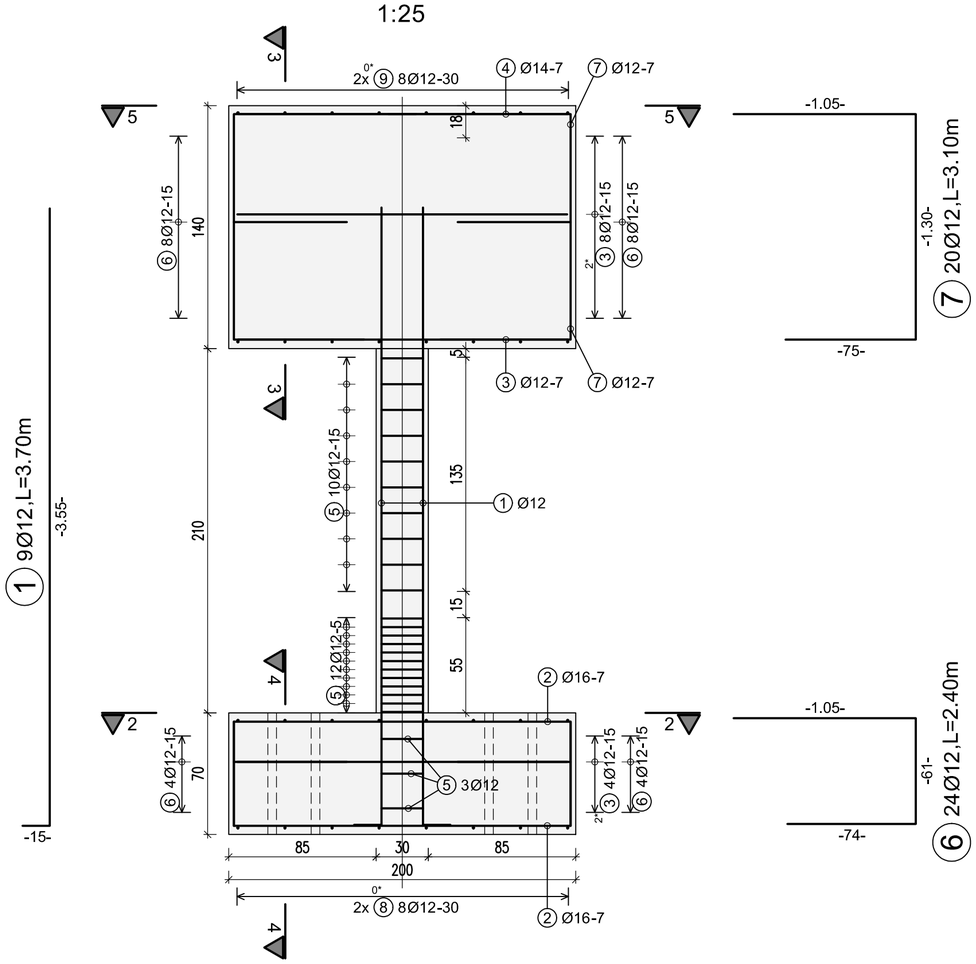

Section 3-3

1:25

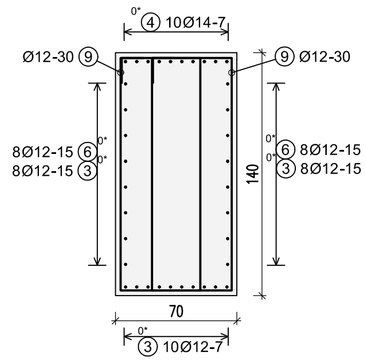

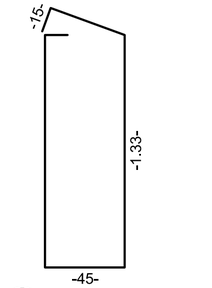

Section 4-4

1:25

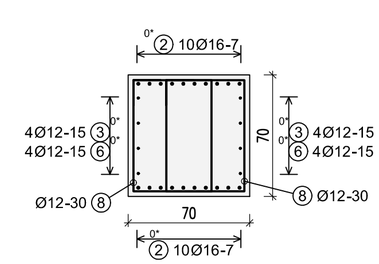

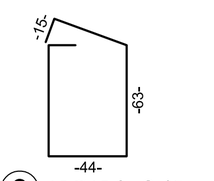

Section 2-2

1:25

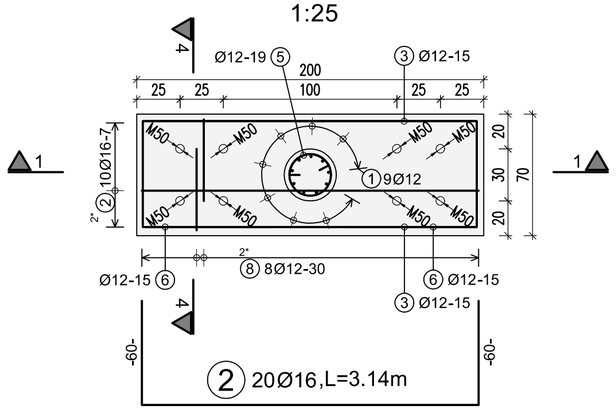

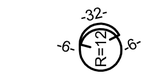

5 25Ø12,L=1.19m
Übergreifung 0.32m

Section 5-5

1:25

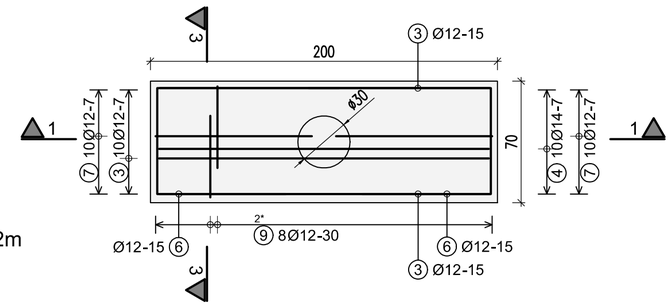

PROTECTION AGAINST ACCIDENTS

STRAIGHT UPTURNED ENDING BARS (REINFORCEMENT CONNECTION) MUST BE COVERED OR ADDITIONAL BEND AT THE END OF THE BAR WITHOUT REDUCTION OF THE CONNECTION LENGTH

BENDING SCHEDULE ACCORDING TO EN 1992-1-1

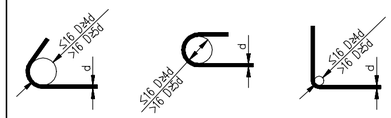

LAYERBOARD PLATES

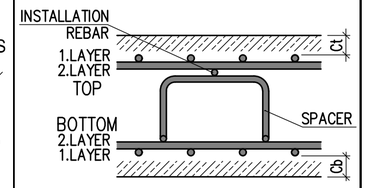

NOTES:

1.) ALL BENDING DIMENSIONS ARE EXTERNAL DIMENSIONS.
2.) SPACER BAR: IF THERE ARE NO OTHER INSTRUCTIONS, THE STRUCTURAL CONNECTIONS SHOULD BE DISLOCATED WITH THE SPECIFIED LAP LENGTH
3.) CURVATURES, BEND UPS, STEEL ANGLE AND LOOPS SHOULD BE IMPLEMENTED ACCORDING TO EN 1992-1-1

STEEL: **B500 C**

LAST STEEL BAR: 9
LAST MAT POSITION: 0

ELEMENT	CONCRETE QUALITY	CONCRETE COVER [MM] TOP (Co)	BOTTOM (Cu)
Column	**C25/30**	**30**	**30**

B A R S C H E D U L E Steelgrade: B500 C

Pos.	No.	d	Length	D12	D14	D16
1	9	12	3.70	33.30		
2	20	16	3.14			62.80
3	34	12	1.90	64.60		
4	10	14	1.90		19.00	
5	25	12	1.19	29.75		
6	24	12	2.40	57.60		
7	20	12	3.10	62.00		
8	16	12	2.45	39.20		
9	16	12	3.85	61.60		
Total lengths				348.05	19.00	62.80
kg / m				D12 0.888	D14 1.210	D16 1.580
kg / d				309.068	22.990	99.224
Total weight (kg)				431.282		

DRAFT 30.01.2019

VCE Vienna Consulting Engineers ZT GmbH

PROJECT TITLE

PLAN DESCRIPTION:
COLUMN REINFORCEMENT
D = 30 cm

DATE:	PL. NR.:	IND.:
30.01.2019	COL-RF-01	A

COLUMN REINFORCEMENT D=40cm

Section 1-1

1:25

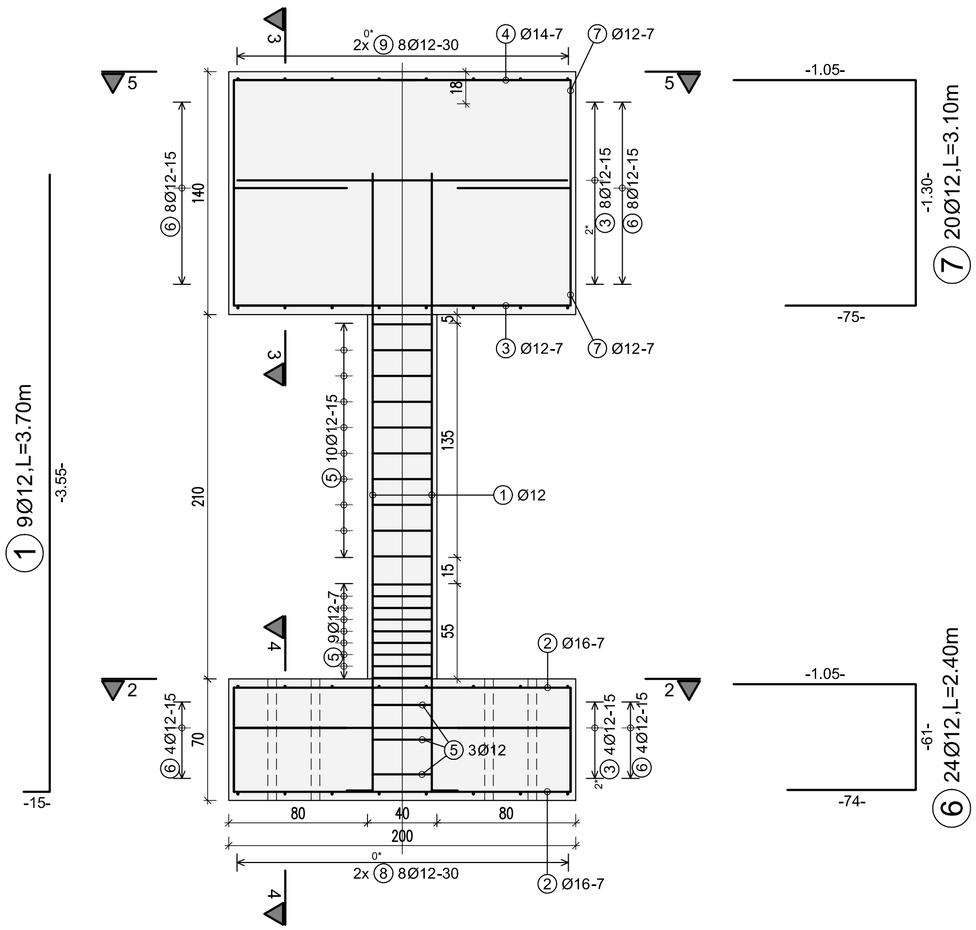

Section 3-3

1:25

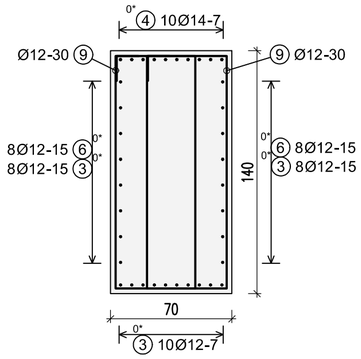

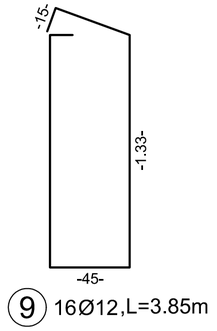

Section 4-4

1:25

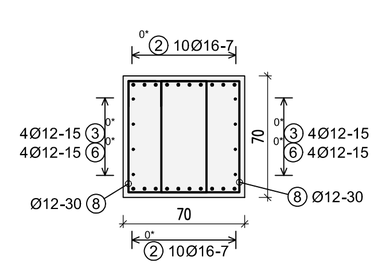

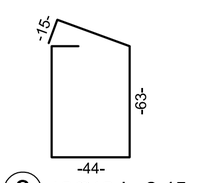

Section 2-2

1:25

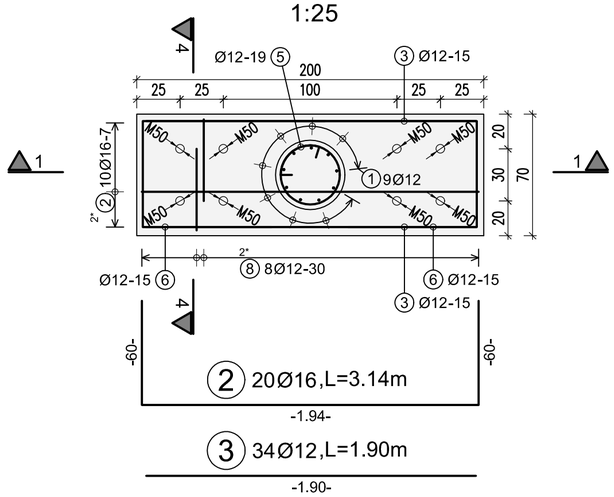

Section 5-5

1:25

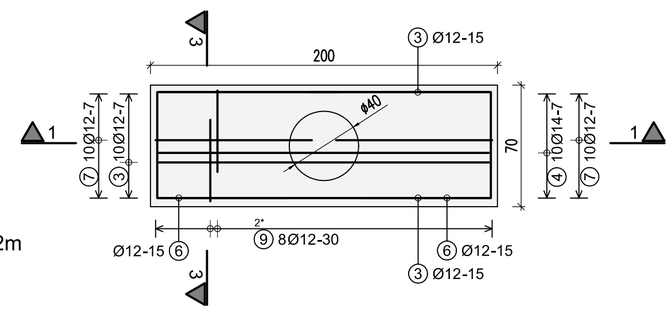

PROTECTION AGAINST ACCIDENTS

STRAIGHT UPTURNED ENDING BARS (REINFORCEMENT CONNECTION) MUST BE COVERED OR ADDITIONAL BEND AT THE END OF THE BAR WITHOUT REDUCTION OF THE CONNECTION LENGTH

BENDING SCHEDULE ACCORDING TO EN 1992-1-1

LAYERBOARD PLATES

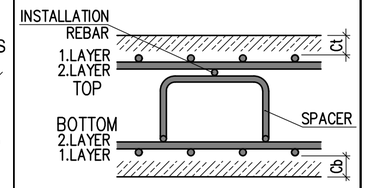

NOTES:

1.) ALL BENDING DIMENSIONS ARE EXTERNAL DIMENSIONS.
2.) SPACER BAR: IF THERE ARE NO OTHER INSTRUCTIONS, THE STRUCTURAL CONNECTIONS SHOULD BE DISLOCATED WITH THE SPECIFIED LAP LENGTH
3.) CURVATURES, BEND UPS, STEEL ANGLE AND LOOPS SHOULD BE IMPLEMENTED ACCORDING TO EN 1992-1-1

STEEL: **B500 C**

LAST STEEL BAR: 9
LAST MAT POSITION: 0

ELEMENT	CONCRETE QUALITY	CONCRETE COVER [MM] TOP (Co)	BOTTOM (Cu)
Column	**C25/30**	**30**	**30**

B A R S C H E D U L E Steelgrade: B500 C

Pos.	No.	d	Length	D12	D14	D16
1	9	12	3.70	33.30		
2	20	16	3.14			62.80
3	34	12	1.90	64.60		
4	10	14	1.90		19.00	
5	22	12	1.52	33.44		
6	24	12	2.40	57.60		
7	20	12	3.10	62.00		
8	16	12	2.45	39.20		
9	16	12	3.85	61.60		
Total lengths				351.74	19.00	62.80
kg / m				D12 0.888	D14 1.210	D16 1.580
kg / d				312.345	22.990	99.224
Total weight (kg)				434.559		

DRAFT 30.01.2019

VCE Vienna Consulting Engineers ZT GmbH

PROJECT TITLE

PLAN DESCRIPTION:
COLUMN REINFORCEMENT
D = 40 cm

DATE:	PL. NR.:	IND.:
30.01.2019	COL-RF-02	A

Appendix C

Appendix C Instrumentation U.C. San Diego column

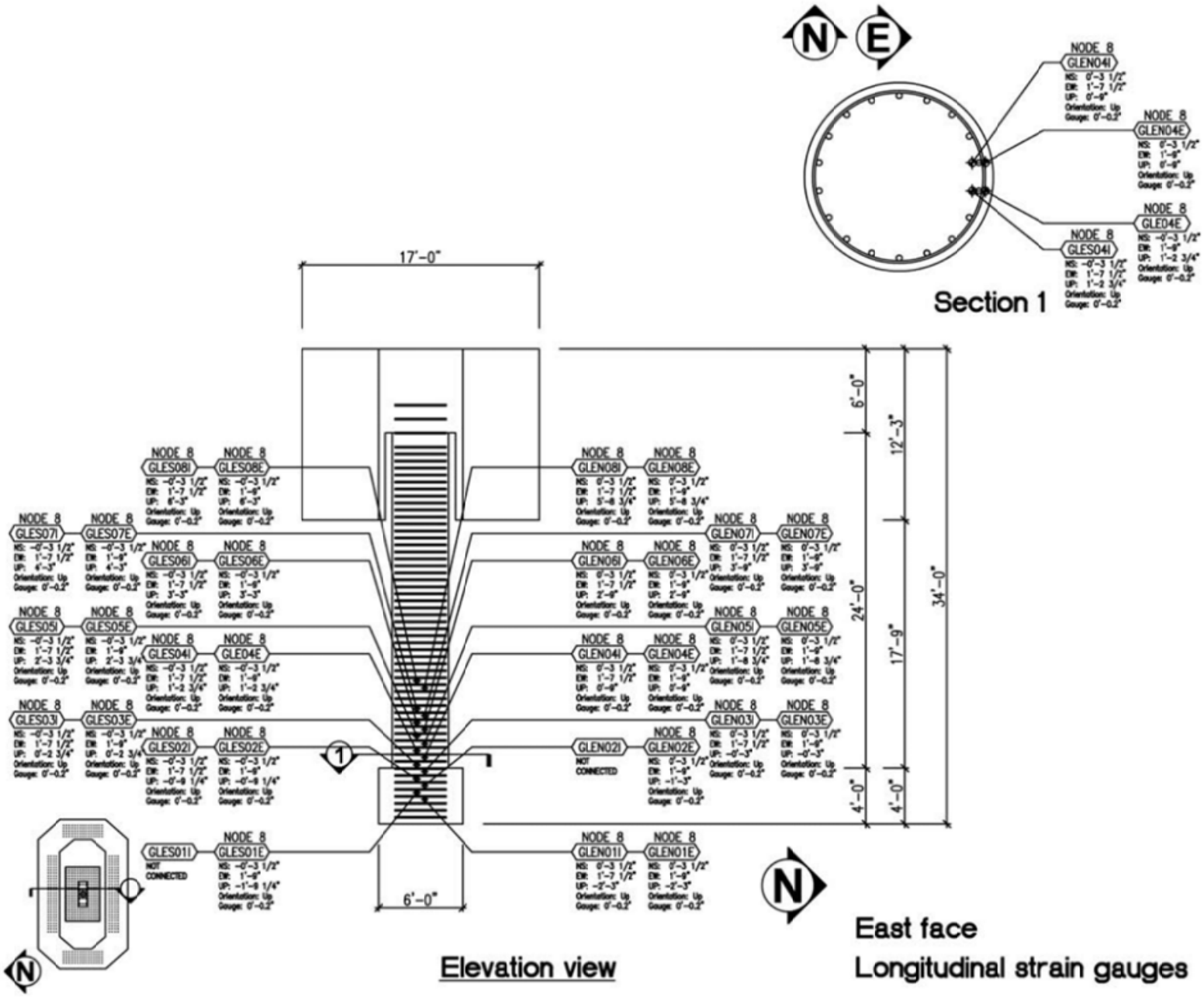
N
E
NODE 8
GLEN04I
NODE 8
GLEN04E
NODE 8
GLE04E
NODE 8
GLES04I
Section 1
17'-0"
6'-0"
12'-3"
24'-0"
17'-9"
34'-0"
4'-0"
4'-0"
6'-0"
GLES08I
GLES08E
GLEN08I
GLEN08E
GLES07I
GLES07E
GLEN07I
GLEN07E
GLES06I
GLES06E
GLEN06I
GLEN06E
GLES05I
GLES05E
GLEN05I
GLEN05E
GLES04I
GLE04E
GLEN04I
GLEN04E
GLES03I
GLES03E
GLEN03I
GLEN03E
GLES02I
GLES02E
GLEN02I
GLEN02E
NOT CONNECTED
GLES01I
GLES01E
GLEN01I
GLEN01E
1
N
Elevation view
East face
Longitudinal strain gauges

Appendix D

Appendix D Instrumentation University of Patras columns

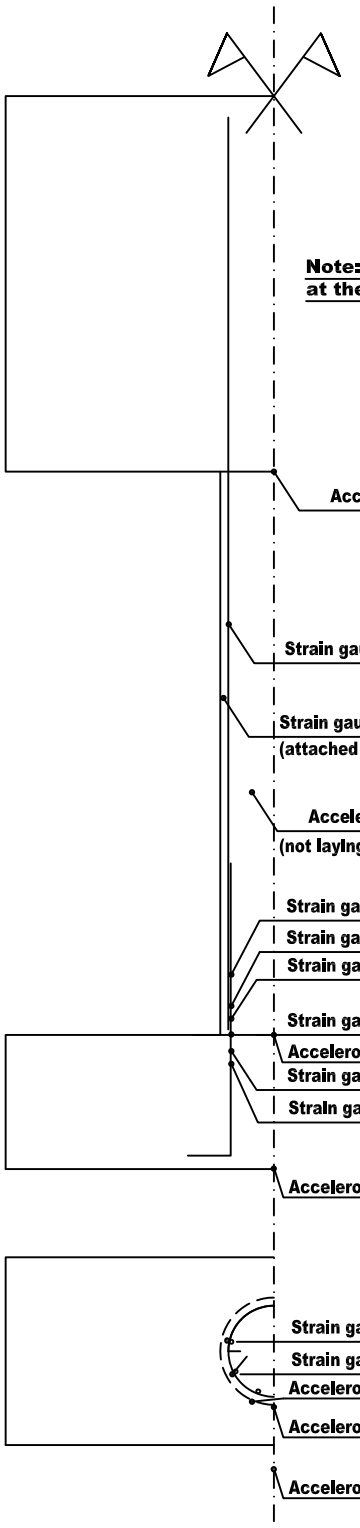

List of strain gauges
1LA, 1LB,1RA,1RB
2LA, 2LB,2RA,2RB
3LA, 3LB,3RA,3RB
4LA, 4LB,4RA,4RB
5LA, 5LB,5RA,5RB
6LA, 6LB,6RA,6RB
7LA, 7LB,7RA,7RB
8LA, 8LB,8RA,8RB
Total number - 32

List of accelerometers

A1, A2, A3, A4

Total number - 4

VCE Vienna Consulting Engineers ZT GmbH

CONTENTS: COLUMN INSTRUMENTATION